Stony Brook University

Statistical image reconstruction for low-dose X-ray computed tomography: statistical models and regularization strategies

A Dissertation Presented

by

Hao Zhang

to

The Graduate School

in Partial Fulfillment of the Requirements

for the Degree of

Doctor of Philosophy

in

Biomedical Engineering

Stony Brook University

May 2016

Stony Brook University
The Graduate School

Hao Zhang

We, the dissertation committee for the above candidate for the
Doctor of Philosophy degree, hereby recommend
acceptance of this dissertation.

Jerome Liang, PhD – Dissertation Advisor
Professor of Radiology and Biomedical Engineering

Yingtian Pan, PhD - Chairperson of Defense
Professor of Biomedical Engineering

Terry Button, PhD - Committee Member
Associate Professor of Biomedical Engineering

Gene Gindi, PhD - Committee Member
Associate Professor of Biomedical Engineering

William Moore, MD - Committee Member
Associate Professor of Radiology, NYU

This dissertation is accepted by the Graduate School

Charles Taber
Dean of the Graduate School

Abstract of the Dissertation

Statistical image reconstruction for low-dose X-ray computed tomography: statistical models and regularization strategies

by

Hao Zhang

Doctor of Philosophy

in

Biomedical Engineering

Stony Brook University

2016

Low-dose X-ray computed tomography (CT) imaging is desirable due to the growing concerns about excessive radiation exposure to the patients. However, the reconstructed CT images by the conventional filtered back-projection (FBP) method from the low-dose acquisitions may be severely degraded. Statistical image reconstruction (SIR) methods have shown potential to substantially improve the image quality of low-dose CT as compared to the FBP method. According to the maximum a posteriori (MAP) estimation, the SIR methods can be typically formulated by an objective function consisting of two terms: (1) data-fidelity term modeling the statistics of projection measurements, and (2) regularization term reflecting prior knowledge or expectation on the characteristics of the image to be reconstructed. Statistical modeling of the projection measurements is a prerequisite for SIR, while the regularization term in the objective function also plays a critical role for successful image reconstruction. The objective of this dissertation is investigating accurate statistical models and novel regularization strategies for SIR to improve CT image quality in low-dose cases. Specifically, we proposed two texture-preserving regularizations based on the Markov random field (MRF) model and one generic regularization based on the nonlocal means (NLM) filter. The feasibility and efficacy of the proposed strategies are explicitly explored in this dissertation, using both computer simulation and real data (i.e., physical phantoms and clinical patients).

To my family

Contents

List of Figures vii
List of Tables xi
List of Acronyms xii
Acknowledgements xiii
Chapter 1. Low-dose X-ray computed tomography imaging 1
1.1 X-ray photons emission and beam filtration 1
1.2 Fundamentals of X-ray CT imaging 2
1.3 Intensity distribution of incident X-ray photons 3
1.4 X-ray photons interaction inside the patient 3
1.5 Signal model for energy-integrating detector 4
1.6 Degrading factors and signal preprocessing 5
Chapter 2. Statistical image reconstruction of low-dose CT 6
2.1 Statistical modeling on projection measurements 7
2.1.1 Calibrated transmitted photon counts 7
2.1.2 Calibrated line integrals 8
2.2 Discrete forward models 8
2.3 Maximum likelihood (ML)/weighted least-squares (WLS) criterions 9
2.3.1 Poisson model for calibrated transmitted photon counts 9
2.3.2 Poisson+Gaussian model for calibrated transmitted photon counts 10
2.3.3 Gaussian model for calibrated line integrals 10
2.4 Maximum a posteriori (MAP) estimation 11
Chapter 3. Deriving voxel-specific MRF coefficients from previous normal-dose CT scan for low-dose CT reconstruction 13
3.1 Introduction 13
3.2 Markov random field (MRF) model-based regularization 14
3.3 The proposed adaptive MRF regularization 14
3.3.1 Computation of object scale 15
3.3.2 Determination of MRF window size and sample window size 16
3.3.3 Prediction of MRF coefficients 17
3.4 Summary of presented reconstruction method 18
3.5 Experiments and results 19
3.5.1 Anthropomorphic torso phantom study 19
3.5.2 Patient data study 23
3.6 Discussion and conclusion 28
Chapter 4. Deriving region-specific MRF coefficients from previous full-dose CT scan for low-dose CT reconstruction 30
4.1 Introduction 30
4.2 The proposed texture-preserving MRF regularization 31
4.3 Summary of the presented PWLS-texture method 32
4.4 Experiments and results 33
4.4.1 Experiments on simulated low-dose sinogram data 34
4.4.2 Experiments on real low-dose sinogram data 42
4.5 Discussion and conclusion 46
Chapter 5. Adaptive nonlocal means-regularized statistical image reconstruction for low-mAs CT 48

5.1 Introduction 48
5.2 Overview of the NLM algorithm 49
5.3 Adaptive NLM-regularized statistical image reconstruction 50
5.3.1 NLM-based regularization 50
5.3.2 Local adaption of the filtering parameter h 50
5.3.3 Adaptive NLM-regularized statistical image reconstruction 51
5.4 Experiments and results 51
5.4.1 Digital clock phantom 51
5.4.2 Physical anthropomorphic torso phantom 54
5.4.3 Clinical patient data 57
5.5 Discussion and Conclusion 59
Chapter 6. Adaptive nonlocal-means regularized statistical image reconstruction for sparse-view CT 61
6.1 Introduction 61
6.2 Adaptive NLM-regularized image reconstruction 62
6.3 Experiments and results 63
6.3.1 Digital clock phantom 63
6.3.2 Clinical patient data 66
6.4 Discussion and conclusion 69
Chapter 7. Overview and prospective of SIR for low-dose CT 71
7.1 Construction of objective function 71
7.2 Optimization of objective function 72
7.3 Clinical use of SIR methods 72

List of Figures

Figure 1.1. Illustration of the bowtie filter and flat filter used in clinical CT system
Figure 1.2. Illustration of normalized energy spectra of incident X-ray photons with tube voltage at 80, 100, 120 and 140 kV.
Figure 1.3. Incident photons distribution in different detector bins caused by the bowtie filter. (Figure reprinted from Manduca et al. 2009, Projection space denoising with bilateral filtering and CT noise modeling for dose reduction in CT, Med. Phys., 36(11): 4911–4919)
Figure 1.4. Flow chart of CT projection data preparation for image reconstruction.
Figure 2.1. List of image reconstruction methods for X-ray CT.
Figure 2.2. (a) pixel-driven projection-backprojection; (b) ray-driven projection-backprojection; (c) distance-driven projection-backprojection. (Figure reprinted from DeMan and Basu 2004, Distance-driven projection and backprojection in three dimensions, Phys. Med. Biol., 49: 2463–2475)
Figure 3.1. (a) One transverse slice of the anthropomorphic torso phantom; (b) the corresponding object scale map of the CT image in (a).
Figure 3.2. Example illustration of the MRF/sample window designed for one single pixel (labeled with green marker). The gray window represents the 7×7 MRF window, and the white window is the corresponding 17×17 sample window.
Figure 3.3. Flow chart of the proposed PWLS iterative reconstruction with adaptive MRF regularization for low-dose CT.
Figure 3.4. A reconstructed slice of the anthropomorphic torso phantom: (a) The FBP reconstruction from the averaged sinogram; (b) The FBP reconstruction from 40 mAs sinogram; (c) The PWLS-GMRF reconstruction from 40 mAs sinogram, $\beta = 3\times10^5$; (d) The PWLS-Huber reconstruction from 40 mAs sinogram, $\beta = 3\times10^5$, $\delta=0.004$; (e) The PWLS-adaptive reconstruction from 40 mAs sinogram, $\beta = 3\times10^5$. All the images are displayed with the same window.
Figure 3.5. Performance comparison of four algorithms on the reconstruction of detailed ROIs labeled in Figure 3.4(b) with four different metrics. The corresponding algorithms are illustrated in figure legend.
Figure 3.6. Comparison of the profiles along the horizontal line labeled in Fig. 4(b) between the four algorithms with 40 mAs sinogram and ground truth image. The corresponding algorithms are illustrated in figure legend.
Figure 3.7. Reconstructed transverse slice of the patient data: (a) The FBP reconstruction from the normal-dose sinogram; (b) The FBP reconstruction from the simulated low-dose sinogram; (c) The PWLS-GMRF reconstruction from the simulated low-dose sinogram, $\beta = 2\times10^5$; (d) The PWLS-Huber reconstruction from the simulated low-dose sinogram, $\beta = 2\times10^5$, $\delta=0.004$; (e) The PWLS-adaptive reconstruction from the simulated low-dose sinogram, $\beta = 2\times10^5$. All the images are displayed with the same window.

Figure 3.8. Performance comparison of four algorithms on the reconstruction of detailed ROIs labeled in Figure 3.7(b) with four different metrics. The corresponding algorithms are illustrated in figure legend.
Figure 3.9. Comparison of the profiles along the horizontal line labeled in Figure 3.7(b) between the four algorithms with simulated low-dose sinogram and the FBP reconstruction with the normal-dose sinogram. The corresponding algorithms are illustrated in figure legend.
Figure 3.10. Comparison of the profiles along the vertical line labeled in Figure 3.7(b) between the three SIR algorithms with simulated low-dose sinogram and the FBP reconstruction with the normal-dose sinogram. The contrast of the small object and the corresponding algorithms are illustrated in figure legend.
Figure 4.1. Flowchart of the proposed texture-preserving LdCT image reconstruction algorithm.
Figure 4.2. Segmented masks of the chest CT image (a). Picture (b) is the lung mask; (c) is the bone mask; (d) is the fat mask; and (e) is the muscle mask.
Figure 4.3. The predicted four sets of MRF model coefficients for the four tissue regions of Figure 4.2 with a 7×7 MRF window size in 2D presentation. The corresponding regions are indicated by picture title.
Figure 4.4. The predicted MRF coefficients of the lung region for five neighboring slices in 2D presentation. The corresponding slice numbers are indicated in picture title.
Figure 4.5. Reconstructed transverse slice of the patient from the simulated low-dose sinogram: (a) The FBP reconstruction; (b) The PWLS-GMRF reconstruction, $\beta = 3\times10^5$; (c) The PWLS-Huber reconstruction, $\beta = 3\times10^5$, $\delta=0.004$; and (d) The MRF-T60 reconstruction, $\beta = 3\times10^5$. All the images are displayed with the same window [0, 0.034] mm^{-1}.
Figure 4.6. Reconstructed transverse slice of the patient by the proposed PWLS-texture algorithm from the simulated low-dose sinogram: (a) The MRF-T58 reconstruction; (b) The MRF-T59 reconstruction; (c) The MRF-T60 reconstruction; (d) The MRF-T61 reconstruction; (e) The MRF-T62 reconstruction; and (f) The MRF-T58-62 reconstruction. The images were cropped for better visualization. All the images are displayed with the same window [0, 0.034] mm^{-1}.
Figure 4.7. NVF images of a ROI labeled in Figure 4.2(a). (a) is the reference from Figure 4.2(a). (b)-(e) are corresponding to the reconstructions in Figure 4.5(a)-(d).
Figure 4.8. Reconstructed transverse slice of two patients from full-dose acquisitions: (a) containing a lung nodule as indicated by ROI 5; (b) containing a colon polyp as indicated by ROI 4.
Figure 4.9. Reconstructed transverse slice of the patient data from the low-dose 20 mAs sinogram: (a) The FBP reconstruction; (b) The PWLS-GMRF reconstruction, $\beta = 1\times10^5$; (c) The PWLS-Huber reconstruction, $\beta = 1\times10^5$, $\delta=0.004$; and (d) The MRF-T60 reconstruction, $\beta = 1\times10^5$. All the images are displayed with the same window [0, 0.034] mm^{-1}.
Figure 4.10. Reconstructed transverse slice of the patient by the proposed PWLS-texture algorithm from the low-dose 20 mAs sinogram: (a) The MRF-T58 reconstruction; (b) The MRF-T59 reconstruction; (c) The MRF-T60 reconstruction; (d) The MRF-T61 reconstruction; (e) The MRF-T62 reconstruction; and (f) The MRF-T58-62 reconstruction. All the images are displayed with the same window [0, 0.034] mm^{-1}.

Figure 4.11. NVF images of a ROI labeled in Figure 4.9(a). The NVF images in Figure 4.11(a)-(d) are corresponding to the reconstructions in Figure 4.9(a)-(d).
Figure 5.1. One slice of the clock phantom: (a) phantom; (b) FBP reconstruction from simulated noisy sinogram; (c) FBP+NLM filtering from simulated noisy sinogram (h=0.012); (d) PWLS-NLM reconstruction from simulated noisy sinogram ($\beta=5\times10^{6}$, h=0.008); (e) PWLS-adaptiveNLM reconstruction from simulated noisy sinogram ($\beta=5\times10^{6}$, $s=5\times10^{-4}$, $t=4\times10^{-6}$); (f) PWLS-TV reconstruction from simulated noisy sinogram ($\beta=2\times10^{3}$). All the images are displayed with the same window.
Figure 5.2. Performance comparison of the four methods on reconstruction of the eight ROIs labeled in Figure 5.1(b) with RMSE and UQI metrics. The corresponding methods are illustrated in figure legend.
Figure 5.3. A reconstructed slice of the anthropomorphic torso phantom: (a) FBP reconstruction from the averaged sinogram; (b) FBP reconstruction from the 40 mAs sinogram; (c) FBP+NLM filtering from the 40 mAs sinogram (h=0.012); (d) PWLS-NLM reconstruction from the 40 mAs sinogram ($\beta=3\times10^{5}$, h=0.008); (e) PWLS-adaptiveNLM reconstruction from the 40 mAs sinogram ($\beta=3\times10^{5}$, $s=5\times10^{-4}$, $t=4\times10^{-6}$); (f) PWLS-TV reconstruction from the 40 mAs sinogram ($\beta=200$). All the images are displayed with the same window.
Figure 5.4. Performance comparison of the four methods on the reconstruction of detailed ROIs labeled in Figure 5.3(b) with RMSE and UQI metrics. The corresponding methods are illustrated in figure legend.
Figure 5.5. A reconstructed slice of the patient data: (a) FBP reconstruction from the 20 mAs sinogram; (b) FBP+NLM filtering from the 20mAs sinogram (h=0.012); (c) PWLS-NLM reconstruction from the 20 mAs sinogram ($\beta=1\times10^{5}$, h=0.008); (d) PWLS-adaptiveNLM reconstruction from the 20 mAs sinogram ($\beta=1\times10^{5}$, $s=1\times10^{-3}$, $t=4\times10^{-6}$); (e) PWLS-TV reconstruction from the 20 mAs sinogram ($\beta=50$). All the images are displayed with the same window.
Figure 6.1. The computer simulated clock phantom.
Figure 6.2. One reconstructed slice of the clock phantom by the four reconstruction methods from sparse-view acquisitions: (a1)-(a4) are reconstructed from 20 projection views; (b1)-(b4) are reconstructed from 30 projection views; (c1)-(c4) are reconstructed from 40 projection views; (d1)-(d4) are reconstructed from 50 projection views. All the images are displayed with the same window [0, 0.04] mm^{-1}.
Figure 6.3. Performance comparison of the two NLM-regularized iterative reconstruction methods on reconstruction of the three ROIs labeled in Figure 6.1 with RMSE and UQI metrics. The corresponding methods are illustrated in figure legend.
Figure 6.4. One reconstructed slice of the patient by the FBP method from 1,160 projection views.
Figure 6.5. A reconstructed slice of the patient data by the four reconstruction methods from sparse-view acquisitions: (a1)-(a4) are reconstructed from 116 projection views; (b1)-(b4) are reconstructed from 145 projection views; (c1)-(c4) are reconstructed from 232 projection views; (d1)-(d4) are reconstructed from 290 projection views. All the images are displayed with the same window [0, 0.034] mm^{-1}, and the images are cropped for better visualization.

Figure 6.6. Zoom-in views of Figure 6.5 for two detailed ROIs labeled in Figure 6.4: Figure 6.6(a) corresponds to ROI 1 and Figure 6.6(b) corresponds to ROI 3. All the images are displayed with a typical lung window [0, 0.022] mm^{-1}.

Figure 6.7. Performance comparison of the two NLM-regularized iterative reconstruction methods on reconstruction of the three ROIs labeled in Figure 6.4 with RMSE and UQI metrics. The corresponding methods are illustrated in figure legend.

List of Tables

Table 3.1. Pseudo-code for the object scale computation.
Table 3.2. MRF window size setting based on object scale, and corresponding sample window size required for MRF coefficient prediction.
Table 4.1. Texture distance between the reference full-dose image and the reconstructed low-dose images in Figure 4.5.
Table 4.2. Texture distance between the reference full-dose image in Figure 4.8(a) and the reconstructed low-dose images by the four reconstruction algorithms.
Table 4.3. Texture distance between the reference full-dose image in Figure 4.8(b) and the reconstructed low-dose images by the four reconstruction algorithms.
Table 4.4. Physicians' scoring of the reconstructed image quality in Figure 4.9 by the four reconstruction methods.
Table 5.1. Noise reduction performance of the five reconstruction methods for the clock phantom.
Table 5.2. Noise reduction performance of the five reconstruction methods for the anthropomorphic torso phantom
Table 6.1. PSNR (dB) measures of the results reconstructed by the four methods for the clock phantom
Table 6.2. PSNR (dB) measures of the results reconstructed by the four methods for patient data

List of Acronyms

2D	two-dimensional
3D	three-dimensional
4D	four-dimensional
ALARA	as low as reasonably achievable
ART	algebraic reconstruction technique
CC	correlation coefficient
CT	computed tomography
FBP	filtered back-projection
FD	full-dose
FOV	field of view
GMRF	Gaussian Markov random field
GPU	graphical processing unit
GS	Gauss-Seidel
keV	kiloelectron volt
kV	kilovoltage
LD	low-dose
MAP	maximum a posteriori
mAs	milliampere-second
ML	maximum likelihood
MRF	Markov random field
ND	normal-dose
NLM	nonlocal means
OSL	one-step-late
PET	positron emission tomography
pML	penalized maximum likelihood
PW	patch-window
PWLS	penalized weighted least-squares
RMSE	root mean squared error
ROI	region of interest
SNR	signal-to-noise ratio
SIR	statistical image reconstruction
SPECT	single photon emission computed tomography
SW	search-window
TV	total variation
UQI	universal quality index
WLS	weighted least-squares
VQ	vector quantization

Acknowledgements

First of all, I would like to thank my dissertation adviser, Prof. Jerome Liang, for his patient guidance, brilliant ideas, and financial support during my PhD study. Indeed, this dissertation would never have been completed without his enthusiasm, dedication and support. I would also like to thank my dissertation committee – Prof. Yingtian Pan, Prof. Terry Button, Prof. Gene Gindi, and Prof. William Moore for their precious time and valuable suggestions.

I would like to thank current and previous members of the Laboratory for Imaging Research and Informatics (IRIS lab): especially Dr. Jing Wang and Dr. Hongbing Lu, for their software packages on noise reduction and image reconstruction of low-dose X-ray computed tomography; Dr. Jianhua Ma, Dr. Yan Liu, Dr. Hao Han, Dr. Lihong Li, and Dr. Hongbing Zhu, for their helpful discussions on my research work; Dr. William Moore for his clinical guidance; Priya Bhattacharji for her assistance on clinical data management. Finally, I would like to thank my parents, other family members and friends, for their love, encouragement and support in my life.

This work was supported in part by the NIH/NCI under grant #CA143111 and #CA082402. Some of the text, figures and tables are reprints of the materials appeared in publications:

1. Zhang H, Han H, Wang J, Ma J, Liu Y, Moore W, and Liang Z (2014). "Deriving adaptive MRF coefficients from previous normal-dose CT scan for low-dose image reconstruction via penalized weighted least-squares minimization." Medical Physics 41(4): 041916.

2. Zhang H, Han H, Liang Z, Hu Y, Liu Y, Moore W, Ma J, and Lu H (2015). "Extracting information from previous full-dose CT scan for knowledge-based Bayesian reconstruction of current low-dose CT images." IEEE Transactions on Medical Imaging (DOI: 10.1109/TMI.2015.2498148).

3. Zhang H, Ma J, Wang J, Liu Y, Lu H, and Liang Z (2014). "Statistical image reconstruction for low-dose CT using nonlocal means-based regularization." Computerized Medical Imaging and Graphics 38(6): 423-435.

4. Zhang H, Ma J, Wang J, Liu Y, Han H, Lu H, Moore W, and Liang Z (2015). "Statistical image reconstruction for low-dose CT using nonlocal means-based regularization. Part II: An adaptive approach." Computerized Medical Imaging and Graphics 43: 26-35.

5. Zhang H, Ma J, Wang J, Liu Y, Han H, Moore W, Salerno M, and Liang Z (2014). "Adaptive nonlocal means-based regularized iterative image reconstruction for sparse-view CT." IEEE Medical Imaging Conference Record.

Based on the copyright agreement, Hao Zhang has the right to include partial/full articles in research dissertation.

Chapter 1 . Low-dose X-ray computed tomography imaging

X-ray computed tomography (CT) has been widely exploited for various clinical applications such as diagnosis and image-guided interventions. In 2013, it was estimated that 76 million CT scans were performed across the hospitals and clinics in the United States. Recent discoveries regarding the potential harmful effects of X-ray radiation including genetic and cancerous diseases have raised growing concerns to patients and the medical physics community (Brenner and Hall 2007). Consequently, low-dose CT with satisfactory image quality for specific clinical tasks is highly desirable. Many techniques and strategies have been proposed for radiation dose reduction of CT examinations to achieve the as low as reasonably achievable (ALARA) principle (Hsieh 2009). In the past decade, two classes of strategies have been widely explored for radiation dose reduction: (1) lower the X-ray tube current and exposure time (i.e., milliampere-second (mAs)) or the X-ray tube voltage (i.e., kilovoltage (kV)) settings to reduce the X-ray flux towards each detector bin; and (2) lower the number of projection views per rotation during projection data acquisition.

In this chapter, I give an introduction of CT imaging physics, including X-ray emission, its interaction with scanned patient, as well as projection data acquisition and preprocessing.

1.1 X-ray photons emission and beam filtration

The X-ray photons emitted from X-ray tube have a wide energy spectrum. In clinical CT systems, in order to reduce radiation dose and beam-hardening artifacts, a flat filter (which is often Cu/Al) is usually employed to remove the low-energy photons which mostly would be absorbed by the patients and make little contribution to the detected signals (Hsieh 2009). To further optimize radiation dose utility and improve the noise homogeneity in the projection data after traversing the body, an additional bowtie filter is also commonly used to compensate for the typically oval shape of the patient in cross section, see Figure 1.1. Also, the bowtie filter is important for reduction of beam hardening and cupping artifacts. The beam filtration by the two filters modifies the energy spectrum and intensity distribution of the emitted X-ray photons across the field of view (FOV), which will be discussed in following sections.

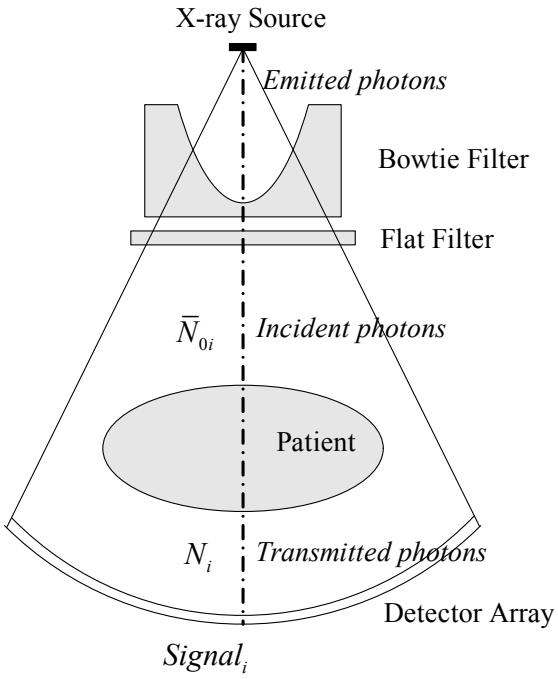

Figure 1.1. Illustration of the bowtie filter and flat filter used in clinical CT system.

1.2 Fundamentals of X-ray CT imaging

The X-ray photons after filtration and just before entering the patient are defined as the incident photons in this work. Figure 1.2 shows representative normalized energy spectra ($\int_E \Phi(E)dE = 1$) of incident X-ray photons with four different tube voltage (kV) settings. The spectra were plotted by the Spektr (Siewerdsen et al. 2004) with tungsten anode and 3mm aluminum filter. It can be observed that the maximum energy of the incident X-ray photons is determined by the tube voltage, and most of the low-energy photons (e.g., <20 keV) are removed due to the beam filtration.

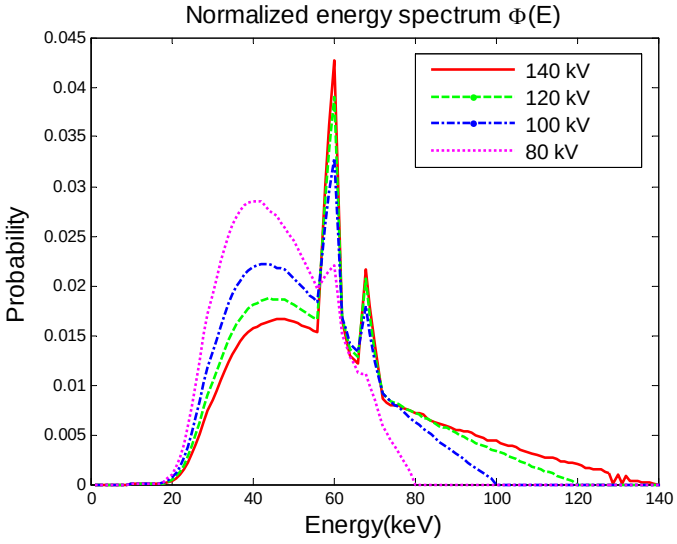

Figure 1.2. Illustration of normalized energy spectra of incident X-ray photons with tube voltage at 80, 100, 120 and 140 kV.

If we discretize the polychromatic spectrum at discrete energies E_l in energy bin l (l =1,2,...,L), we have:

$$\sum_{l=1}^{L} \Phi(E_l) = 1 \tag{1.1}$$

Although the normalized energy spectrum of the incident X-ray photons can be slightly different for each detector bin due to effects such as bowtie filtration and anode angulation, the variation is generally neglected practically (Whiting et al. 2006).

1.3 Intensity distribution of incident X-ray photons

For a given tube voltage and tube current in a given time interval (fixed kV and mAs level), the number of incident photons along the ith X-ray path, N_{0i}, is widely treated as a Poisson random variable (Macovski 1983) with a mean $\bar{N}_{0i}$. Since N_{0i} is a large number in most circumstances, the noise in the incident photon counts can often be ignored, that is, $N_{0i} \approx \bar{N}_{0i}$. $\bar{N}_{0i}$ can be estimated by the system calibration, e.g., by repeated air scans. In clinical CT systems, because of the use of bowtie filter and the heel effect, $\bar{N}_{0i}$ is not the same for all X-ray paths and is depending on the detector bin position.

Figure 1.3 reflects the distribution of $\bar{N}_{0i}$ of different detector bins across the FOV at a fixed mAs level and four different kV settings for a Siemens scanner (Manduca et al. 2009). Alternatively, if we fix the X-ray tube voltage and adjust the mAs levels, we can observe similar curves of $\bar{N}_{0i}$ as in Figure 1.3.

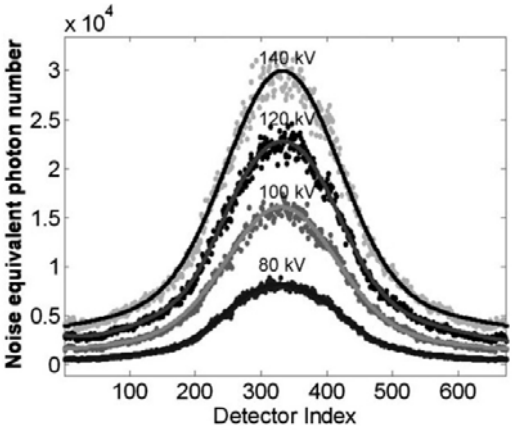

Figure 1.3. Incident photons distribution in different detector bins caused by the bowtie filter. (Figure reprinted from Manduca *et al.* 2009, Projection space denoising with bilateral filtering and CT noise modeling for dose reduction in CT, *Med. Phys.*, **36**(11): 4911–4919).

1.4 X-ray photons interaction inside the patient

The process of X-ray photons interacting with human tissue is assumed to be a binary process, where the photons are either attenuated (absorbed or/and scattered) or pass

through without any interaction (Macovski 1983). X-ray photons with different energies have different surviving probabilities. Let $\bar{N}_{0i}(E_l)$ denote the mean number of incident photons with energy E_l along the ith X-ray path. Then, the number of transmitted photons with energy E_l along the ith X-ray path, $N_i(E_l)$, is a statistical independent Poisson random variable, governed by the Lambert-Beer's law:

$$\begin{aligned} N_i(E_l) &= Poisson\left\{\bar{N}_{0i}(E_l)\bullet\exp\left[-\int_{ray\ i}\mu(E_l,\vec{r})d\vec{r}\right]\right\} \\ &= Poisson\left\{\bar{N}_{0i}\bullet\Phi(E_l)\bullet\exp\left[-\int_{ray\ i}\mu(E_l,\vec{r})d\vec{r}\right]\right\} \end{aligned} \tag{1.2}$$

where $\mu(E_l,\vec{r})$ is the attenuation coefficient of the patient at the position $\vec{r}$ at energy E_l.

Consequently, the total number of transmitted photons along the ith X-ray path can be given as:

$$N_i = \sum_{l=1}^{L} N_i(E_l) = \sum_{l=1}^{L} Poisson\left\{\bar{N}_{0i}\bullet\Phi(E_l)\bullet\exp\left[-\int_{ray\ i}\mu(E_l,\vec{r})d\vec{r}\right]\right\} \tag{1.3}$$

1.5 Signal model for energy-integrating detector

In current clinical CT systems, energy-integrating detectors are commonly used. The detected signal strength is proportional to the energy that the transmitted photons carry. Let η be the conversion or gain factor from X-ray photon energy (keV) to detected signal. The total signal strength along the ith X-ray path can be given as (La Rivière et al. 2006):

$$Signal_i = \sum_{l=1}^{L}\eta\bullet E_l\bullet Poisson\left\{\bar{N}_{0i}\bullet\Phi(E_l)\bullet\exp\left[-\int_{ray\ i}\mu(E_l,\vec{r})d\vec{r}\right]\right\} \tag{1.4}$$

The energy weighted combination of Poisson random variables in Eq. (1.4) induces the compound Poisson statistics, which has been described by Whiting et al (Whiting et al. 2006).

The detected signal is read out through detector electronics, therefore, extra uncertainty is added to the recorded signal due to the electronic noise. The electronic noise is intrinsic to the detection system and results from electronic fluctuation in the detector photodiode and other electronic components. The electronic noise is typically modeled as additive Gaussian noise, where the mean and variance reflect the detector dark current and readout noise of electronics, respectively (Hsieh 2009). The mean of the electronic noise can be determined immediately before each scan by sampling the signals in unexposed detectors over some time interval, and the variance of the electronic noise can be estimated from the sample variance of a series of dark current measurements. Consequently, the recorded signal can be described by:

$$Signal_i = \sum_{l=1}^{L}\eta\bullet E_l\bullet Poisson\left\{\bar{N}_{0i}\bullet\Phi(E_l)\bullet\exp\left[-\int_{ray\ i}\mu(E_l,\vec{r})d\vec{r}\right]\right\} + Gaussian(M_{e,i},\sigma_{e,i}^2) \tag{1.5}$$

where $M_{e,i}$ and $\sigma_{e,i}^2$ denotes the mean and variance of electronic noise for the ith projection measurement, respectively.

1.6 Degrading factors and signal preprocessing

In reality, besides the statistical noise mentioned above, there are several other factors that degrade the recorded signals, including off-focal radiation, beam hardening, scattered radiation, detector speed and afterglow, detective quantum efficiency, detector nonlinearity, crosstalk, quantization noise, etc (Hsieh 2009). As a result, the statistics of raw CT signals can be very complicated. In clinical practice, the raw CT signals are always preprocessed or calibrated by vendors for these degrading factors, while the specific operations are proprietary in nature and unavailable in the public domain. Therefore, the typically accessible projection data to academic researchers are calibrated transmitted photon counts (before log-transform), or calibrated line integrals (after log-transform) which are given by:

$$y_i \simeq \ln(\bar{N}_{0i} / N_i) \tag{1.6}$$

where y_i represents the line integral measurement along the ith X-ray path, and the approximation in Eq. (1.6) reflects an assumption that the Lambert-Beer's law can be applied to random values. Figure 1.4 illustrates the flow chart from raw CT signal acquisition, preprocessing, up to the tomographic reconstruction from calibrated transmitted photon counts or calibrated line integrals.

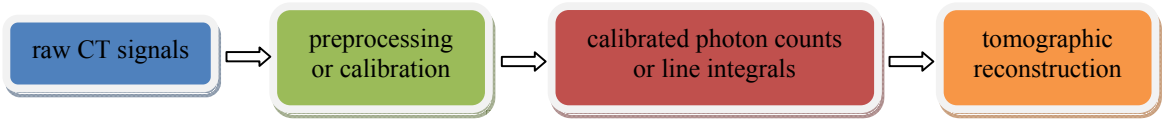

Figure 1.4. Flow chart of CT projection data preparation for image reconstruction.

Chapter 2 . Statistical image reconstruction of low-dose CT

In order to improve the CT image quality from the abovementioned low-dose acquisitions, the statistical image reconstruction (SIR) methods were proposed and have become an endeavor for almost all major vendors of clinical CT systems (Beister et al. 2012). Actually, their origins can be traced back to the early time of CT development in the decade of 1970s (Herman 1980). In parallel to the search for analytical inversion to the Radon transform for analytical CT image reconstruction, an alternative effort was devoted to discretize the Radon transform as a system of linear equations and then invert the system of linear equations for algebraic CT image reconstruction. A typical example of the alternative effort is an iterative approach to the solution of the linear equations, rather than directly inverting the system matrix, by consideration of the unique nature of re-projection and back-projection operations in tomographic imaging. This iterative approach was thereafter named the algebraic reconstruction technique (ART) (Herman 1980), and some variations were explored later, e.g., simultaneous ART. The ART was employed for image reconstruction of the original EMI CT scanners in clinic until the analytical inversion of the Radon transform was established, named FBP (Herman 1980). For low-dose CT imaging, where data statistics is an essential factor to be considered in the image reconstruction (similar to the count-limited imaging modalities of single photon emission computed tomography (SPECT) and positron emission tomography (PET)), the SIR methods are desired and iterative strategies are needed (Shepp and Vardi 1982; Lange and Carson 1984; Bouman and Sauer 1996). Essentially, the SIR methods search for the image or solution that makes the projection measurements the most probable. Instead of treating all the measurements equally, a statistical model provides different degrees of credibility/reliability among measurements according to the signal-to-noise ratio (Thibault et al. 2007). Figure 2.1 illustrates typical image reconstruction methods for X-ray CT.

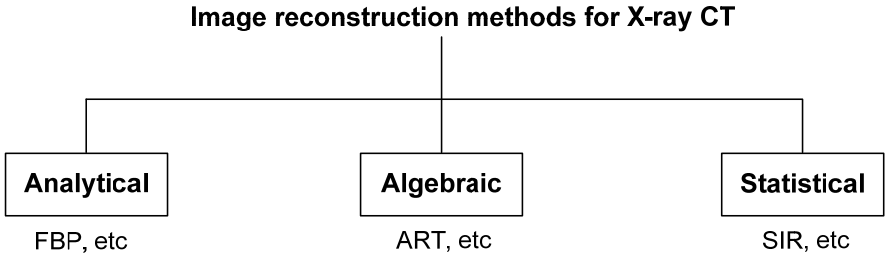

Figure 2.1. List of image reconstruction methods for X-ray CT.

Because of the explicit statistics modeling and potential dose reduction benefits, the SIR methods are likely to play a dominant role in image reconstruction development for low-dose CT in the future. However, due to the ill-posedness of the reconstruction problem, the resulting image of those SIR that directly optimizes the maximum likelihood (ML) criterion can be very noisy and unstable. Alternatively, more recent and more sophisticated SIR methods are derived from the maximum a posteriori (MAP) estimation from the given the measurements, which

consists of two terms in the objective function: the data-fidelity term modeling the statistics of measured data, and the regularization term incorporating prior knowledge or expected properties of the image to be reconstructed. The statistical modeling of the projection measurements is a prerequisite for building the data-fidelity term, and the regularization term also has a strong influence on the quality of reconstructed images. In this chapter, I illustrate the statistical models of CT projection measurements and derive the SIR framework for low-dose CT accordingly.

2.1 Statistical modeling on projection measurements

In clinical CT systems, the raw signals from detectors are always preprocessed by CT vendors for various degrading factors, while the raw signals (considered proprietary by vendors) are rarely accessible to academic researchers (Hsieh 2009). Therefore, the researchers generally focus on investigating the properties of preprocessed CT signals in the past decades. Commonly, the accessible projection data are calibrated transmitted photon counts (before log-transform) or calibrated line integrals (after log-transform).

2.1.1 Calibrated transmitted photon counts

According to the analysis in Chapter 1, the calibrated transmitted photon counts along the *i*th X-ray path can be expressed as (Ma et al. 2012):

$$N_i \sim compoundPoisson(\bar{N}_i, \Phi) + Gaussian(M_{e,i}, \sigma_{e,i}^2) \tag{2.1}$$

While the mathematical formula of the compound Poisson distribution has been explicitly derived (Whiting et al. 2006), the lack of analytical probability density function (PDF) expression impedes its use in SIR method development. Additionally, this model has more challenges when the electronic noise is considered, which makes this exact model impractical for SIR.

Practically, this exact model can be well-approximated by a simple Poisson noise model assuming monochromatic X-ray source, and is widely used in the SIR methods:

$$N_i \sim Poisson(\bar{N}_i) \tag{2.2}$$

Although the simple Poisson model is acceptable in most cases, the influence of electronic noise becomes non-neglectable, and has been considered as an important factor affecting the image quality (Xu and Tsui 2009) under very low-flux acquisitions (transmitted photon counts are extremely low). In clinical CT systems, in order to reduce the effect of detector dark current, the mean of electronic noise is often calibrated to be zero in practice. Also, the variance of electronic noise is assumed to be the same for all X-ray paths and thus the index can be removed. As a result, the statistics of the calibrated transmitted photon count along the *i*th X-ray path can be described by (Snyder et al. 1993; Snyder et al. 1995):

$$N_i \sim Poisson(\bar{N}_i) + Gaussian(0, \sigma_e^2) \tag{2.3}$$

However, the likelihood function of the 'Poisson+Gaussian' model in Eq. (2.3) is still analytically intractable. To circumvent this problem, a shifted Poisson approximation can be exploited to match the first two statistical moments (Yavuz and Fessler 1998). That is, the random variable $\hat{N}_i = \left[N_i + \sigma_e^2 \right]_+$ can have the variance equal to its mean $(\bar{N}_i + \sigma_e^2)$. Based on the relationship of variance equal to the mean, we assume that the shifted random variable $\hat{N}_i$ follows Poisson distribution:

$$\hat{N}_i = \left[N_i + \sigma_e^2 \right]_+ \sim Poisson(\bar{N}_i + \sigma_e^2) \tag{2.4}$$

where $[x]_+ = x$ if $x > 0$ and is 0 otherwise.

2.1.2 Calibrated line integrals

The noise property of the calibrated line integrals has been investigated by analyzing experimental data of a physical phantom from repeated scans. The statistical analysis showed that the calibrated line integrals can be fitted approximately by a Gaussian distribution with a nonlinear signal-dependent variance (Lu et al. 2002; Li et al. 2004):

$$y_i \sim Gaussian(\bar{y}_i, \sigma_{y_i}^2) \tag{2.5}$$

With the Poisson noise model of the transmitted photon counts in Eq. (2.2) and the Taylor's expansion, it has been shown that the variance of the line integral y_i is given by:

$$\sigma_{y_i}^2 = 1/\bar{N}_i = \exp(\bar{y}_i)/\bar{N}_{0i} \tag{2.6}$$

Similarly, with the 'Poisson+Gaussian' noise model of the transmitted photon counts in Eq. (2.3), the variance of the line integral can be described by (Thibault et al. 2006; Ma et al. 2012):

$$\sigma_{y_i}^2 = \frac{\bar{N}_i + \sigma_e^2}{\bar{N}_i^2} = \frac{1}{\bar{N}_{0i}}\exp(\bar{y}_i)\left(1 + \frac{\sigma_e^2}{\bar{N}_{0i}}\exp(\bar{y}_i)\right) \tag{2.7}$$

Essentially, Eqs. (2.6) and (2.7) still have the monochromatic X-ray source assumption because of the models from which they are derived. Since the polychromatic nature of X-ray generation does not change the mean and only affect the variance of the calibrated line integrals, Eqs. (2.6) and (2.7) actually have the potential to consider the polychromatic nature by replacing $1/\bar{N}_{0i}$ with a factor Γ_i, where Γ_i is no longer exactly equal to $1/\bar{N}_{0i}$ but can be measured by repeated scans and experimental data fitting (Li et al. 2004).

2.2 Discrete forward models

Under the assumption of monochromatic X-ray generation, the CT projection measurement can be expressed as:

$$\bar{y}_i = \ln(\bar{N}_{0i}/\bar{N}_i) = \int_{ray\ i} \mu(\vec{r})d\vec{r} \approx \sum_j a_{ij}\mu_j = [\mathbf{A}\boldsymbol{\mu}]_i \tag{2.8}$$

or described as a discrete linear system:

$$\bar{\mathbf{y}} = \mathbf{A}\boldsymbol{\mu} \tag{2.9}$$

where $\bar{\mathbf{y}} \in \mathbb{R}^{I\times 1}$ denotes the vector of expected line integrals, and I is the total number of projection measurements; $\boldsymbol{\mu} \in \mathbb{R}^{J\times 1}$ represents the vector of attenuation coefficients of the object to be reconstructed, and J is the total number of image voxels; $\mathbf{A} \in \mathbb{R}^{I\times J}$ is the projection matrix and its element a_{ij} represents the contribution of voxel j to the ith projection ray. In CT imaging, the projector mainly accounts for the geometry of the imaging system. A variety of projectors as well as strategies to accelerate the process have been proposed, comprehensive review of which are out of the scope of this paper. Herein, we briefly review three commonly used approaches to calculate the projection matrix: (1) *voxel-driven* (or *pixel-driven*, in 2D presentation), which connects a line from the focal spot through the center of concerned voxel and projects to the detector (Herman 1980); (2) *ray-driven*, which casts one ray (or several rays) from the focal spot to the center (or boundaries) of the detector bin of interest and utilize the intersected length, intersected area (for 2D case), or intersected volume (for 3D case) as the weight (Herman 1980);

(3) *distance-driven*, which maps the boundaries of each voxel and detector bin onto a common axis and employ the length of overlap as the weight (De Man and Basu 2004). Figure 2.2 illustrates the three projection models in 2D case. Although there are potential benefits of modeling the focal spot size, it is noted that, for the projectors in Figure 2.2, the focal spot is generally assumed to be infinitely small point for simplicity.

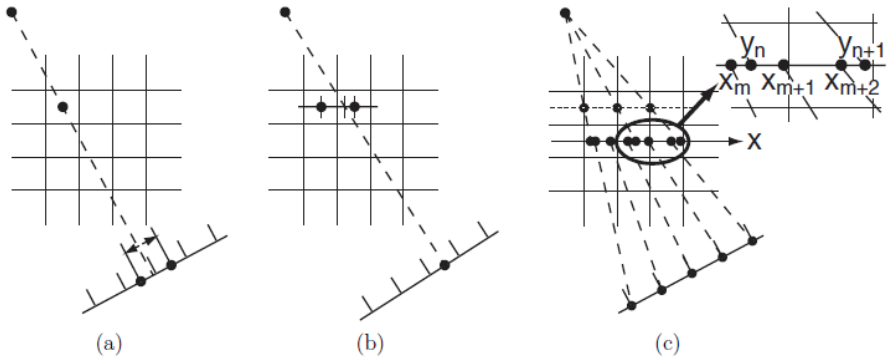

Figure 2.2. (a) pixel-driven projection-backprojection; (b) ray-driven projection-backprojection; (c) distance-driven projection-backprojection. (Figure reprinted from DeMan and Basu 2004, Distance-driven projection and backprojection in three dimensions, *Phys. Med. Biol.*, **49**: 2463–2475)

2.3 Maximum likelihood (ML)/weighted least-squares (WLS) criterions

2.3.1 Poisson model for calibrated transmitted photon counts

Let $\mathbf{N} \in \mathbb{R}^{I\times 1}$ denote the vector of calibrated transmitted photon counts. Assuming the measurements among different bins are statistically independent, the likelihood function of the joint probability distribution, given a distribution of the attenuation coefficients, can be written as:

$$P(\mathbf{N}\,|\,\boldsymbol{\mu}) = \prod_i \frac{(\bar{N}_i)^{N_i}\exp(-\bar{N}_i)}{N_i!} \tag{2.10}$$

Due to the logarithm's monotonicity, we can take the natural logarithm, which will not change the location of the maximum. Thus, the log-likelihood function $L(\mathbf{N}\,|\,\boldsymbol{\mu})$, can be written as:

$$L(\mathbf{N}\,|\,\boldsymbol{\mu}) = \ln P(\mathbf{N}\,|\,\boldsymbol{\mu}) = \sum_i (N_i \ln \bar{N}_i - \bar{N}_i - \ln N_i!) \tag{2.11}$$

Ignoring the constant terms which will not change the optimization solution, we can obtain:

$$L(\mathbf{N}\,|\,\boldsymbol{\mu}) = -\sum_i (\bar{N}_{0i}\,\mathrm{e}^{-\bar{y}_i} + N_i\bar{y}_i) = -\sum_i (\bar{N}_{0i}\,\mathrm{e}^{-[\mathbf{A}\boldsymbol{\mu}]_i} + N_i[\mathbf{A}\boldsymbol{\mu}]_i) \tag{2.12}$$

where Eq. (2.12) is called the ML criterion.

A second-order Taylor's expansion can be applied to $g_i(\bar{y}_i) = N_{0i}\,\mathrm{e}^{-\bar{y}_i} + N_i\bar{y}_i$ around the measured line integral y_i (Sauer and Bouman 1993), that is:

$$
\begin{aligned}
g_i(\bar{y}_i) = \bar{N}_{0i}\, \mathrm{e}^{-\bar{y}_i} + N_i \bar{y}_i &\approx g_i(y_i) + \frac{g_i^{'}(y_i)}{1!}(\bar{y}_i - y_i) + \frac{g_i^{''}(y_i)}{2!}(\bar{y}_i - y_i)^2 \\
&= (N_i + N_i \ln \frac{\bar{N}_{0i}}{N_i}) + 0 + \frac{N_i}{2}(\bar{y}_i - y_i)^2
\end{aligned}
\tag{2.13}
$$

Therefore, ignoring the constant and irrelevant terms, the log-likelihood in Eq. (2.12) can be approximated as:

$$
L(\mathbf{y} \mid \boldsymbol{\mu}) \approx -\sum_i \left\{ \frac{N_i}{2}(y_i - \bar{y}_i)^2 \right\} = -\frac{1}{2}(\mathbf{y} - \bar{\mathbf{y}})^T \boldsymbol{\Lambda}(\mathbf{y} - \bar{\mathbf{y}}) = -\frac{1}{2}(\mathbf{y} - \mathbf{A}\boldsymbol{\mu})^T \boldsymbol{\Lambda}(\mathbf{y} - \mathbf{A}\boldsymbol{\mu}) \tag{2.14}
$$

where $\boldsymbol{\Lambda} = diag\{N_i\}$ depends on the random variable N_i. The approximate log-likelihood in Eq. (2.14) has computational advantages compared to Eq. (2.12) due to the quadratic form, but it may be biased when N_i is close to zero. Despite the potential shortcomings, the approximate log-likelihood has been used successfully in CT applications, and its negative is also widely known as the WLS criterion.

2.3.2 Poisson+Gaussian model for calibrated transmitted photon counts

The likelihood function of the 'Poisson+Gaussian' model in Eq. (2.3) is analytically intractable. To circumvent this problem, a shifted Poisson approximation in Eq. (2.4) is exploited to match the first two statistical moments (Yavuz and Fessler 1998). With the shifted Poisson model and ignoring the constant and irrelevant terms, the corresponding log-likelihood function similar to that in Eq. (2.12) can be written as:

$$
\begin{aligned}
L(\mathbf{N} \mid \boldsymbol{\mu}) &= \sum_i \left\{ \left[N_i + \sigma_e^2 \right]_+ \ln(\bar{N}_i + \sigma_e^2) - (\bar{N}_i + \sigma_e^2) \right\} \\
&= \sum_i \left\{ \left[N_i + \sigma_e^2 \right]_+ \ln(\bar{N}_{0i}\, \mathrm{e}^{-\bar{y}_i} + \sigma_e^2) - (\bar{N}_{0i}\, \mathrm{e}^{-\bar{y}_i} + \sigma_e^2) \right\} \\
&= \sum_i \left\{ \left[N_i + \sigma_e^2 \right]_+ \ln(\bar{N}_{0i}\, \mathrm{e}^{-[\mathbf{A}\boldsymbol{\mu}]_i} + \sigma_e^2) - (\bar{N}_{0i}\, \mathrm{e}^{-[\mathbf{A}\boldsymbol{\mu}]_i} + \sigma_e^2) \right\}
\end{aligned}
\tag{2.15}
$$

where Eq. (2.15) is the ML criterion with consideration of the electronic noise.

Similar to the Taylor's expansion in Eq. (2.13) and omitting the constant and irrelevant terms, the log-likelihood in Eq. (2.15) can be approximated as:

$$
L(\mathbf{y} \mid \boldsymbol{\mu}) \approx -\frac{1}{2}\sum_i \left\{ \frac{N_i^2}{N_i + \sigma_e^2}(y_i - \bar{y}_i)^2 \right\} = -\frac{1}{2}(\mathbf{y} - \bar{\mathbf{y}})^T \boldsymbol{\Lambda}(\mathbf{y} - \bar{\mathbf{y}}) = -\frac{1}{2}(\mathbf{y} - \mathbf{A}\boldsymbol{\mu})^T \boldsymbol{\Lambda}(\mathbf{y} - \mathbf{A}\boldsymbol{\mu}) \tag{2.16}
$$

where $\boldsymbol{\Lambda} = diag\left\{ \frac{N_i^2}{N_i + \sigma_e^2} \right\}$ depends on the random variable N_i. Also, the negative of Eq. (2.16) is called as the WLS criterion in consideration of the electronic noise.

It is noted that if we neglect the influence of the electronic noise ($\sigma_e^2 = 0$), the diagonal matrix $\boldsymbol{\Lambda}$ in Eq. (2.16) reduces to $\boldsymbol{\Lambda} = diag\{N_i\}$, which is the same as that in Eq. (2.14).

2.3.3 Gaussian model for calibrated line integrals

Similarly, assuming the calibrated line integrals among different detector bins are statistically independent, the likelihood function of the joint probability distribution, given a distribution of the attenuation coefficients, can be written as:

$$P(\mathbf{y}\,|\,\boldsymbol{\mu}) = \frac{1}{Z_0}\prod_i \exp\left[-\frac{(y_i-\bar{y}_i)^2}{2\sigma_{y_i}^2}\right] \tag{2.17}$$

where Z_0 is a normalizing constant.

Then, ignoring the constant and irrelevant terms, the log-likelihood function can be written as:

$$L(\mathbf{y}\,|\,\boldsymbol{\mu}) = \ln P(\mathbf{y}\,|\,\boldsymbol{\mu}) = \sum_i \left\{-\frac{(y_i-\bar{y}_i)^2}{2\sigma_{y_i}^2}\right\} = -\frac{1}{2}(\mathbf{y}-\bar{\mathbf{y}})^T\boldsymbol{\Lambda}(\mathbf{y}-\bar{\mathbf{y}}) = -\frac{1}{2}(\mathbf{y}-\mathbf{A}\boldsymbol{\mu})^T\boldsymbol{\Lambda}(\mathbf{y}-\mathbf{A}\boldsymbol{\mu}) \tag{2.18}$$

where the matrix $\boldsymbol{\Lambda}$ is diagonal and $\boldsymbol{\Lambda}$=diag$\{1/\sigma_{y_i}^2\}$.

With the monochromatic X-ray source assumption, the variance of the calibrated line integral can be given as:

$$\sigma_{y_i}^2 = 1/\bar{N}_i \text{, or } \sigma_{y_i}^2 = \frac{\bar{N}_i + \sigma_e^2}{\bar{N}_i^2} \tag{2.19}$$

The WLS criterion derived in Eq. (2.18) is consistent with that in Eq. (2.14) and Eq. (2.16) with the approximation of $\bar{N}_i \approx N_i$. It shall be noted that this approximation holds only if the mean value $\bar{N}_i$ is relatively large. In the cases of ultra low-dose CT imaging and presence of the electronic noise, this approximation may not hold. The gain of the matrix $\boldsymbol{\Lambda}$ of (2.18) over that of (2.14) was analyzed theoretically (Xu and Tsui 2014). In practice, since the variance in matrix $\boldsymbol{\Lambda}$ of (2.18) depends on the unknown mean $\bar{N}_i$, it is typically re-calculated during iterative image reconstruction, and the criterion in Eq. (2.18) is sometimes called re-weighted least-squares (Wang et al. 2006).

2.4 Maximum a posteriori (MAP) estimation

Mathematically, low-dose CT image reconstruction is an ill-posed problem due to the presence of noise and other inconsistencies in the projection data. Therefore, the image estimation that directly optimizes the ML criterion can be very noisy and unstable. So researchers reformulate this problem with the MAP estimation by posing a prior term to penalize or regularize the solution. The prior term enables us to incorporate available information or expected properties of the image to be reconstructed.

Mathematically, the MAP estimator can be expressed as:

$$\boldsymbol{\mu}^* = \arg\max_{\boldsymbol{\mu}} P(\boldsymbol{\mu}\,|\,\mathbf{N}) \tag{2.20}$$

According to the Bayesian law:

$$P(\boldsymbol{\mu}\,|\,\mathbf{N}) = \frac{P(\mathbf{N}\,|\,\boldsymbol{\mu})P(\boldsymbol{\mu})}{P(\mathbf{N})} \tag{2.21}$$

By taking the logarithm and omitting the irrelevant term, the MAP estimator can be simplified to:

$$\boldsymbol{\mu}^* = \arg\max_{\boldsymbol{\mu}} [\ln P(\boldsymbol{\mu}\,|\,\mathbf{N})] = \arg\max_{\boldsymbol{\mu}} [L(\boldsymbol{\mu}\,|\,\mathbf{N})] = \arg\max_{\boldsymbol{\mu}} [L(\mathbf{N}\,|\,\boldsymbol{\mu}) + \ln P(\boldsymbol{\mu})] \tag{2.22}$$

By replacing the log *a priori* probability $\ln P(\boldsymbol{\mu})$ with a more general form, we have:

$$\boldsymbol{\mu}^* = \arg\max_{\boldsymbol{\mu}} [L(\mathbf{N}\,|\,\boldsymbol{\mu}) - R(\boldsymbol{\mu})] = \arg\max_{\boldsymbol{\mu}} [L(\mathbf{N}\,|\,\boldsymbol{\mu}) - \beta U(\boldsymbol{\mu})] \tag{2.23}$$

where $U(\boldsymbol{\mu})$ denotes a penalty, and $\beta > 0$ is a scalar control parameter which allows one to tune the MAP (or penalized ML (pML)) estimation for a specific noise-resolution tradeoff. When β goes to zero, the reconstructed image from the MAP estimation approaches the ML estimation.

From the Tikhonov regularization point of view, the MAP estimation can be considered as an objective function consisting of two terms: a data-fidelity term (e.g., the log-likelihood) modeling the statistics of projection measurements, and a regularization term (e.g., the log-prior) incorporating prior knowledge or expected properties of the image to be reconstructed.

The log-likelihood functions in Eqs. (2.12) (2.14) (2.16) (2.18) are concave functions of $\boldsymbol{\mu}$, therefore, the resulting objective functions in Eq. (2.23) would be concave if and only if $U(\boldsymbol{\mu})$ is a convex function of $\boldsymbol{\mu}$. The log-likelihood function in Eq. (2.15) is not concave in $\boldsymbol{\mu}$ for $\sigma_e^2 > 0$, so the corresponding objective function in Eq. (2.23) would not be concave in $\boldsymbol{\mu}$ anyway. Global maximum can be found for concave objective functions, while only local maximum can be achieved for others.

In summary, the SIR of low-dose CT can be considered to estimate the attenuation map by maximizing the MAP (or pML) criterion with a non-negativity constraint (using the calibrated transmitted photon counts):

$$\boldsymbol{\mu}^* = \arg\max_{\mu \geq 0} \left[L(\mathbf{N} \mid \boldsymbol{\mu}) - \beta U(\boldsymbol{\mu}) \right] \tag{2.24}$$

or directly minimizing the penalized WLS (PWLS) criterion (using the calibrated line-integrals):

$$\boldsymbol{\mu}^* = \arg\max_{\mu \geq 0} \left[L(\mathbf{y} \mid \boldsymbol{\mu}) - \beta U(\boldsymbol{\mu}) \right] = \arg\min_{\mu \geq 0} \left[\frac{1}{2} (\mathbf{y} - \mathbf{A}\boldsymbol{\mu})^T \boldsymbol{\Lambda} (\mathbf{y} - \mathbf{A}\boldsymbol{\mu}) + \beta U(\boldsymbol{\mu}) \right] \tag{2.25}$$

where $L(\mathbf{N} \mid \boldsymbol{\mu})$ is defined in Eqs. (2.12) (1.15), and $L(\mathbf{y} \mid \boldsymbol{\mu})$ is defined in Eqs. (1.14) (2.16) (2.18).

Chapter 3. Deriving voxel-specific MRF coefficients from previous normal-dose CT scan for low-dose CT reconstruction

Repeated CT scans are required for some clinical applications such as image-guided interventions. To optimize radiation dose utility, a normal-dose scan is often first performed to set up reference, followed by a series of low-dose scans for intervention. One common strategy to achieve the low-dose scan is to lower the X-ray tube current and exposure time settings in the scanning protocol, but the resulting image quality by the conventional filtered back-projection (FBP) method may be severely degraded due to the excessive noise. Statistical image reconstruction has shown the potential to significantly improve the image quality from low-mAs acquisitions, where the penalty plays an important role. In this work, we explore an adaptive Markov random field (MRF)-based penalty term by utilizing previous normal-dose scan to improve the subsequent low-dose scans image reconstruction.

3.1 Introduction

In the applications with repeated CT scans, previous scan can be exploited as prior information due to the similarity among the reconstructed image series of the scans. These scans generally contain the same anatomical structures. While somewhat misalignment or deformation may occur among the image series, they can be mitigated through registration of the image series and/or modeling the effects in constructing the cost function. Using the reconstruction from previous normal-dose scan to improve the follow-up low-dose scan reconstructions has become a research interest recently. For instance, Yu et al (Yu et al. 2009) proposed a previous scan-regularized reconstruction (PSRR) method for perfusion CT imaging by replacing the unchanged regions of the low-dose CT image with the corresponding embodiments in the previous normal-dose reconstruction and employing a nonlinear noise filtration in the remaining regions. Ma et al (Ma et al. 2011) and Xu and Muller (Xu and Mueller 2012) investigated restoration on the low-dose CT images with the help of the previous normal-dose image via the nonlocal means (NLM) noise filtration algorithm. The above efforts also explored the use of the previous scan as a penalty for regularized iterative image reconstructions. For instance, the studies (Nett et al. 2009; Lauzier et al. 2012) incorporated a prior image (averaging over FBP reconstructions from different time frames) as a penalty into their prior image-constrained compressed sensing (PICCS) framework for time-resolved sparse-view CT reconstruction. Tian et al (Tian et al. 2011) presented a temporal NLM regularization for low-dose four-dimensional (4D) CT reconstruction, where the reconstruction of the current frame image utilizes the previous iteration results of the two neighboring frames. Ma et al (Ma et al. 2012) proposed a low-mAs perfusion CT image reconstruction method by incorporating a previous normal-dose unenhanced image into the regularization term for the subsequent reconstruction of the low-dose enhanced CT images. Recently, Wang et al (Wang et al. 2012) explored the potential of using a high

quality image to estimate the MRF weighting coefficients for penalized reconstruction of its corresponding image from noisy (or low-dose) data. They exploited an 11×11 MRF window and estimated the MRF weighting coefficients from a high-quality bone-region sample image, and then incorporated the single set of MRF coefficients into an iterative CT reconstruction framework to preserve details in the bone structures. Inspired by this recent work, this study aims to incorporate a previous normal-dose CT scan into the quadratic functional form, while considering adaptively the entire local region for the MRF weighting coefficients, for the purpose of reconstructing the subsequent low-dose CT images. In this way, both the MRF window size and the corresponding coefficients are adaptively estimated for better reflection of the prior information in both space and frequency domains. Thus, it is expected that with the proposed penalty term from the previous normal-dose scan, the reconstruction from the follow-up low-dose scans will be substantially improved.

3.2 Markov random field (MRF) model-based regularization

Under the MRF model, a family of regularization terms is widely used for iterative image reconstruction:

$$U(\boldsymbol{\mu}) = \sum_{j} \sum_{m \in W_j} b_{jm} \phi(\mu_j - \mu_m) \tag{3.1}$$

where index j runs over all the pixels in the image domain, W_j denotes a small fixed neighborhood window (typically 8 neighbors in the 2D case) of the jth image pixel, and b_{jm} is the weighting coefficient that indicates the interaction degree between pixel j and pixel m. Usually the weighting coefficient is considered to be inversely proportional to the Euclidean distance between the two pixels. Thus, in 2D case, b_{jm}=1 for the four horizontal and vertical neighboring pixels, $b_{jm}=1/\sqrt{2}$ for the four diagonal neighboring pixels, and b_{jm}=0 otherwise. In this study, the normalized form was used to make $\sum_{m \in W_j} b_{jm} = 1$, which is given as:

$$\begin{bmatrix} \frac{1}{4+4\sqrt{2}} & \frac{1}{4+2\sqrt{2}} & \frac{1}{4+4\sqrt{2}} \\ \frac{1}{4+2\sqrt{2}} & 0 & \frac{1}{4+2\sqrt{2}} \\ \frac{1}{4+4\sqrt{2}} & \frac{1}{4+2\sqrt{2}} & \frac{1}{4+4\sqrt{2}} \end{bmatrix} \text{ or } \begin{bmatrix} 0.104 & 0.146 & 0.104 \\ 0.146 & 0 & 0.146 \\ 0.104 & 0.146 & 0.104 \end{bmatrix} \tag{3.2}$$

And ϕ denotes a potential function, which can be given as:

$$\phi(\Delta) = \Delta^2 \quad , \quad \text{or} \quad \phi(\Delta) = \begin{cases} \Delta^2 & |\Delta| \le \delta \\ 2\delta |\Delta| - \delta^2 & |\Delta| > \delta \end{cases} \tag{3.3}$$

where the former corresponds to the Gaussian MRF penalty, and the latter corresponds to the Huber MRF penalty that introduces an adjustable parameter δ to balance the desired degree on the regional smoothness and edge sharpness.

3.3 The proposed adaptive MRF regularization

Inspired by the work of Wang et al (Wang et al. 2012), we investigate the design of an adaptive MRF regularization term which exploits space-variant MRF window size and adaptive weighting coefficients, which are predicted from local sampling window of a

normal-dose scan, to help the following low-dose scan CT reconstruction. The proposed adaptive MRF regularization term is defined as:

$$U(\boldsymbol{\mu}) = \sum_{j} \sum_{m \in AW_j} b_{jm}^{ND\_predict} (\mu_j - \mu_m)^2 \tag{3.4}$$

where AW_j is no longer a fixed neighborhood window, but varies depending on the object scale (to be described later). Also, the coefficients $b_{jm}^{ND\_predict}$ are no longer constant but adaptively predicted from the previous normal-dose scan. The symbols AW and ND are short for adaptive-window and normal-dose, respectively. AW_j and $b_{jm}^{ND\_predict}$ are determined through the following three steps:

3.3.1 Computation of object scale

The scale at every pixel j, $K(j)$, is defined as the radius of the largest hyperball (or hypercirle in a 2D case) centered at the pixel j such that all pixels within the ball satisfied a predefined image intensity homogeneity criterion (Saha and Udupa 2000). For any pixel j in a given image, a digital ball of radius r centered at j is the set of pixels:

$$B_r(j) = \{h \mid \|h - j\| \le r\} \tag{3.5}$$

where $\|h - j\|$ denotes the Euclidean distance between j and h. Then, a fraction $FO_r(j)$ ("fraction of object") is defined. It indicates the fraction of the ball boundary occupied by a region which is sufficiently homogeneous with j, and can be described by:

$$FO_r(j) = \frac{\sum_{h \in B_r(j) - B_{r-1}(j)} H_\psi(\mu_j - \mu_h)}{|B_r(j) - B_{r-1}(j)|} \tag{3.6}$$

where $|B_r(j) - B_{r\text{-}1}(j)|$ is the number of pixels in the region $B_r(j) - B_{r\text{-}1}(j)$, and H_ψ is a homogeneity function defined by:

$$H_\psi(x) = \exp\left(-\frac{x^2}{2\sigma_\psi^2}\right) \tag{3.7}$$

where σ_ψ is the region-homogeneity parameter and computed following the method as in (Saha and Udupa 2000).

Thus, the scale at pixel j, $K(j)$, is computed as follows: $K(j)$ is initialized as one. Then we iteratively increase the ball radius r by one and check the value of $FO_r(j)$. When the first time this fraction falls below t_s (usually set to be 85%), we consider that the ball contains an object region different from that to which j belongs and set the scale value of $K(j)$ as $r - 1$. Table 3.1 lists the pseudo-code for the object scale computation.

Table 3.1. Pseudo-code for the object scale computation.

```
For each pixel j:
begin
    r = 1;
    while FO_r(j) > t_s (e.g., 85%)
        r = r+1;
    end
    K(j) = r-1;
end
```

Figure 3.1(b) illustrates an example of the object scale map calculated from one transverse CT slice of the anthropomorphic torso phantom of Figure 3.1(a). The black/grey dots indicate pixels with low sclae values, while the white regions are relative uniform with high scale values.

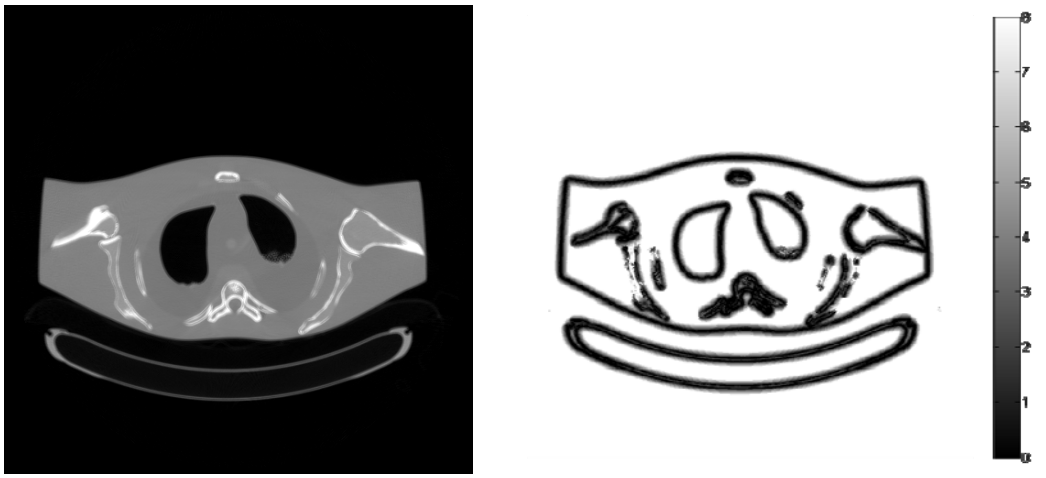

(a) (b)

Figure 3.1. (a) One transverse slice of the anthropomorphic torso phantom; (b) the corresponding object scale map of the CT image in (a).

3.3.2 Determination of MRF window size and sample window size

For each pixel in the FBP reconstructed image from the normal-dose scan, an explicit MRF window can be modeled with its size determined by the object scale, which is a quantitative measure of local uniformity as described above. In terms of signal processing, when the neighborhood of a specific pixel tends to be homogeneous (i.e., when its object scale is large), there exists a small spread of frequency spectrum, and vice versa. Therefore, a lower-order MRF, penalizing only differences among immediately neighboring pixels, is adequate to model a small spread of frequency spectrum (i.e., when the object scale is large), while a higher-order MRF is required when the spread of frequency spectrum is large (i.e., when the object scale is small). The correspondence between the object scale and MRF window size was empirically set in this study in a 2D presentation, as shown in Table 3.2.

Table 3.2. MRF window size setting based on object scale, and corresponding sample window size required for MRF coefficient prediction.

Object scale	MRF window size	Number of coefficients to be predicted	Sample size needed to reach 90% prediction power	Actual sample window size used
>7	3×3	8	136	13×13
6-7	5×5	24	206	15×15
4-5	7×7	48	278	17×17
2-3	9×9	80	355	19×19
0-1	11×11	120	435	21×21

Subsequently, assuming similar frequency spectrums among nearby pixels, the MRF coefficients for each pixel were predicted adaptively from a local sample window. Statistically, to ensure the prediction power of the least-squares linear regression with a certain number of predictors (i.e., the number of MRF coefficients to be predicted), the required sample size needs to be determined. Given a type I error rate of less than 5%, the sample size was calculated using the G*Power software (Faul et al. 2009) to achieve a prediction power of at least 90% at a medium effect size (Cohen's $f^2 = 0.15$). The actual sample window size utilized in this study was designed to be a bit larger than the required sample size, as summarized in Table 3.2.

Hence, the prediction of adaptive MRF coefficients depends on an adaptive MRF window size and the corresponding sample window size. Figure 3.2 shows an example of the MRF window as well as the prediction sample window for a pixel (labeled with green marker) whose object scale is 4-5. According to Table 3.2, a 7×7 MRF window (labeled with gray marker) and 17×17 sample window should be adopted for this pixel. Similar MRF/sample window selection strategy based on Table 3.2 is performed for pixels in the 2D image one-by-one.

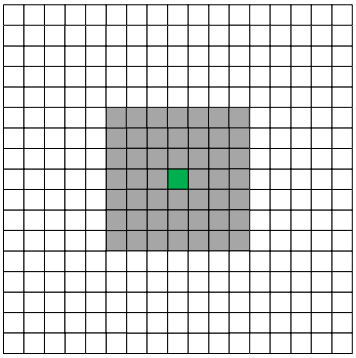

Figure 3.2. Example illustration of the MRF/sample window designed for one single pixel (labeled with green marker). The gray window represents the 7×7 MRF window, and the white window is the corresponding 17×17 sample window.

3.3.3 Prediction of MRF coefficients

After we have obtained the MRF and sample window sizes for each pixel in the FBP reconstructed image slices of the normal-dose CT scan, we can predict the corresponding MRF coefficients for each pixel via least-squares regression as every pixel can be predicted from a linear combination of its clique-mates. The clique-mates of current pixel here are the neighbors within the MRF window. According to (Wang et al. 2012), the least-squares predicted coefficients for the clique-mates can be formulated as:

$$\mathbf{b}_j^{ND\_predict} = \arg\min_{\mathbf{b}_j} \sum_{k \in S_j} (\mu_k^{ND} - \mathbf{b}_j{}^T \boldsymbol{\mu}_{AW_k}^{ND})^2 = \left[\sum_{k \in S_j} (\boldsymbol{\mu}_{AW_k}^{ND} (\boldsymbol{\mu}_{AW_k}^{ND})^T) \right]^{-1} \left[\sum_{k \in S_j} (\boldsymbol{\mu}_{AW_k}^{ND} \mu_k^{ND}) \right] \quad (3.8)$$

where $\boldsymbol{b}_j$ is the vector of MRF coefficients for the neighbors of pixel j within the MRF window, S_j is the sample window of pixel j, AW_k represents the set of neighbors for pixel k within the MRF window and $\boldsymbol{\mu}_{AW_k}$ is the vector of corresponding attenuation value for them. Herein, the expression $\sum_{k \in S_j} (\boldsymbol{\mu}_{AW_k}^{ND} (\boldsymbol{\mu}_{AW_k}^{ND})^T)$ is the sample autocorrelation matrix, while

$\sum_{k\in S_j}(\boldsymbol{\mu}_{AW_k}^{ND}\mu_k^{ND})$ is the sample cross-correlation vector. The symbol *ND* was defined before as the short for normal-dose.

In order to solve Eq. (3.8), the sample autocorrelation matrix is required to be of full rank and reversible. This condition is met for all the pixels except for some whose object scale is relatively large, where the intensity homogeneity leads to the multi-collinearity of the sample space. In our experiments, we empirically set a robust threshold on the object scale to be 7. For those pixels with scale above this threshold, their MRF window size should be 3 ×3 according to Table 3.2, and therefore, we set their weighting coefficients the same as that for the conventional GMRF. For the pixels with object scale under the preset threshold, the MRF coefficients were estimated directly using Eq. (3.8). And it is worth noting that the sum of predicted MRF coefficients $\mathbf{b}_j^{ND\_predict}$ for the pixel *j* using Eq. (3.8) is close to 1 (e.g., 0.95-1.05).

3.4 Summary of presented reconstruction method

With the WLS criterion and the newly designed quadratic-form MRF regularization presented above, our PWLS iterative reconstruction scheme for low-dose CT can be summarized as follows:

$$\boldsymbol{\mu}^* = \arg\min_{\mu\geq 0}\{(\mathbf{y}-\mathbf{A}\boldsymbol{\mu})^T\boldsymbol{\Sigma}^{-1}(\mathbf{y}-\mathbf{A}\boldsymbol{\mu})+\beta\sum_j\sum_{m\in AW_j} b_{jm}^{ND\_predict}(\mu_j-\mu_m)^2\} \tag{3.9}$$

Minimization of this cost function can be achieved with many algorithms, and in this study, the Gauss-Seidel (GS) updating strategy was exploited due to its rapid convergence (Wang et al. 2006). It updates each pixel sequentially, and the values for all pixels are updated in each iteration. The use of the GS strategy for the minimization solution of Eq. (3.9) is given in the Appendix. The flowchart of deriving the MRF weighting coefficients and PWLS minimization for image reconstruction is shown by Figure 3.3.

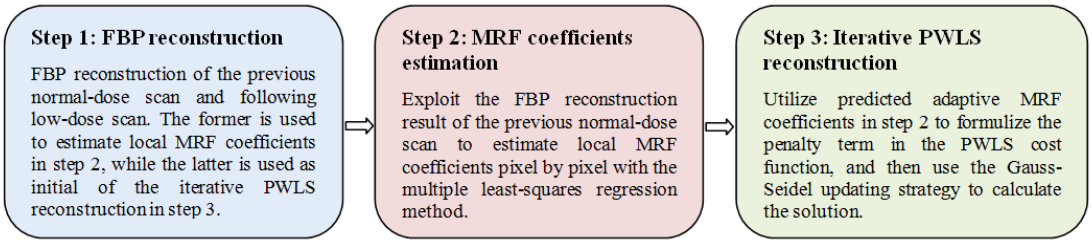

Figure 3.3. Flow chart of the proposed PWLS iterative reconstruction with adaptive MRF regularization for low-dose CT.

The pseudo-code for the cost function minimization in Eq.(3.9) is listed as follows (where $\mathbf{A}_j$ denotes the *j*th column of the projection matrix $\mathbf{A}$):

Initialization:

$$\hat{\boldsymbol{\mu}} = FBP\{\mathbf{y}\};\ \mathbf{q} = \mathbf{A}\hat{\boldsymbol{\mu}};\ \hat{\mathbf{r}} = \mathbf{y}-\mathbf{q};\ \boldsymbol{\Sigma} = diag\{\sigma_{y_i}^2\};$$

$$\lambda_j = \mathbf{A}_j^T\boldsymbol{\Sigma}^{-1}\mathbf{A}_j, \forall j$$

For each iteration:
begin
For each pixel j:
begin

$$\hat{\mu}_j^{old} := \hat{\mu}_j;$$

$$\hat{\mu}_j^{new} := \frac{\mathbf{A}_j^T \boldsymbol{\Sigma}^{-1} \hat{\mathbf{r}} + \lambda_j \hat{\mu}_j^{old} + \beta \sum_{m \in AW_j} b_{jm}^{ND\_predict} \mu_m}{\lambda_j + \beta \sum_{m \in AW_j} b_{jm}^{ND\_predict}};$$

$$\hat{\mu}_j := \max\{0, \hat{\mu}_j^{new}\};$$

$$\hat{\mathbf{r}} := \hat{\mathbf{r}} + \mathbf{A}_j(\hat{\mu}_j^{old} - \hat{\mu}_j);$$

end
end

In our implementations, we stop the reconstruction process after a number of iterations when the estimated images between two successive iterations become very small (e.g., RMSE < 0. 0002). This kind of stopping rule has been widely used in the iterative image reconstruction community. For the datasets presented in this study, 20 iterations were seen to be large enough for good convergence. And it may take around 30 minutes to reconstruct a 512×512 image on a desktop computer without any acceleration.

3.5 Experiments and results

In this study, experimental physical phantom and patient data were utilized to validate the presented PWLS iterative reconstruction scheme using the proposed adaptive MRF regularization (referred to as PWLS-adaptive), with comparison to the PWLS iterative reconstruction using the conventional GMRF regularization (referred to as PWLS-GMRF), the PWLS iterative reconstruction using the edge-preserving Huber regularization (referred to as PWLS-Huber), and the classical FBP algorithm.

3.5.1 Anthropomorphic torso phantom study

1). Data acquisition

An anthropomorphic torso phantom (Radiology Support Devices, Inc., Long Beach, CA) was used for experimental data acquisition. The phantom was scanned by a Siemens SOMATOM Sensation16 CT scanner (Siemens Healthcare, Forchheim, Germany) in a cine mode at a fixed bed position. The X-ray tube voltage was set to be 120 kV while the mAs level was set to be 40 mAs. Each scan included 1160 projection views evenly spanned on a 360^0 circular orbit, and each view included 672 detector bins. The distance from the X-ray source to the detector arrays was 1040 mm and the distance from the X-ray source to the rotation center was 570 mm. The CT scanner was rotated 150 times around the phantom.

The central slice sinogram data (672 bins×1160 views) of one scan was extracted for this feasibility study, which is regarded as low-dose scan. The averaged sinogram data from those 150 repeated scans of that slice was reconstructed by the FBP method to serve as the ground truth image for evaluation purpose and also as the previous normal-dose

scan for MRF coefficients prediction. The size of reconstructed image is 512×512 with pixel size of 1.0 ×1.0 mm^2.

2). Visualization-based evaluation

The reconstructed images by FBP, the PWLS-GMRF with $\beta = 3\times10^5$, the PWLS-Huber with $\beta = 3\times10^5$, and the PWLS-adaptive with $\beta = 3\times10^5$ from the noisy 40 mAs sinogram are shown in Figure 3.4. It can be observed that all the SIR algorithms outperformed the FBP in terms of noise and streak artifact suppression. As for the SIR algorithms, the PWLS-adaptive is superior to the PWLS-GMRF and the PWLS-Huber in terms of edge/detail preservation, which will be quantified in the following section.

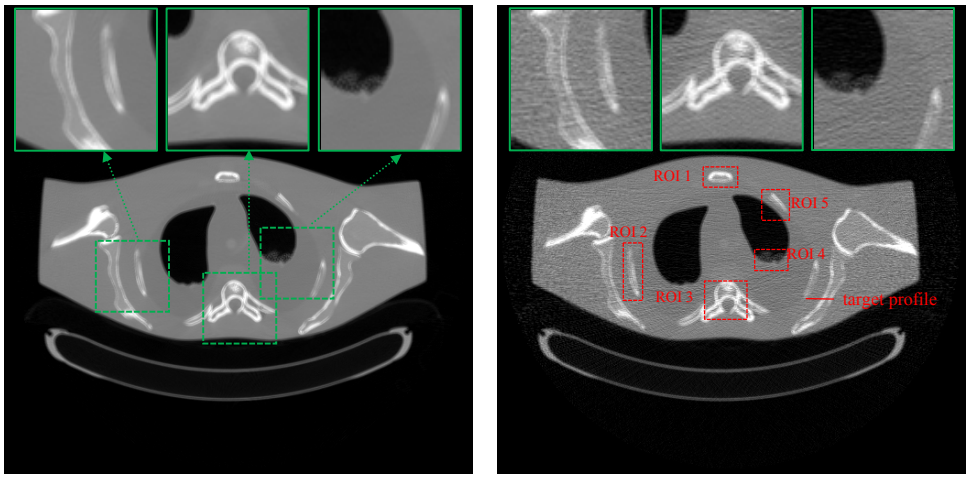

(a) (b)

(c) (d)

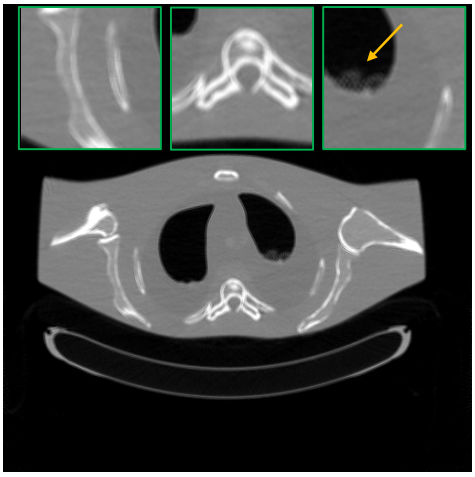

(e)

Figure 3.4. A reconstructed slice of the anthropomorphic torso phantom: (a) The FBP reconstruction from the averaged sinogram; (b) The FBP reconstruction from 40 mAs sinogram; (c) The PWLS-GMRF reconstruction from 40 mAs sinogram, $\beta = 3\times10^5$; (d) The PWLS-Huber reconstruction from 40 mAs sinogram, $\beta = 3\times10^5$, δ=0.004; (e) The PWLS-adaptive reconstruction from 40 mAs sinogram, $\beta = 3\times10^5$. All the images are displayed with the same window.

3). Quantitative evaluation

To quantitatively demonstrate the benefits of our proposed scheme, we compared the performance of the four algorithms on the reconstruction of ROIs with detailed structures, which were labeled with red rectangles in Figure 3.4(b). Four metrics were employed to quantitatively evaluate the image quality of the detailed ROIs. They are root mean squared error (RMSE), universal quality index (UQI), correlation coefficient (CC) and signal-to-noise ratio (SNR).

Let $\boldsymbol{\mu}_\mathbf{r}$ denote the vector of the reconstructed image and $\boldsymbol{\mu}_\mathbf{0}$ be the vector of the ground truth image or reference image, the metrics are defined as (Q is the number of image pixels):

$$RMSE = \sqrt{\frac{(\boldsymbol{\mu}_\mathbf{r}-\boldsymbol{\mu}_\mathbf{0})^T(\boldsymbol{\mu}_\mathbf{r}-\boldsymbol{\mu}_\mathbf{0})}{Q}} = \sqrt{\frac{1}{Q}\sum_{n=1}^{Q}(\mu_{r,n}-\mu_{0,n})^2} \tag{3.10}$$

$$UQI = \frac{4Cov\{\boldsymbol{\mu}_\mathbf{r},\boldsymbol{\mu}_\mathbf{0}\}}{\mathrm{var}\{\boldsymbol{\mu}_\mathbf{r}\}+\mathrm{var}\{\boldsymbol{\mu}_\mathbf{0}\}}\bullet\frac{\bar{\mu}_r\bar{\mu}_0}{\bar{\mu}_r^{\,2}+\bar{\mu}_0^{\,2}} \tag{3.11}$$

where

$$\bar{\mu}_r = \frac{1}{Q}\sum_{n=1}^{Q}\mu_{r,n},\ \bar{\mu}_0 = \frac{1}{Q}\sum_{n=1}^{Q}\mu_{0,n},\ \ \mathrm{var}\{\boldsymbol{\mu}_\mathbf{r}\} = \frac{1}{Q-1}\sum_{n=1}^{Q}(\mu_{r,n}-\bar{\mu}_r)^2,\ \ \mathrm{var}\{\boldsymbol{\mu}_\mathbf{0}\} = \frac{1}{Q-1}\sum_{n=1}^{Q}(\mu_{0,n}-\bar{\mu}_0)^2,$$

$$cov\{\boldsymbol{\mu}_\mathbf{r},\boldsymbol{\mu}_\mathbf{0}\} = \frac{1}{Q-1}\sum_{n=1}^{Q}(\mu_{r,n}-\bar{\mu}_r)(\mu_{0,n}-\bar{\mu}_0)$$

$$CC = \frac{\sum_{n=1}^{Q}(\mu_{r,n} - \bar{\mu}_r)(\mu_{0,n} - \bar{\mu}_0)}{\sqrt{\sum_{n=1}^{Q}(\mu_{r,n} - \bar{\mu}_r)^2 \sum_{n=1}^{Q}(\mu_{0,n} - \bar{\mu}_0)^2}} \tag{3.12}$$

$$SNR = 10\log_{10}\left(\frac{\sum_{n=1}^{Q}(\mu_{r,n} - \bar{\mu}_r)^2}{\sum_{n=1}^{Q}(\mu_{r,n} - \mu_{0,n})^2}\right) \tag{3.13}$$

The corresponding quantitative results are shown in Figure 3.5. As we can see, the proposed PWLS-adaptive algorithm offered the lowest RMSE and the highest UQI/CC/SNR for all the five detailed ROIs.

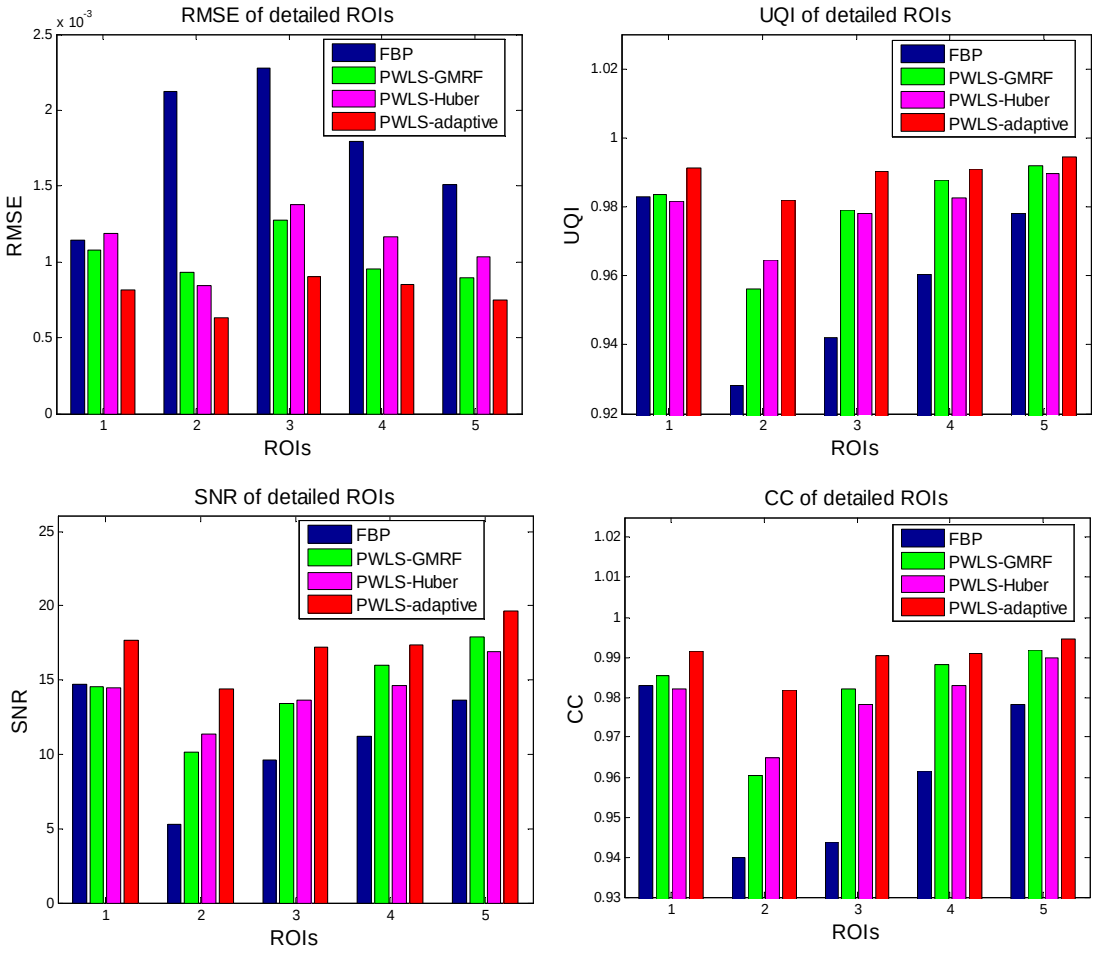

Figure 3.5. Performance comparison of four algorithms on the reconstruction of detailed ROIs labeled in Figure 3.4(b) with four different metrics. The corresponding algorithms are illustrated in figure legend.

4). Profile-based evaluation

To further visualize the difference among the four reconstruction algorithms, a horizontal profile of the resulting images were drawn across the red line labeled in Figure 3.4(b). The profile comparison further demonstrated the advantage of three SIR

algorithms over the FBP on noise suppression, as well as the advantage of the PWLS-adaptive over the PWLS-GMRF and the PWLS-Huber on edge/contrast preservation at matched noise level.

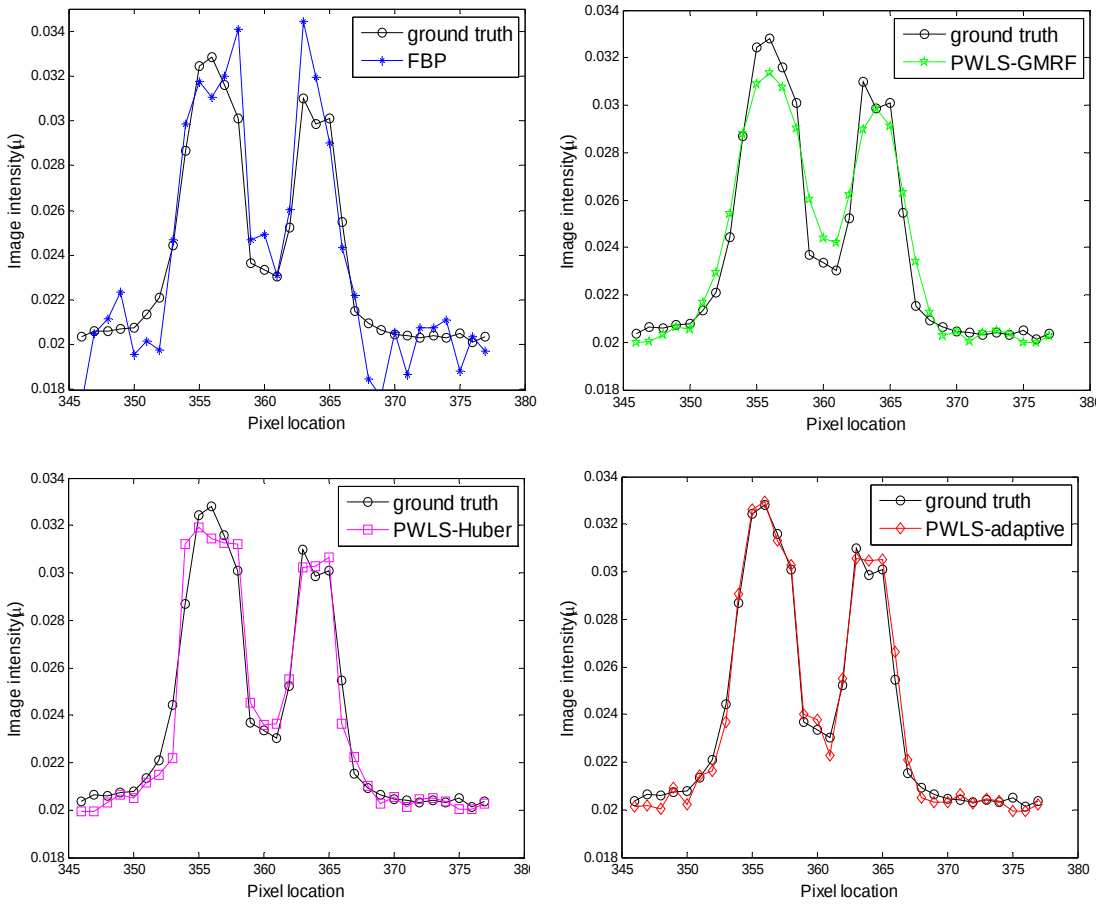

Figure 3.6. Comparison of the profiles along the horizontal line labeled in Fig. 4(b) between the four algorithms with 40 mAs sinogram and ground truth image. The corresponding algorithms are illustrated in figure legend.

3.5.2 Patient data study

1). Data acquisition

To evaluate the algorithms in a more realistic situation, the raw sinogram data was acquired using the same Siemens scanner from a patient who was scheduled for CT scan for medical reasons under the approval of the Institutional Review Board of the Stony Brook University. The scanning geometry is the same as that for the anthropomorphic torso phantom. The tube voltage was set to be 120 kV, and the mAs level was 100 mAs. We regarded this acquisition as the normal-dose scan, and instead of scanning the patient twice, we simulated the corresponding low-dose sinogram data by adding noise to the normal-dose sinogram data using the simulation method in (La Rivière and Billmire 2005). The noisy measurement N_i at detector bin i was generated according to the statistical model:

$$N_i \sim \text{Poisson}(N_{0i}\exp(-\overline{y}_i)) + \text{Gaussian}(0, \sigma_e^2) \tag{3.14}$$

where N_{0i} was set to be 5×10^4 and σ_e^2 was set to be 10 for low-dose scan simulation in this study. Then the corresponding noisy line integral y_i was calculated by the logarithm transform.

2). Visualization-based evaluation

The reconstructed images from the normal-dose sinogram data with the FBP algorithm serve as the *ground truth* image for this patient data study. The optimal β value for the PWLS-GMRF algorithm with the simulated low-dose patient sinogram data is 2×10^5. Again, the identical β value was adopted for the PWLS-Huber and the PWLS-adaptive so that the noise level in the uniform background region is equivalent for all the three PWLS algorithms.

One slice of the reconstructed images are shown in Figure 3.7, where (a) and (b) are the FBP reconstructed images from the acquired normal-dose and simulated low-dose sinogram data respectively, and (c) (d) (e) are the reconstructed images from the simulated low-dose sinogram by the PWLS-GMRF, the PWLS-Huber and the PWLS-adaptive algorithms with $\beta=2\times10^5$. It is evident that all the three SIR algorithms outperformed the FBP in terms of noise suppression, and the PWLS-adaptive algorithm was superior to the PWLS-GMRF and the PWLS-Huber in terms of edge and detail preservation.

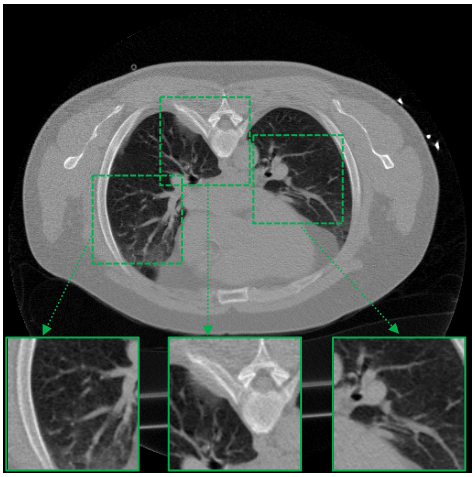

(a)

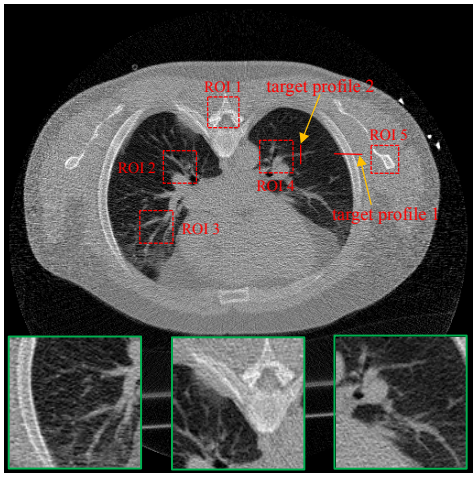

(b)

(c)

(d)

(e)

Figure 3.7. Reconstructed transverse slice of the patient data: (a) The FBP reconstruction from the normal-dose sinogram; (b) The FBP reconstruction from the simulated low-dose sinogram; (c) The PWLS-GMRF reconstruction from the simulated low-dose sinogram, $\beta = 2\times10^5$; (d) The PWLS-Huber reconstruction from the simulated low-dose sinogram, $\beta = 2\times10^5$, δ=0.004; (e) The PWLS-adaptive reconstruction from the simulated low-dose sinogram, $\beta = 2\times10^5$. All the images are displayed with the same window.

3). Quantitative evaluation

To quantitatively demonstrate the benefits of our proposed scheme, we compare the performance of the four algorithms on the reconstruction of ROIs with detailed structures, which were labeled with red rectangles in Figure 3.7(b). The corresponding quantitative results based on the four different metrics were shown in Figure 3.8. Again, the PWLS-adaptive algorithm yielded the lowest RMSE and the highest UQI/CC/SNR for all the five detailed ROIs.

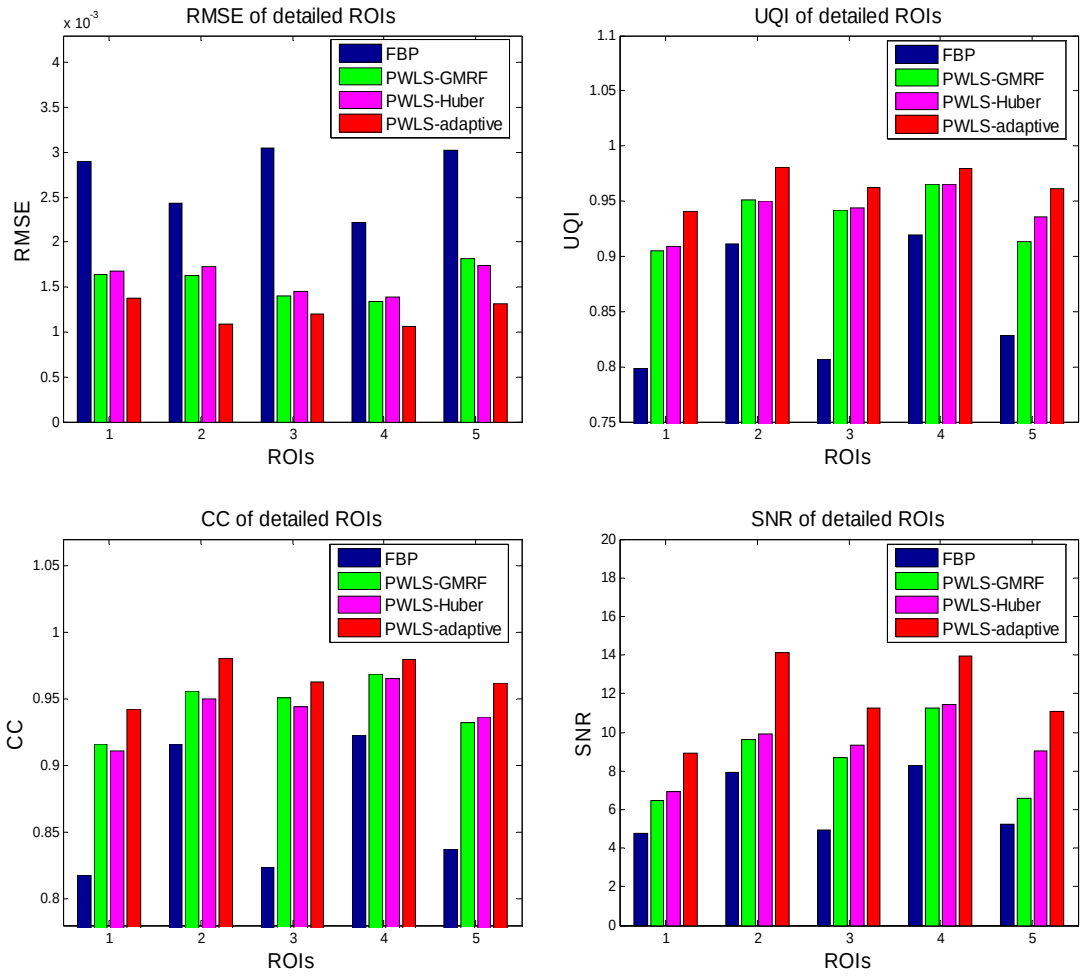

Figure 3.8. Performance comparison of four algorithms on the reconstruction of detailed ROIs labeled in Figure 3.7(b) with four different metrics. The corresponding algorithms are illustrated in figure legend.

4). Profile-based evaluation

Figure 3.9 shows the targeted horizontal profiles (labeled with red line in Figure 3.7 (b)) of the reconstructed images by the four reconstruction algorithms in Figure 3.7 as compared to that of the FBP reconstruction with normal-dose sinogram. The profile comparison quantitatively demonstrated the advantage of the three SIR algorithms over the FBP on noise suppression, as well as the advantage of the PWLS-adaptive over the PWLS-GMRF and the PWLS-Huber on edge and contrast preservation at matched noise level.

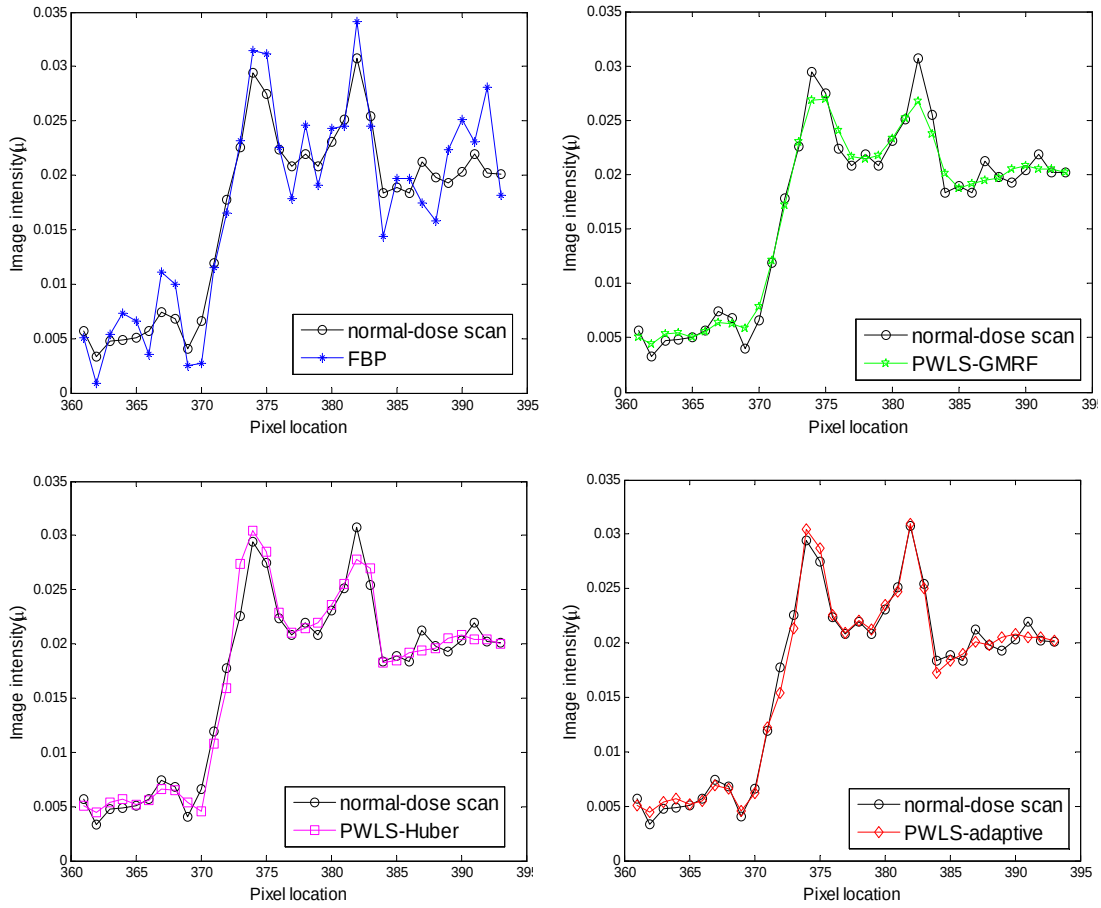

Figure 3.9. Comparison of the profiles along the horizontal line labeled in Figure 3.7(b) between the four algorithms with simulated low-dose sinogram and the FBP reconstruction with the normal-dose sinogram. The corresponding algorithms are illustrated in figure legend.

5). Profile-based evaluation

Figure 3.10 shows the vertical profiles (labeled with red line in Figure 3.7(b)) through a small object for the three SIR algorithms with comparison to the FBP reconstruction from the normal-dose sinogram. The contrasts shown in the figure legend were computed as:

$$Contrast = \frac{\mu_{\max} - \mu_{base}}{\mu_{base}} \tag{3.15}$$

where $\mu_{\max}$ is the maximum value of a profile through the object, while μ_{base} is the mean value of the profile baseline.

The reconstructed small object by the PWLS-adaptive algorithm has higher contrast (2.07) than that of the PWLS-GMRF algorithm (1.45) and the PWLS-Huber algorithm (1.83), and is closer to that of the FBP reconstruction from the normal-dose sinogram (2.37).

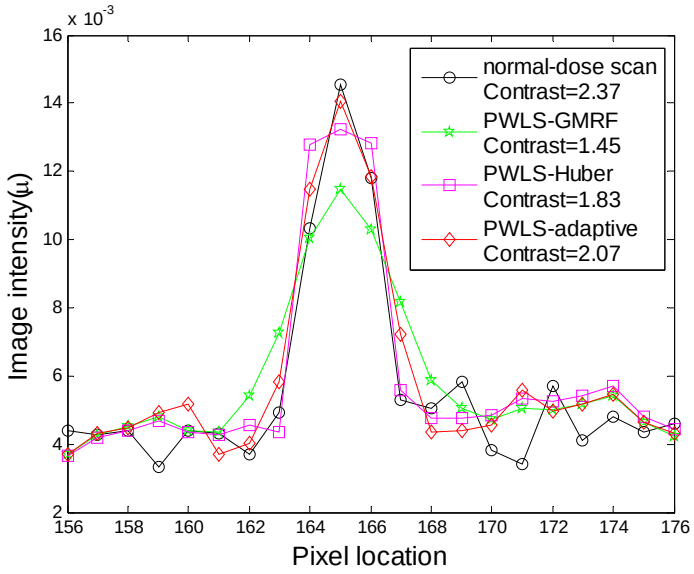

Figure 3.10. Comparison of the profiles along the vertical line labeled in Figure 3.7(b) between the three SIR algorithms with simulated low-dose sinogram and the FBP reconstruction with the normal-dose sinogram. The contrast of the small object and the corresponding algorithms are illustrated in figure legend.

3.6 Discussion and conclusion

The regularization term which reflects *prior* information, is very important for the SIR algorithms. Strategies using the image reconstructed from previous scan to improve the current scan reconstruction have been explored in several studies. Different from these works, we proposed to utilize the frequency information in the FBP reconstructed image from the previous normal-dose scan to improve the follow-up low-dose scans by incorporating a quadratic-form MRF regularization with adaptive MRF window and adaptive coefficients predicted from the previous normal-dose scan into the established PWLS iterative reconstruction scheme (PWLS-adaptive). The experimental results with both physical phantom and patient data demonstrated the feasibility and efficacy of the proposed scheme. We further compared the reconstruction results using the PWLS-adaptive to that using the conventional Gaussian MRF penalty (PWLS-GMRF) and the edge-preserving Huber penalty (PWLS-Huber). The results consistently showed that the presented PWLS-adaptive algorithm is superior on edge, detail and contrast preservation at matched noise level. In turn, this study showed us again how critical the penalty term is for the SIR algorithms.

It may seem counterintuitive to employ a small MRF window for uniform regions and a large MRF window for non-uniform regions in this study. Therefore, we emphasize again that this kind of MRF window size selection is operated in the frequency domain. The rationale behind this approach is that the more uniform the local structure is, the smaller the frequency spectrum spread is, so a smaller MRF window should be adopted, and *vice versa*. Traditional penalties generally utilize a small fixed MRF window size (e.g., 3×3 in the 2D case), which limit the spectral description to a crude low-pass model. By increasing MRF window size, the penalty term raises the number of degrees of freedom in spectral description, and can include the high frequency information (Wang et

al. 2012). In this way, the high frequency components, such as the edges and details, could be better preserved. In our another work (Zhang et al. 2013) which also utilizes the object scale map, we employed a large MRF window for uniform regions while a small MRF window for edge regions, but the weighting coefficients were adopted inversely proportional to the Euclidean distance between the central and neighboring pixels. The consideration was based on the reasons that the neighbors cupping is strong for uniform regions and a large MRF window should be employed while the neighbors cupping is weak for edge regions thus a small MRF window may be more reasonable. Generally, these are two different ways of utilizing the object scale map, one in the frequency domain as in this study while the other in the spatial domain as in (Zhang et al. 2013).

In this proof-of-concept study, the image misalignment issue between the low-dose scan and the corresponding normal-dose scan was not considered explicitly. In some applications where the normal-dose scan and low-dose scan is perfectly aligned, the proposed PWLS-adaptive algorithm can be used directly. For example, in the image-guided needle biopsy for lung nodule analysis, the motion among different scans can be ignored when CT is used in a cine mode and the patient holds the breath during each single scan. In the applications where misalignment between the low-dose and normal-dose scans cannot be ignored, registration can be first employed to align the scans. We plan to investigate the influence of image registration accuracy on our proposed method in a future study.

Chapter 4 . Deriving region-specific MRF coefficients from previous full-dose CT scan for low-dose CT reconstruction

In our previous study of utilizing full-dose (or normal-dose) CT scan via MRF coefficients in chapter 3, we predicted MRF coefficients for each single voxel in the full-dose image. That is, for a 2D image with 512×512 pixels, 512×512 sets of MRF coefficients were obtained. And because of the pixel-by-pixel mechanism, accurate registration between the previous full-dose image and the current low-dose image is required before we can reconstruct the low-dose image. In practice, severe patient motion, tissue or organ deformation, fluid flow, etc. can occur between the full- and low-dose scans, where even a deformable registration may not be adequate to capture the complex anatomical and physiological motions, resulting in residual errors in the low-dose image reconstruction (Dang et al. 2014). To mitigate this issue, in this chapter, we proposed to segment each image into several tissue regions (e.g., lung, bone, fat, and muscle). And then, for a 2D image with 512×512 pixels, only 4 sets of MRF coefficients are predicted from the previous full-dose image, assuming that the pixels within the same tissue region share similar texture pattern. Because of its region-by-region nature, the strategy in this chapter is more efficient and more feasible in practice than that in chapter 3. We validate the efficacy and feasibility of the proposed strategy via experiments with simulated and real patient datasets.

4.1 Introduction

Recently, noticeable research efforts have been devoted to take advantage of previously-available full-dose CT (FdCT) scan, for the purpose of improving the piece-wise smooth image reconstruction of low-dose CT (LdCT) images. For instance, Nett et al. (Nett et al. 2009) incorporated a registered FdCT image into their prior image constrained compressed sensing (PICCS) cost function (Chen et al. 2008) for iterative reconstruction of subsequent LdCT images. Stayman et al. (Stayman et al. 2013; Dang et al. 2014) presented a PICCS-type penalty term, but the high-quality prior image was formulated into a joint estimation framework for both image registration and image reconstruction in order to better capturing the anatomical motion among different scans. Moreover, Ma et al. (Ma et al. 2011; Ma et al. 2012) proposed previous FdCT image induced nonlocal means penalties to improve the following LdCT image reconstruction for perfusion and interventional imaging, wherein the previous FdCT image was also pre-registered with the LdCT scans. These efforts share the common idea of registering the FdCT image structure with the LdCT image to ensure piece-wise regional smoothness and edge-sharpness image reconstructions. The edge-preserving regional smoothing paradigm can sharpen the tissue region borders, but may sacrifice the tissue region image texture characteristics, which have been shown as a useful imaging marker for many clinical tasks (Aerts et al. 2014).

This exploratory study aims to shift the paradigm to texture-preserving LdCT reconstruction by capturing the regional tissue textures from the previous FdCT scan and incorporating the textures as *a priori* knowledge for Bayesian reconstruction of the current LdCT images. Specifically, it captures the image textures of muscle, fat, bone, lung, etc., from the full-dose image and then incorporates the tissue image textures as *a priori* knowledge for Bayesian reconstruction of the corresponding tissue regions in the low-dose images, so that the reconstruction preserves not only the edges but also the textures inside the tissue regions.

4.2 The proposed texture-preserving MRF regularization

Different from the regional noise smoothing penalty such as GMRF and Huber penalty, we proposed a novel tissue region-based texture-preserving regularization which can be given as:

$$U(\boldsymbol{\mu}) = \sum_{r=1}^{R} \sum_{j \in \text{Region}(r)} \sum_{m \in \Omega_j} b_{jm}^{\text{FD\_predict}} (\mu_j - \mu_m)^2 , \tag{4.1}$$

where R is the number of different tissue regions and typically set to be 4 for chest CT imaging, representing lung, bone, fat and muscle, respectively. The index r runs over all the tissue regions, and index j runs over all the voxels in a specific tissue region. Ω denotes the MRF window for the neighborhood system. $\{b_{jm}^{\text{FD\_predict}}\}_{m \in \Omega_j} = \mathbf{b}_r^{\text{FD\_predict}}$ represents a set of MRF model coefficients of tissue region r (each tissue region has a specific set of MRF coefficients, and the voxels in the same tissue region employ the same set of MRF coefficients) predicted from the previous FdCT scan, where FD is the abbreviation for full-dose. This definition of MRF model coefficients is the central idea of this study and will be investigated in the following sections. The description on the MRF neighborhood system employs a pair-wise quadratic form for simplicity in computing the PWLS solution. For the task of extracting tissue textures, an adequate window size is desired and will be determined by experiments. The definition of Eq. (4.1) is based on the well-established MRF theory and thus our attention will then turn to its implementation in the following sections.

Given a FdCT image and an adequate MRF window size, a set of MRF model coefficients corresponding to a tissue region can be determined by a linear regression strategy such that every image voxel inside the MRF window can be predicted from a linear combination of its clique-mates. Among all the linear regression estimation algorithms, the least-squares algorithm is adapted in this study because of its computational efficiency. According to the MRF definition that the clique-mates of current voxel are the neighbors within the MRF window, thus the least squares predicted MRF coefficients for the clique-mates can be formulated as (Wang et al. 2012):

$$\mathbf{b}_r^{\text{FD\_predict}} = \arg\min_{\mathbf{b}_r} \sum_{k \in \text{Region}(r)} (\mu_k^{FD} - \mathbf{b}_r^T \boldsymbol{\mu}_{\Omega_k}^{FD})^2 = \left[\sum_{k \in \text{Region}(r)} (\boldsymbol{\mu}_{\Omega_k}^{FD} (\boldsymbol{\mu}_{\Omega_k}^{FD})^T) \right]^{-1} \left[\sum_{k \in \text{Region}(r)} (\boldsymbol{\mu}_{\Omega_k}^{FD} \mu_k^{FD}) \right] \tag{4.2}$$

where vector $\boldsymbol{\mu}^{FD}$ is the FdCT image. The expression $\sum_{k \in \text{Region}(r)} (\boldsymbol{\mu}_{\Omega_k}^{FD} (\boldsymbol{\mu}_{\Omega_k}^{FD})^T)$ is the sample auto-correlation matrix, and $\sum_{k \in \text{Region}(r)} (\boldsymbol{\mu}_{\Omega_k}^{FD} \mu_k^{FD})$ is the sample cross-correlation vector. It is

expected that the sum of the predicted MRF coefficients for each region, $\text{sum}(\mathbf{b}_r^{\text{FD\_predict}})$, shall be equal to 1.

4.3 Summary of the presented PWLS-texture method

With the WLS criterion and the texture-preserving MRF regularization presented above, our PWLS iterative reconstruction scheme for low-dose CT can be summarized as follows:

$$\boldsymbol{\mu}^* = \arg\min_{\mu \geq 0} \{(\mathbf{y} - \mathbf{A}\boldsymbol{\mu})^T \mathbf{D}(\mathbf{y} - \mathbf{A}\boldsymbol{\mu}) + \beta \sum_{r=1}^{R} \sum_{j \in \text{Region}(r)} \sum_{m \in \Omega_j} b_{jm}^{\text{FD\_predict}} (\mu_j - \mu_m)^2\} \tag{4.3}$$

A flowchart for implementation of the presented knowledge-based Bayesian reconstruction method can be summarized by the four steps in Figure 4.1, where steps 1 and 2 operate on both full- and low-dose scans, and steps 3 and 4 only on full- and low-dose scan, respectively. More details on the implementation are described below.

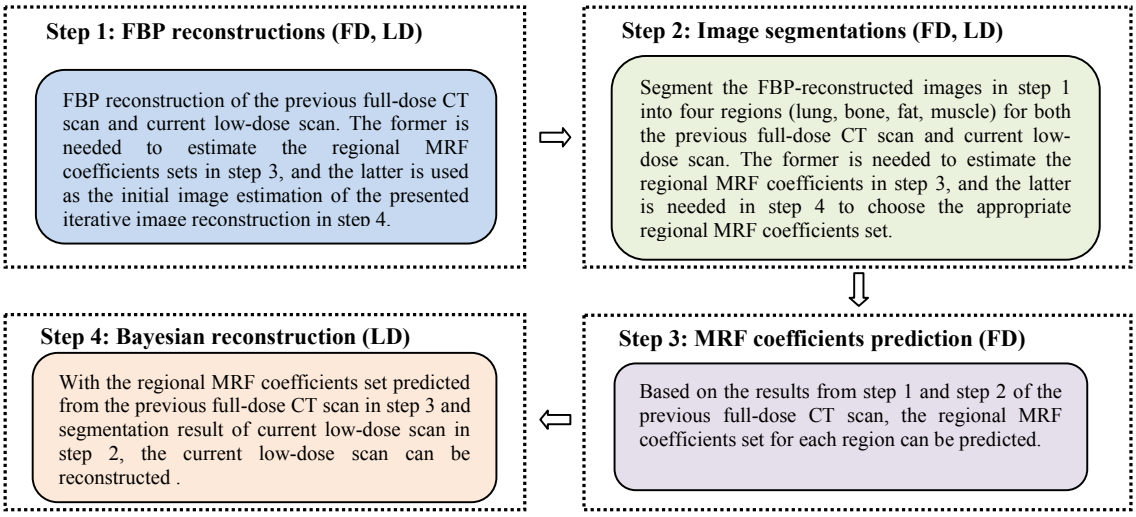

Figure 4.1. Flowchart of the proposed texture-preserving LdCT image reconstruction algorithm.

Many numerical methods could be chosen to calculate the resulting PWLS solution. This study employed the Gauss-Seidel updating strategy due to its rapid convergence. The algorithm for the minimization solution can be illustrated by the pseudo codes below. where $\mathbf{A}_j$ denotes the jth column of the projection matrix $\mathbf{A}$, σ_e^2 is the electronic noise and N_i^0 is the mean number of X-ray photons just before entering the patient body and going toward the detector cell i, where the values of σ_e^2 and N_i^0 were estimated given the data acquisition protocol.

Initialization:

$\hat{\boldsymbol{\mu}} = FBP\{\mathbf{y}\}$; $\mathbf{q} = \mathbf{A}\hat{\boldsymbol{\mu}}$; $\hat{\mathbf{r}} = \mathbf{y} - \mathbf{q}$;

$$\mathbf{D} = diag\left\{\frac{(N_i^o e^{-q_i})^2}{N_i^o e^{-q_i} + \sigma_e^2}\right\}$$

$\lambda_j = \mathbf{A}_j^T \mathbf{D} \mathbf{A}_j, \forall j$

For each iteration:
begin
For each voxel j:
determine tissue region for voxel j , $j \in \text{Region}\ (r)$;
choose corresponding MRF coefficient set;
begin

$$\hat{\mu}_j^{old} := \hat{\mu}_j;$$

$$\hat{\mu}_j^{new} := \frac{\mathbf{A}_j^T \mathbf{D} \hat{\mathbf{r}} + \lambda_j \hat{\mu}_j^{old} + \beta \sum_{m \in \Omega_j} b_{jm}^{FD\_predict} \mu_m}{\lambda_j + \beta \sum_{m \in \Omega_j} b_{jm}^{FD\_predict}};$$

$$\hat{\mu}_j := \max\{0, \hat{\mu}_j^{new}\};$$

$$\hat{\mathbf{r}} := \hat{\mathbf{r}} + \mathbf{A}_j (\hat{\mu}_j^{old} - \hat{\mu}_j);$$

end

$$\mathbf{D} := diag\left\{ \frac{(N_i^o e^{-\sum_j A_{ij} \hat{\mu}_j})^2}{N_i^o e^{-\sum_j A_{ij} \hat{\mu}_j} + \sigma_e^2} \right\}$$

$$\lambda_j := \mathbf{A}_j^T \mathbf{D} \mathbf{A}_j, \forall j$$

end.

We stopped the reconstruction process after a number of iterations when the estimated images between two successive iterations become very small (e.g., RMSE < 0. 0002). Typically, 20 iterations were seen to be large enough for good convergence. And it may take around 30 minutes to reconstruct a 512×512 image on a desktop computer without any acceleration.

4.4 Experiments and results

A patient, who was scheduled for CT-guided lung nodule needle biopsy at Stony Brook University Hospital, was recruited to this study under informed consent after approval by the Institutional Review Board. The patient was scanned using a Siemens CT scanner. The X-ray tube voltage was set to be 120 kV, and the tube current was set to be 100 mAs for the full-dose scan. The subsequent low-dose scans were performed at 20 mAs level. The raw data were calibrated by the CT system and outputted as sinogram data or line integrals. In addition to the patient recruitment for both full- and low-dose scans, two more recruitments were made for only full-dose scans on patients, one patient has a lung nodule and the other patient has a colon polyp, both of which have a size of 10 mm.

Based on the patient scans, we first performed experiments using simulated low-dose sinogram data by adding noise to the full-dose sinogram data with the simulation tool of (La Rivière and Billmire 2005). The reason of using simulated low-dose data is that the ground truth is available for a proof-of-concept study. Also, by a prefect registration between the full- and low-dose scans in the simulation, the region-specific MRF coefficients predicted from the neighboring slices of the full-dose image can be applied to

different slices in the corresponding low-dose image reconstruction and the impact on the mismatch of slice location and, therefore the mismatch of tissue regions, can be accurately documented.

Then experiments using the acquired full- and low-dose sinogram data at 100 and 20 mAs levels from the same patient were also performed. In the 20 mAs scan, all variations, including patient movements, organ deformations, gantry positioning between the full- and low-dose scans, etc., are present. In addition, the variation associated with the image segmentation is also involved. This clinical pilot study reflects the current clinical situation.

4.4.1 Experiments on simulated low-dose sinogram data

1). Extraction of MRF model coefficients

Given the 100 mAs full-dose data of the patient (who has also a low-dose scan at 20 mAs level) and its simulated low-dose sinogram data, the Step 1 of Figure 4.1 is to apply the well-established filtered back-projection (FBP) algorithm to reconstruct the full-dose data with Ramp filter at Nyquist frequency and the low-dose data with Hann filter at 50% Nyquist frequency. The reason of using Hann filter at 50% Nyquist frequency is because of the increased noise in the low-dose data. This smoothed FBP reconstruction of low-dose data will be treated as the initial estimate of the desired solution. The full-dose FBP reconstruction will be treated as *a priori* image, from which the tissue image textures will be extracted.

Given the above FBP reconstructions, the Step 2 of Figure 4.1 is to apply an efficient image segmentation algorithm to label the tissue regions. Because of its high computing efficiency, our previously-reported vector quantization (VQ) segmentation algorithm (Han et al. 2015) was adopted in this exploratory study. It is fully automatic once the number of tissue types is given, e.g., setting R=4 to represent lung, bone, fat, and muscle for chest CT imaging. Moreover, we adopted morphological operations to enlarge the segmented lung parenchyma and bone region boundaries slightly so that the final lung region for MRF coefficients prediction would include both the blood vessels inside lung and the juxta-pleural nodules attached to the pleural wall. The bone marrow with relatively lower intensities was also included in the refined bone region for MRF coefficients prediction of the bone tissue. Generally, it took less than 1 second to segment a 512×512 image on a desktop computer without acceleration. Because of the high computing efficiency, the VQ algorithm was applied to the low-dose initial estimate and each refining iteration result to obtain the tissue masks. Figure 4.2 illustrates an example of segmenting the full-dose image.

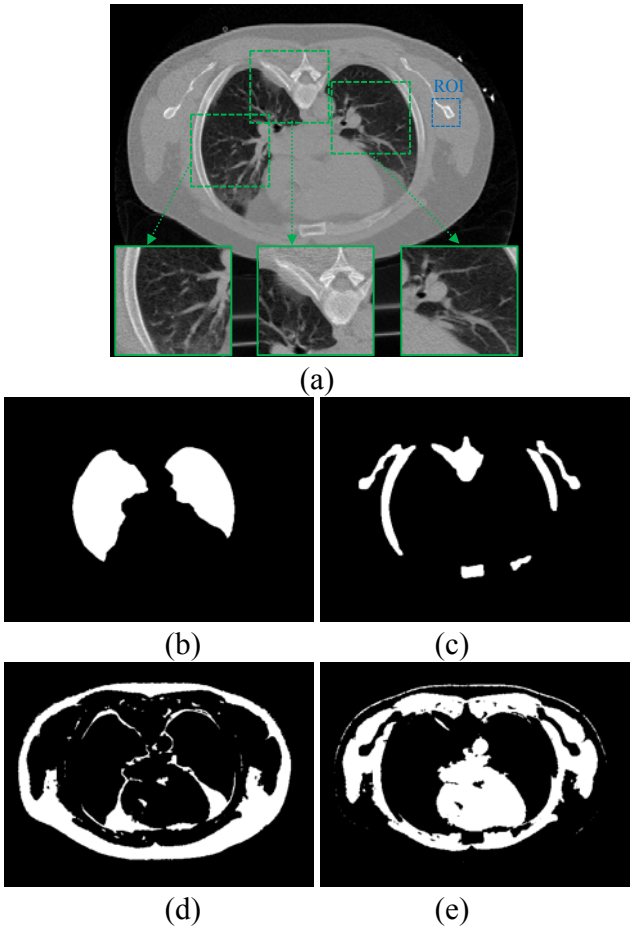

Figure 4.2. Segmented masks of the chest CT image (a). Picture (b) is the lung mask; (c) is the bone mask; (d) is the fat mask; and (e) is the muscle mask.

Given the segmented masks of the four tissue types from the FdCT FBP reconstruction of Figure 4.2, the Step 3 of Figure 4.1 is to extract the corresponding MRF model coefficients set by Eq. (4.2). From experiments, we found that a 7×7 MRF window size is sufficient, since the MRF coefficients beyond this window are close to zero and have nearly no impact. Figure 4.3 illustrates the predicted MRF coefficients set of the four tissue regions, respectively. It is interesting to see that the MRF model coefficients of the lung and bone regions have some similarity while the coefficients of the fat and muscle regions also have some similarity, but the coefficients of the group of lung/bone are clearly different from the coefficients of the group of fat/muscle. The former group has a large intensity variation while the later group has a small intensity variation. All the four tissue regions exhibit different spectral patterns corresponding to different image textures. It is worth noting that the sum of the predicted MRF coefficients for each region, $\text{sum}\,(\mathbf{b}_r^{\text{FD\_predict}})$, is close to 1, as expected.

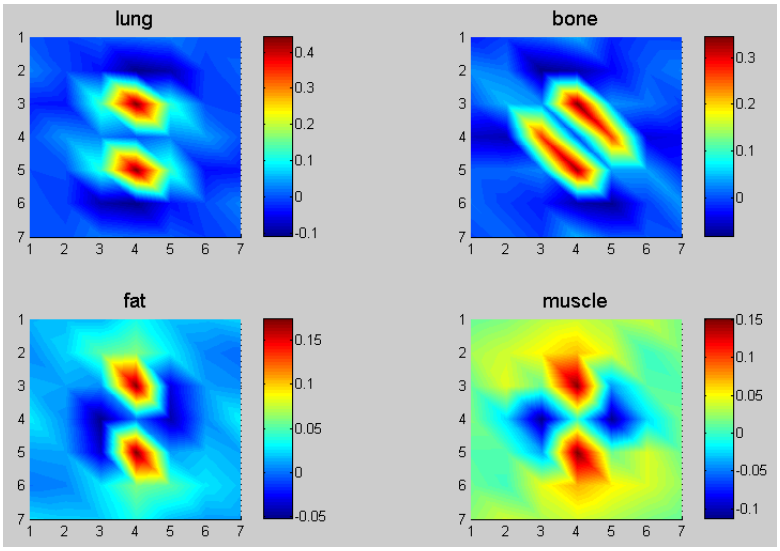

Figure 4.3. The predicted four sets of MRF model coefficients for the four tissue regions of Figure 4.2 with a 7×7 MRF window size in 2D presentation. The corresponding regions are indicated by picture title.

Since our ultimate goal is to preserve these image textures of full-dose scan in the low-dose image reconstructions, the spatial mismatch between the full- and low-dose images must be considered. In the image slice (transverse) plane, the spatial mismatch is not a concern because the contents in each segmented region mask remain the same regardless where the region is located once the axial location is the same between the full- and low-dose images. Therefore, the concern would be on the mismatch of the axial location. To get insights on this, we took the slice of Figure 4.3 which is located at slice #60 as the reference to investigate its nearby slices. Figure 4.4 shows the predicted MRF model coefficients of the lung region from slice #58 to slice #62 of the same patient, as well as the coefficients predicted from the whole five neighboring slices. The similarity among the six sets of MRF coefficients can be quantified by the correlation coefficient measure with a value greater than 98% and with a very tiny difference (discrepancy <5%). The phenomenon of the predicted MRF model coefficients from the neighboring image slices for the lung region also holds for the other three regions (bone, fat, and muscle).

The regional spectral pattern similarity can be attributed to the tissue structure similarity among nearby image slices. Because of this similarity among nearby image slices and the region-specific nature of the estimated MRF model coefficients across the entire image slice, an accurate image alignment between the full-and low-dose in the axial direction is also not necessary. In other words, when we reconstruct one slice of the low-dose scan, we can potentially utilize the MRF model coefficients trained from the roughly-matched nearby image slices of the FdCT scan, which dramatically relieves the demand for accurate alignment of the full-dose image with the low-dose image along the axial direction and completely eliminates the need for voxel-by-voxel alignment across the transverse plane.

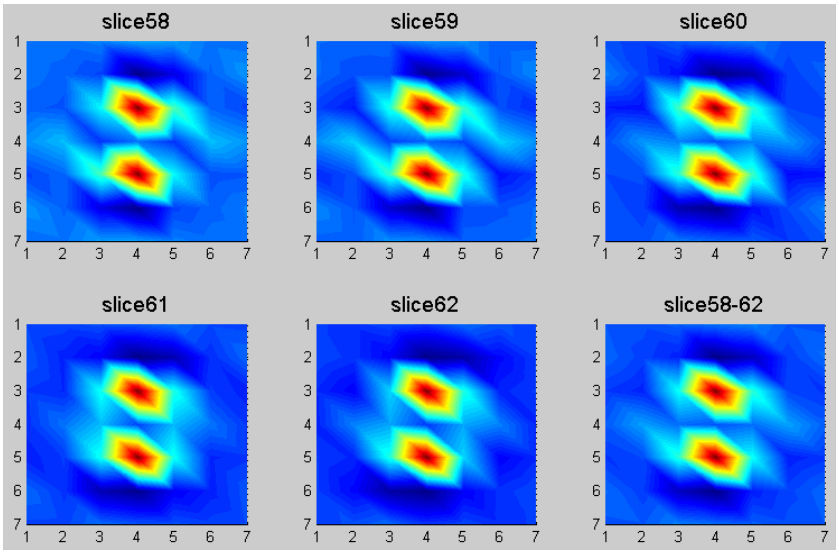

Figure 4.4. The predicted MRF coefficients of the lung region for five neighboring slices in 2D presentation. The corresponding slice numbers are indicated in picture title.

2). Image reconstruction

From the simulated low-dose data of the patient, the sinogram of one slice (slice #60) was extracted to illustrate the first scenario of our experiments, i.e., the slice match between full- and low-dose scans. In this study, we chose β value that gave the best eye-appealing result among other values for the three MRF algorithms. The reconstructed images from the simulated low-dose sinogram by the FBP, PWLS-GMRF, PWLS-Huber, and our proposed PWLS-texture algorithm are shown in Figure 4.5. It can be observed that all the MRF algorithms outperformed the FBP method in terms of noise suppression. While for the three MRF algorithms, the proposed PWLS-texture is superior to both the PWLS-GMRF and the PWLS-Huber in terms of edge/detail preservation, which will be quantified in the following sections. It should be noted that, for the PWLS-texture algorithm, the region-specific MRF coefficients were predicted from the same slice of the corresponding full-dose image (i.e., slice #60, as shown in Figure 4.2(a)). Therefore, we use the legend "MRF-T60" to denote the corresponding results.

According to the analysis of Figure 4.3 and Figure 4.4, since the predicted MRF coefficients from nearby slices show similar patterns, we may not necessarily need to utilize the MRF coefficients predicted from the exactly same slice of the corresponding FdCT scan. That is, when we reconstruct the slice #60 of the low-dose scan, we can potentially employ the MRF coefficients predicted from any one or summation of all the nearby slices (slice #58, #59, #60, #61, #62) of the full-dose scan. In this second scenario of our experiments, Figure 4.6 shows the reconstructed images from the simulated low-dose sinogram data by the proposed PWLS-texture algorithm using MRF coefficients predicted from different slices of the full-dose image. We can observe that the reconstructed images in Figure 4.6 are very similar to each other, and the quantitative evaluations in the following sections also validate this observation.

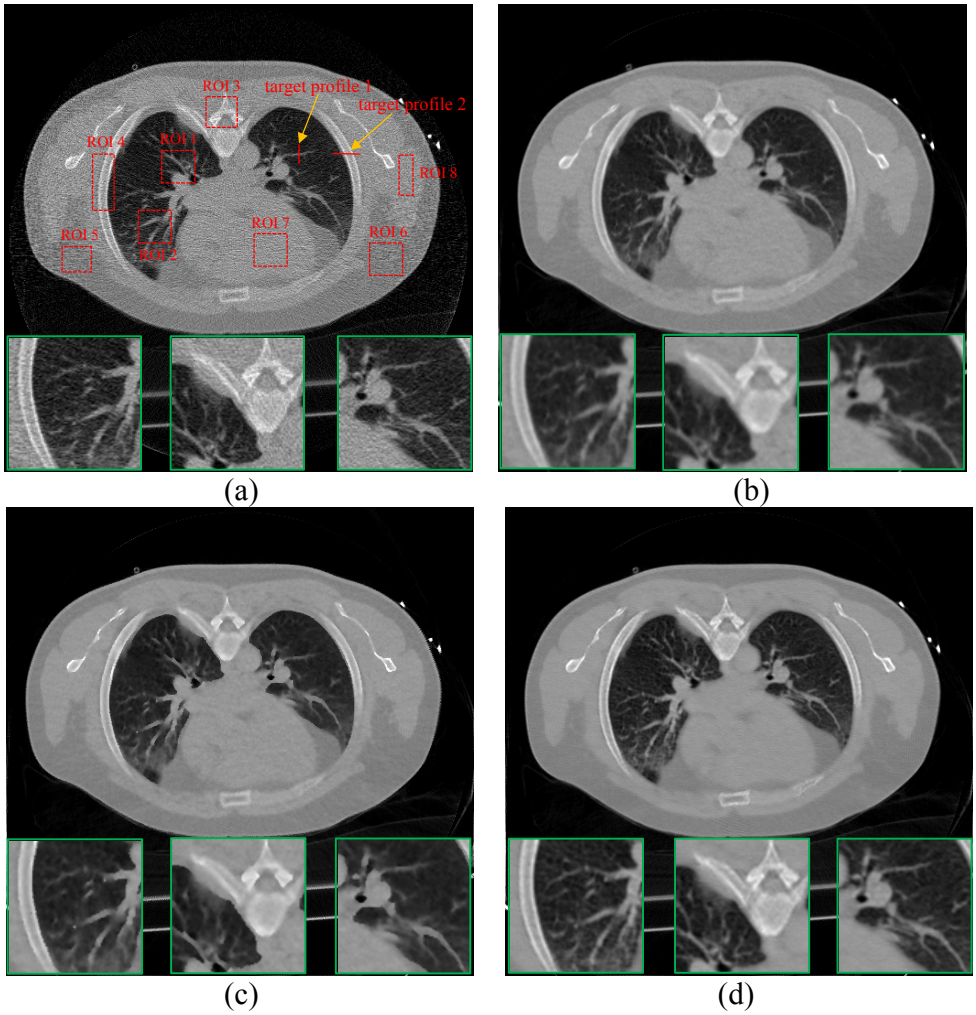

Figure 4.5. Reconstructed transverse slice of the patient from the simulated low-dose sinogram: (a) The FBP reconstruction; (b) The PWLS-GMRF reconstruction, $\beta = 3\times10^5$; (c) The PWLS-Huber reconstruction, $\beta = 3\times10^5$, $\delta=0.004$; and (d) The MRF-T60 reconstruction, $\beta = 3\times10^5$. All the images are displayed with the same window [0, 0.034] mm^{-1}.

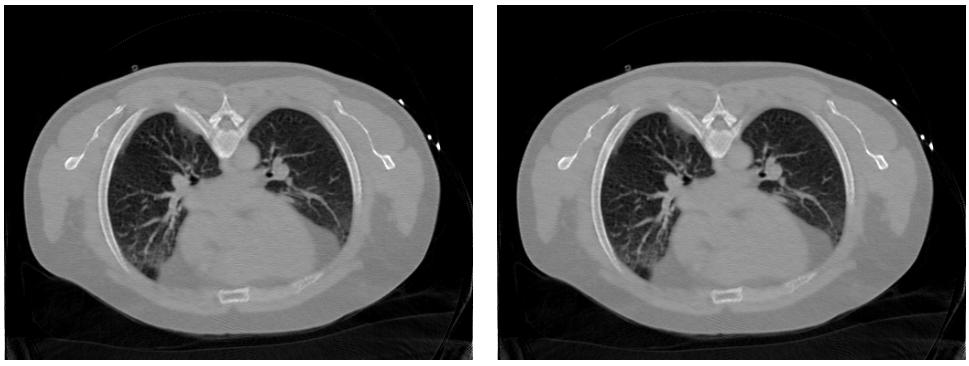

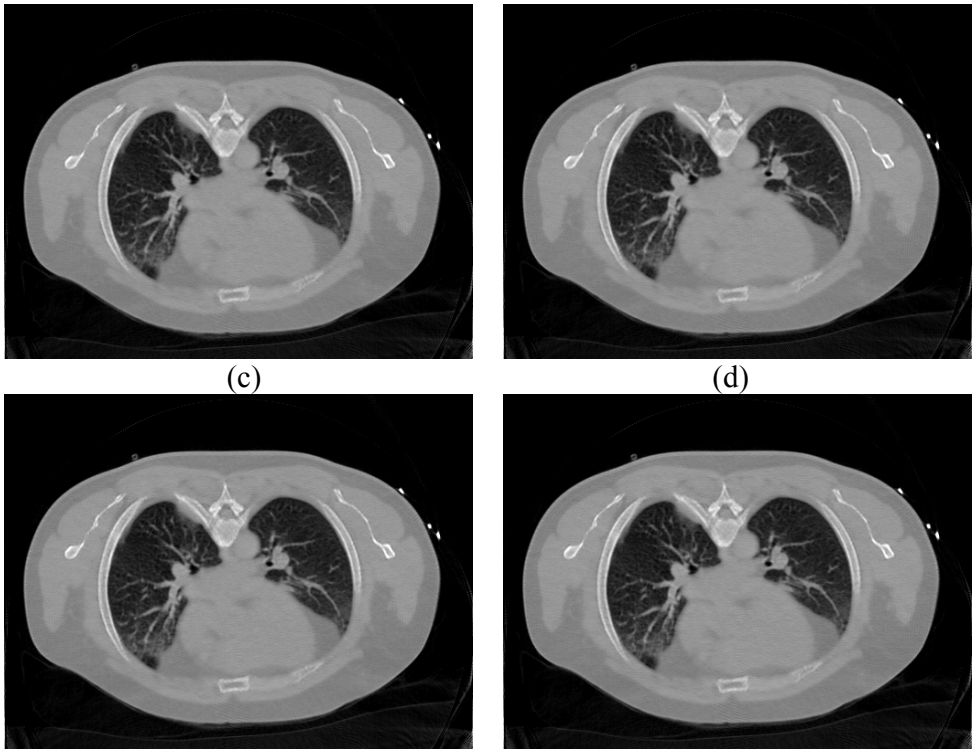

Figure 4.6. Reconstructed transverse slice of the patient by the proposed PWLS-texture algorithm from the simulated low-dose sinogram: (a) The MRF-T58 reconstruction; (b) The MRF-T59 reconstruction; (c) The MRF-T60 reconstruction; (d) The MRF-T61 reconstruction; (e) The MRF-T62 reconstruction; and (f) The MRF-T58-62 reconstruction. The images were cropped for better visualization. All the images are displayed with the same window [0, 0.034] mm^{-1}.

3). Normal vector flow measure

In order to quantify the texture benefit of the proposed *a priori* knowledge model, a region of interest (ROI), indicated by a rectangular box in Figure 4.2(a), was selected to plot the normal vector flow (NVF) (Liu et al. 2014) images for different reconstruction methods in Figure 4.5, and the corresponding NVF images are illustrated in Figure 4.7. The NVF image in Figure 4.7(a) is corresponding to the FBP reconstruction from the full-dose scan of Figure 4.2(a), and can serve as the reference standard. The gradual changes of the intensities in the desired image are often shown as ordered arrow in the NVF image, while the noise in the image is often shown as disordered arrows, as shown in Figure 4.7(b). From Figure 4.7(c)-(e), we can see that the disordered arrows in the uniform regions were suppressed by using MRF reconstruction methods. However, the ordered arrows around the bone boundaries in Figure 4.7(c) swelled a little bit due to the edge blurring in the PWLS-GMRF reconstructed image of Figure 4.5(b), and those in Figure 4.7(d) were falsely depicted due to the brute enforcing of edge-preserving characteristics of the Huber penalty of Figure 4.5(c). In contrast, the NVF image of the proposed PWLS-texture algorithm in Figure 4.7(e) demonstrated best matches of the

ordered arrows as compared to the reference standard of Figure 4.7(a), which indicates that the textures of the corresponding reconstruction were best preserved.

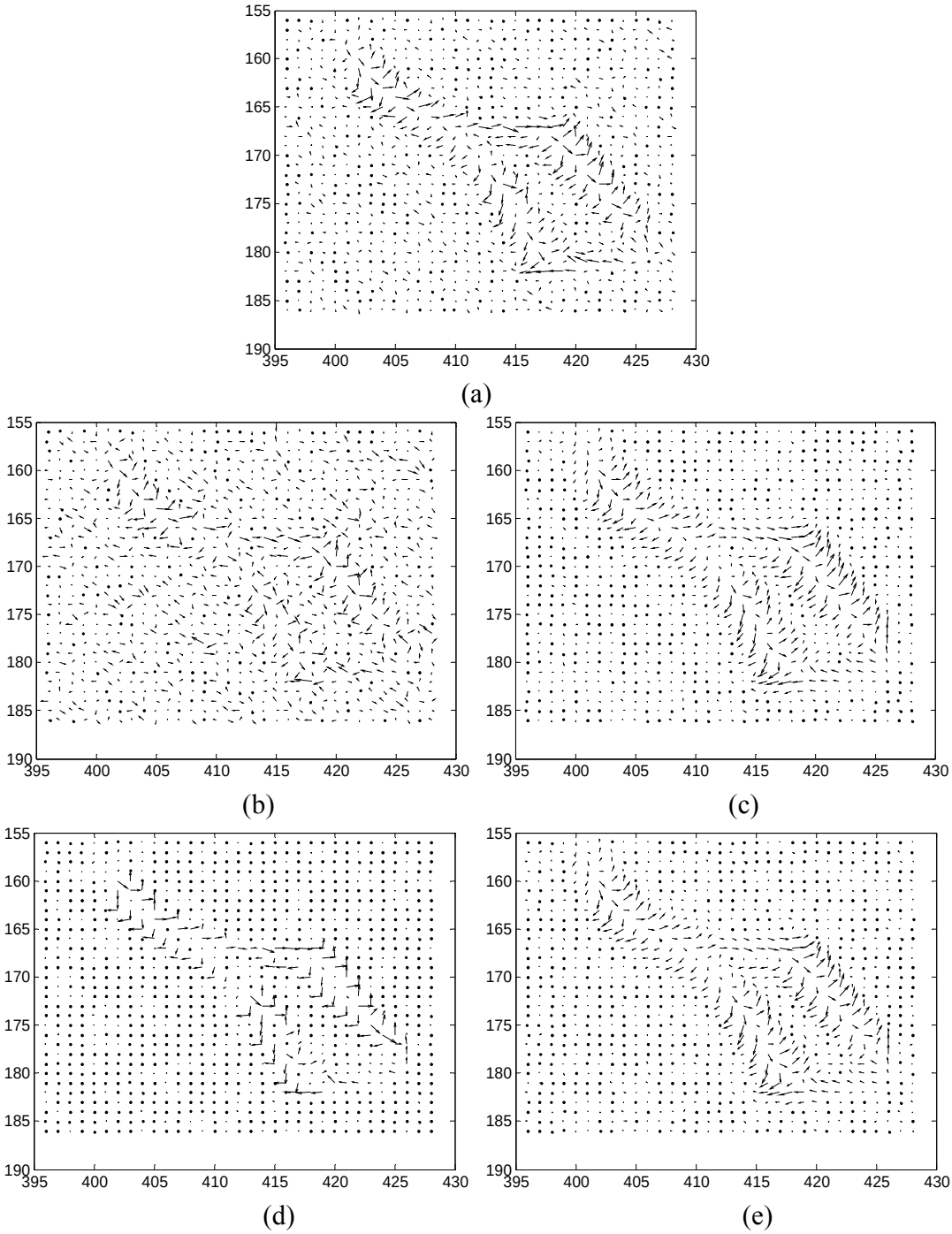

Figure 4.7. NVF images of a ROI labeled in Figure 4.2(a). (a) is the reference from Figure 4.2(a). (b)-(e) are corresponding to the reconstructions in Figure 4.5(a)-(d).

4). Haralick texture measures

Haralick texture features have been widely used for classification of lesion malignancy (Haralick et al. 1973) and, therefore, adopted to quantify the texture preservation in the reconstructions of the four methods above (the FBP, PWLS-GMRF, PWLS-Huber, and MRF-texture). Eight ROIs were selected on the lung, bone, fat, and muscle, respectively, from the full-dose image in Figure 4.5(a) to set up the baseline or reference. The corresponding ROIs were selected on the low-dose reconstructions of the four methods. The 14 Haralick texture measures were extracted from each ROI. The Euclidean distance between the textures of the full- and low-dose images was used as the quantitative measure. A shorter distance indicates better texture preservation by the reconstruction algorithm. Table 4.1 shows the quantitative results. The presented PWLS-texture image reconstruction has the best performance on texture preservation, as expected. Because of the known textures from lung, bone, fat, and muscle from the full-dose image, the gain by the proposed PWLS-texture algorithm on these four tissue types are noticeable in the low-dose image reconstruction.

Table 4.1. Texture distance between the reference full-dose image and the reconstructed low-dose images in Figure 4.5.

ROI	Tissue type	FBP	PWLS-GMRF	PWLS-Huber	PWLS-texture
1	lung	7.2076	2.3043	7.3989	**1.7932**
2	lung	6.3935	3.688	7.6508	**3.5876**
3	bone	8.7506	3.2533	3.1033	**3.0221**
4	bone	8.0978	4.3529	5.7742	**3.4321**
5	fat	8.8243	3.1907	2.685	**2.5203**
6	fat	9.3355	4.3106	3.6281	**2.7702**
7	muscle	9.2740	6.9097	6.9131	**6.0375**
8	muscle	5.7516	6.4899	5.2064	**4.6562**

To show how the gain on the large tissue volumes of lung, bone, fat, and muscle can lead to the gain on the texture preservation of small lung nodule or colon polyp inside the large tissue volumes, the above procedure of extracting texture information from FdCT and performing texture-preserving LdCT image reconstruction was repeated to the sinogram data of the two patients, one with a nodule and the other with a polyp, respectively. Figure 4.8 shows the reconstructed images of the two patients acquired from routine protocol of full-dose level (120 kV, 100 mAs) where the ROIs were selected to compute the textures. The simulated low-dose scans were reconstructed by the four algorithms of FBP, PWLS-GMRF, PWLS-Huber, and MRF-texture. The textures from the full-dose scans were used as the reference when comparing the texture distance of the four algorithms. Table 4.2 and Table 4.3 show the experimental outcomes. The gain from the known large tissue volumes led to a noticeable gain on the unknown small nodule or polyp.

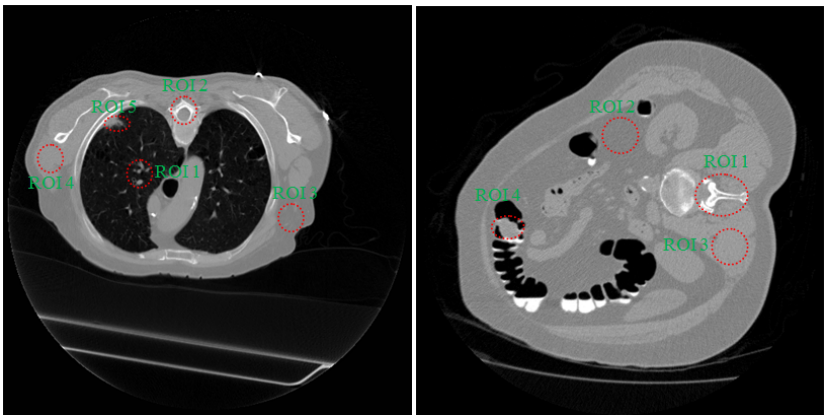

Figure 4.8. Reconstructed transverse slice of two patients from full-dose acquisitions: (a) containing a lung nodule as indicated by ROI 5; (b) containing a colon polyp as indicated by ROI 4.

Table 4.2. Texture distance between the reference full-dose image in Figure 4.8(a) and the reconstructed low-dose images by the four reconstruction algorithms.

ROI	Tissue type	FBP	PWLS-GMRF	PWLS-Huber	PWLS-texture
1	lung	6.4241	5.7532	9.9530	**5.0552**
2	bone	8.6492	5.6968	5.9468	**2.5173**
3	fat	7.3578	7.4379	7.4194	**6.6144**
4	muscle	11.6797	3.8456	5.8283	**2.8951**
5	lung nodule	9.9584	4.5440	5.1329	**4.3407**

Table 4.3. Texture distance between the reference full-dose image in Figure 4.8(b) and the reconstructed low-dose images by the four reconstruction algorithms.

ROI	Tissue type	FBP	PWLS-GMRF	PWLS-Huber	PWLS-texture
1	bone	8.8206	7.8440	6.1991	**4.7278**
2	fat	8.9881	7.5032	6.1540	**5.2425**
3	muscle	8.2534	9.3631	9.2090	**7.9403**
4	colon polyp	9.7208	7.0602	5.8975	**4.5296**

4.4.2 Experiments on real low-dose sinogram data

1). Image reconstruction

To evaluate the proposed *a priori* knowledge model in a more realistic situation, the real low-dose sinogram data (120 kV, 20 mAs) of the same patient (of Figure 4.5) was also used to perform a pilot clinical study. The slice #45 of the low-dose scan roughly matches the slice #60 of the full-dose scan by visual judgment. Therefore, we employed the MRF coefficients sets (as shown in Figure 4.3 and Figure 4.4) predicted from the slice #60 and its neighboring slices of the full-dose scan to reconstruct the slice #45 of the low-dose scan.

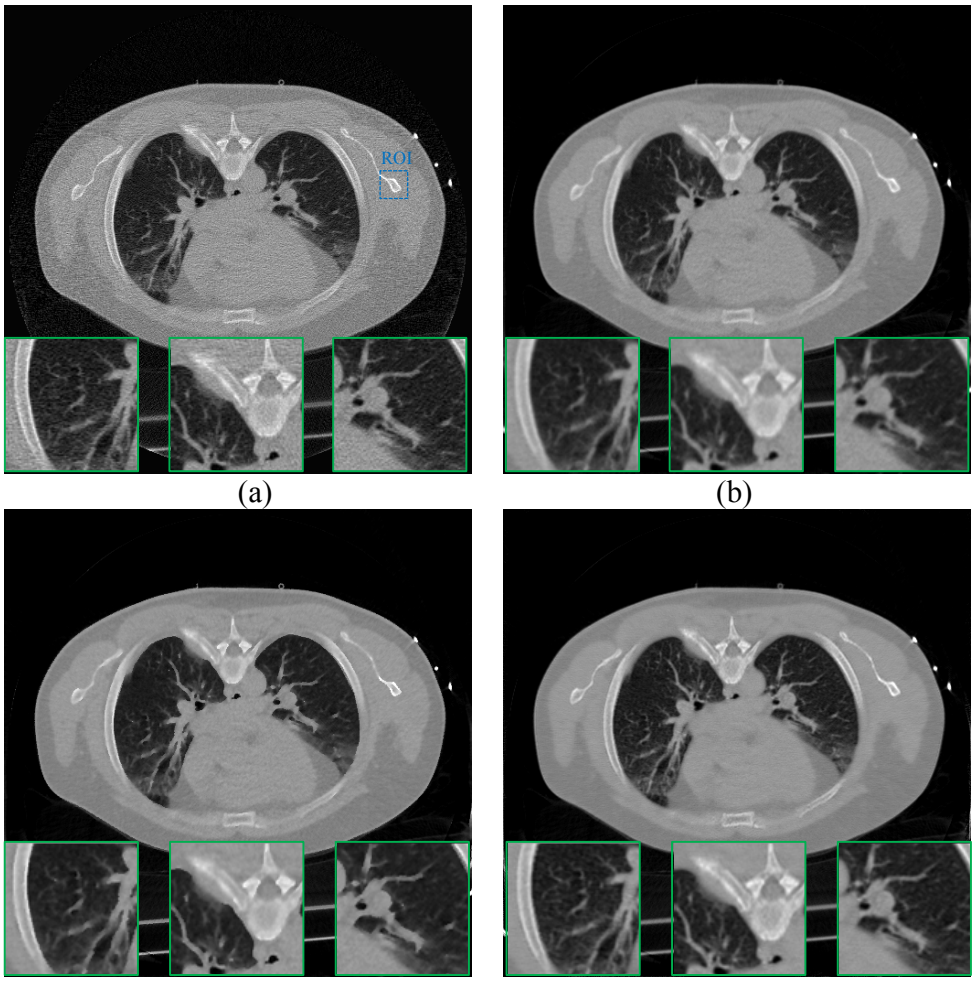

Figure 4.9. Reconstructed transverse slice of the patient data from the low-dose 20 mAs sinogram: (a) The FBP reconstruction; (b) The PWLS-GMRF reconstruction, $\beta = 1\times10^5$; (c) The PWLS-Huber reconstruction, $\beta = 1\times10^5$, δ=0.004; and (d) The MRF-T60 reconstruction, $\beta = 1\times10^5$. All the images are displayed with the same window [0, 0.034] mm^{-1}.

In the first scenario of using the MRF coefficients of the slice #60, the reconstructed images from the low-dose 20 mAs sinogram by the FBP, PWLS-GMRF, PWLS-Huber and MRF-T60 methods are shown in Figure 4.9. It is evident that all the three MRF methods outperformed the FBP method in terms of noise suppression, and the MRF-T60 result is superior to the PWLS-GMRF and the PWLS-Huber in terms of edge/detail preservation.

In the second scenario of using the MRF coefficients set of the nearby slices around the slice #60, (i.e., slice #58, #59, #60, #61, #62) of the full-dose scan to reconstruct the slice #45 of the low-dose 20 mAs sinogram data, Figure 4.10 shows the results of our proposed PWLS-texture method. By visual judgment, the reconstructed images in Figure

4.10 are very similar to each other, concurring with the simulation results of Figure 4.6. Quantitative measures on the results of Figure 4.9 and Figure 4.10 are given below.

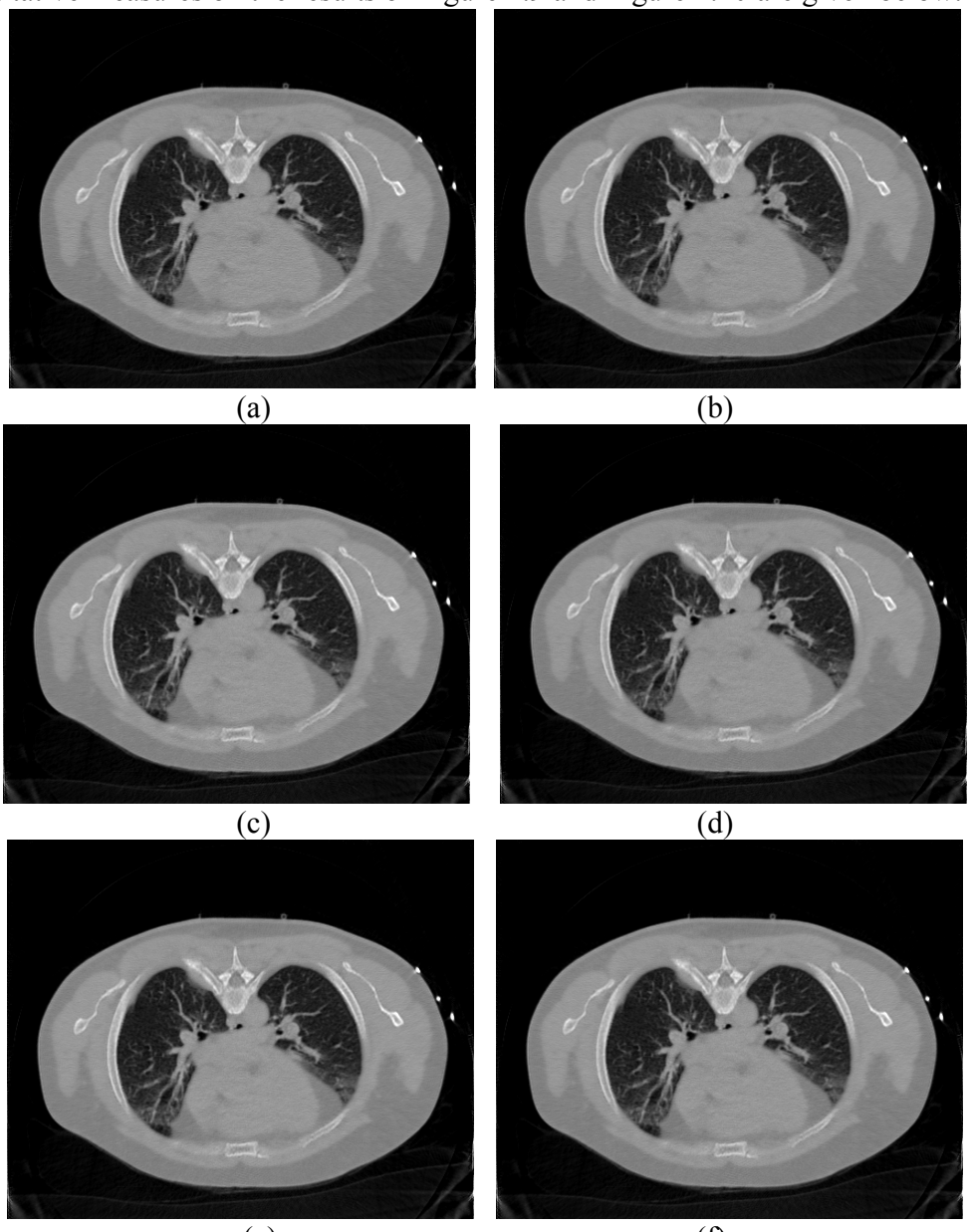

Figure 4.10. Reconstructed transverse slice of the patient by the proposed PWLS-texture algorithm from the low-dose 20 mAs sinogram: (a) The MRF-T58 reconstruction; (b) The MRF-T59 reconstruction; (c) The MRF-T60 reconstruction; (d) The MRF-T61 reconstruction; (e) The MRF-T62 reconstruction; and (f) The MRF-T58-62 reconstruction. All the images are displayed with the same window [0, 0.034] mm^{-1}.

2). Normal vector flow study

The NVF images of a ROI as indicated in Figure 4.9(a) were also plotted for the results of the four different reconstruction methods of Figure 4.9, and the corresponding

NVF images are illustrated in Figure 4.11. The NVF image of Figure 4.7(a) can be served as a reference for comparison, because that image was made from a similar ROI as that in Figure 4.9(a). Despite the lacking of golden standard in this real clinical low-dose data pilot study, yet we can still observe similar phenomena as those claimed in the simulation study. And the NVF image of the presented PWLS-texture algorithm in Figure 4.11(d) has the best match to the reference in Figure 4.7(a), indicating that the textures of the corresponding reconstructed image were best preserved by our proposed *a priori* knowledge model.

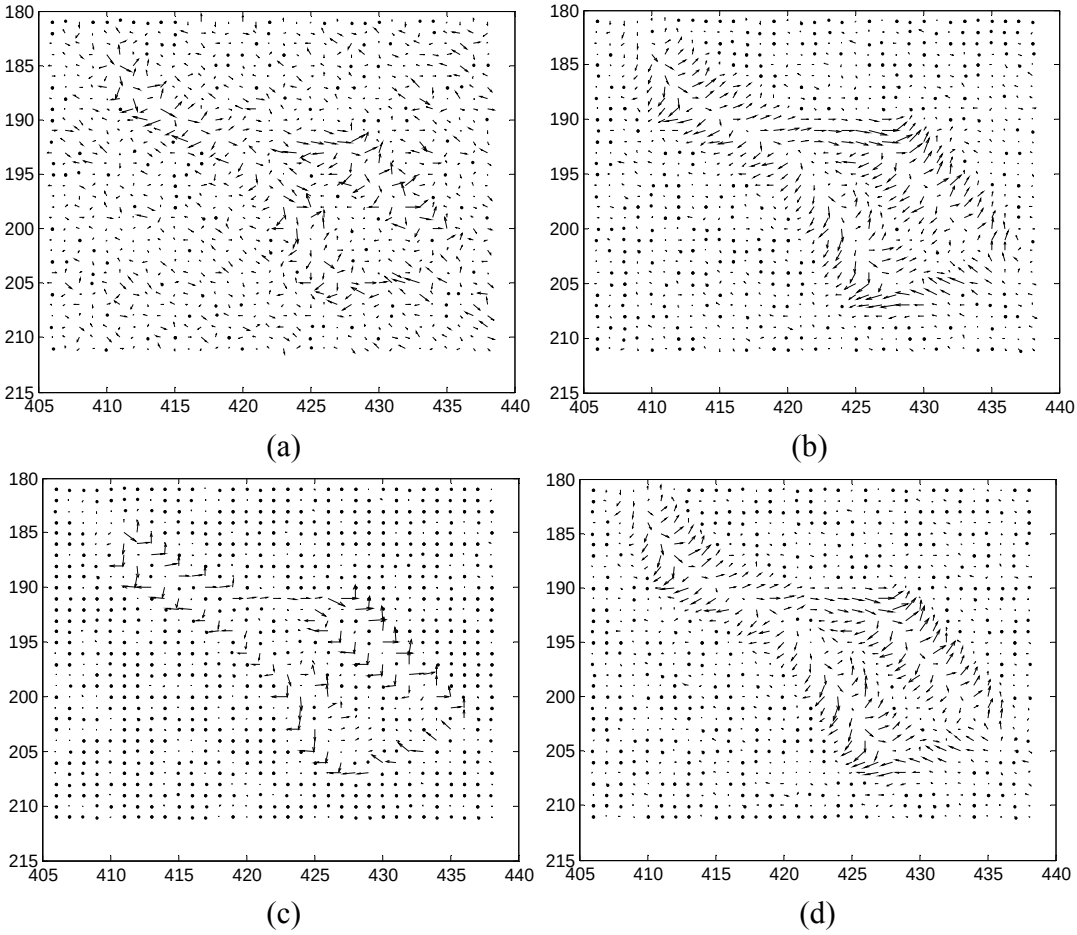

Figure 4.11. NVF images of a ROI labeled in Figure 4.9(a). The NVF images in Figure 4.11(a)-(d) are corresponding to the reconstructions in Figure 4.9(a)-(d).

3). Evaluation by physician experts

In an effort to qualitatively compare the results of the four different reconstruction methods, three experienced physicians were asked to score the reconstructed images from 0 (worst) to 10 (best) in terms of noise reduction and resolution/contrast/ detail/texture preservation. The reconstructed images by different methods were displayed on the screen randomly, so it was a completely blind procedure for the physicians. Table 4.4 lists the physicians' scores on the reconstructed image quality under three different display windows: bone window (BW), soft tissue window (TW), and lung window (LW).

It is evident that the reconstructed image by our proposed PWLS-texture algorithm generally has the highest scores (with mean 7.56) and, therefore, outperformed the other three methods (with mean 3.22 for FBP, 5.67 for PWLS-GMRF, and 5.44 for PWLS-Huber, respectively) from the physicians' point of view.

Table 4.4. Physicians' scoring of the reconstructed image quality in Figure 4.9 by the four reconstruction methods.

	Physician #1			Physician #2			Physician #3		
	BW	TW	LW	BW	TW	LW	BW	TW	LW
FBP	3	3	2	5	4	5	3	2	2
PWLS-GMRF	7	5	4	6	5	7	5	6	6
PWLS-Huber	5	5	5	6	5	6	7	6	4
MRF-T60	**8**	**7**	**7**	**7**	**5**	**9**	**9**	**8**	**8**

4.5 Discussion and conclusion

In this chapter, we introduced a previous full-dose high-quality CT scan induced MRF penalty model for Bayesian image reconstruction of subsequent low-dose scans. The proposed *a priori* knowledge model considers the anatomical similarity among the reconstructed image series of the previous full-dose and current low-dose scans and utilizes the full-dose image to predict region-specific MRF model coefficients, which have been routinely specified by an *ad hoc* manner based on the nearby image voxel distance to the concerned voxel. The presented *a priori* knowledge model further considers the tissue specific patterns in addition to the anatomical similarity and makes the MRF model coefficients adaptive to be regionally specific, resulting in the elimination of the demand for point-by-point image registration between the full- and low-dose scans in the prediction of the model coefficients (Zhang et al. 2014). Experimental outcomes showed noticeable gain by the proposed *a priori* knowledge model compared to the well-known generic GMRF penalty and Huer penalty (which are based on the distance model coefficients), in terms of computer-based merits and physician assessment on the reconstructed images. Essentially, the generic MRF penalty encourages regional smoothness and edge sharpness, lacking a mechanism to preserve the tissue specific characteristics or patterns (i.e., image textures). The proposed MRF-texture model takes advantages of the generic MRF penalty's neighborhood system and also brings the *a priori* knowledge of the image textures into the LdCT image reconstruction. Particularly, the gain on textures of the nodule and polyp is clinically important because (1) the majority of nodules and polyps are benign and differentiation of malignant vs. benign is necessary and (2) the image textures play an important role in the lesion differentiation.

Also, in this proof-of-concept study, we used 2D MRF window (with size 7×7) when computing the MRF model coefficients and reconstructing each transverse image, while the 3D volume was formed as a stack of 2D transverse images. Although lacking of regularization in axial direction, we did not observe artifacts in the coronal or sagittal views of the reconstructed volume. However, a 3D MRF window (e.g., with size 7×7×3),

which results in fully 3D MRF-texture regularization, may be beneficial and would be investigated in our future study.

Chapter 5. Adaptive nonlocal means-regularized statistical image reconstruction for low-mAs CT

The reconstructed CT images by the conventional filtered back-projection (FBP) method from the low-mAs acquisitions may be severely degraded due to the excessive noise. The well-known edge-preserving nonlocal means (NLM) filtering can reduce the noise-induced artifacts in the FBP reconstructed image, but it sometimes cannot completely eliminate the artifacts, especially under the very low-dose circumstance when the image is severely degraded. Instead of taking NLM filtering, we proposed a NLM-regularized statistical image reconstruction scheme, which can effectively suppress the noise-induced artifacts and significantly improve the reconstructed image quality. Also, we noted that using a spatially-invariant filtering parameter in the regularization was rarely optimal for the entire field of view (FOV). Therefore, we developed a novel strategy for designing spatially-variant filtering parameters which are adaptive to the local characteristics of the image to be reconstructed. In this chapter, the adaptive NLM-regularized statistical image reconstruction method was evaluated with low-contrast phantoms and clinical patient data to show (1) the necessity in introducing the spatial adaptivity and (2) the efficacy of the adaptivity in achieving superiority in reconstructing CT images from low-mAs acquisitions.

5.1 Introduction

The nonlocal means (NLM) algorithm was introduced by Buades et al for image de-noising (Buades et al. 2005). Essentially, it is one of the nonlinear neighborhood filters which reduce image noise by replacing each pixel intensity with a weighted average of its neighbors according to the similarity. The similarity comparison could be performed between any two pixels within the entire image, although it is limited to a fixed neighboring window area (e.g., 17×17) of target pixel for computation efficiency in practice. Inspired by its success in image processing scenario, researchers further extended it to the medical imaging applications such as the low-dose CT. For instance, Giraldo et al (Giraldo et al. 2009) examined its efficacy on CT images for noise reduction. Ma et al (Ma et al. 2011) tried to restore the low-mAs CT images using previous normal-dose scan via the NLM algorithm, and observed noticeable gains over the traditional NLM filtering. Similarly, Xu and Muller (Xu and Mueller 2012) added effort to restore the sparse view CT images using high quality prior scan and artifact-matched prior scan with the NLM algorithm and also noticed remarkable improvements. However, these methods are essentially post-reconstruction filtering or restoration, which do not fully take advantage of the projection data. The traditional NLM filtering (Giraldo et al. 2009) sometimes cannot completely eliminate the noise and streak artifacts. The extensions (Ma et al. 2011; Xu and Mueller 2012) need high quality prior scan and necessary registration to align the images from two different scans. Furthermore, researchers also explored the

NLM-based regularizations for several inverse problems, including image reconstructions for magnetic resonance imaging, positron emission tomography and X-ray CT. For instance, Tian et al (Tian et al. 2011) presented a temporal NLM regularization for 4D dynamic CT reconstruction, where the reconstruction of current frame image utilizing two neighboring frame images. Ma et al (Ma et al. 2012) proposed previous normal-dose CT scan induced NLM regularizations to improve the follow-up low-dose CT scans reconstruction. However, for some applications, the neighboring frame images or previous normal-dose scan may not be available. In this study, we explored to incorporate a NLM-based generic regularization into the SIR framework for low-dose CT, wherein the regularization only utilizes information of the current scan.

5.2 Overview of the NLM algorithm

The NLM method was proposed as a non-iterative and edge-preserving filter for image de-noising. It reduces image noise by replacing each pixel's intensity with a weighted average of its neighbors according to similarity. Although the similarity comparison could be performed between any two pixels within the entire image, it is typically limited to a fixed neighboring window area (called search-window (SW), e.g., 17×17, in 2D case) of target pixel in practice for computation efficiency. Mathematically, the NLM method can be describes as (Buades et al. 2005):

$$NLM(\hat{\mu}_j) = \sum_{k \in SW_j} w_{jk}(\hat{\boldsymbol{\mu}})\hat{\mu}_k \tag{5.1}$$

where $\hat{\boldsymbol{\mu}} = (\hat{\mu}_1, ..., \hat{\mu}_J)^T$ represents the noisy image to be smoothed, and $NLM(\hat{\mu}_j)$ is the intensity value of pixel j after the NLM filtering.

However, different from the previous neighborhood filters, the NLM calculates the similarity based on patch instead of a single pixel. A patch of a pixel can be defined as a squared region centered at that pixel (called patch-window (PW), e.g., 5×5, in 2D case). Let $\mathbf{P}(\hat{\mu}_j)$ denote the patch centered at pixel j and $\mathbf{P}(\hat{\mu}_k)$ denote the patch centered at pixel k. The similarity between pixels j and k depends on the weighted Euclidean distance of their patches $\left\|\mathbf{P}(\hat{\mu}_j) - \mathbf{P}(\hat{\mu}_k)\right\|_{2,a}^2$. The exponential function converts the similarity to weighting coefficient which indicates the interaction degree between two pixels. Specifically, the weighting coefficient is given as:

$$w_{jk}(\hat{\boldsymbol{\mu}}) = \frac{\exp\left(-\left\|\mathbf{P}(\hat{\mu}_j) - \mathbf{P}(\hat{\mu}_k)\right\|_{2,a}^2 / h^2\right)}{\sum_{k \in SW_j} \exp\left(-\left\|\mathbf{P}(\hat{\mu}_j) - \mathbf{P}(\hat{\mu}_k)\right\|_{2,a}^2 / h^2\right)} \tag{5.2}$$

The parameter h in Eq. (5.2) controls the decay of the exponential function as well as the weighting coefficient. When h is small, the image tends to be weakly smoothed, and *vice versa*. For simplicity, h is called filtering parameter hereafter. According to (Buades et al. 2005), the filtering parameter h is a function of the standard deviation of the image noise. And if we further consider the size of the patch-window, the parameter h can be given as (Coupé et al. 2008):

$$h^2 = \tau\sigma^2 = 2\eta\sigma^2 \left|PW_j\right| \tag{5.3}$$

where τ and η are free scalar parameters, σ is the standard deviation of the image noise, and $\left|PW_j\right|$ denotes the size of the patch-window. However, it is well known that the noise distribution of low-dose CT images is non-stationary, so determining the standard deviation σ is not a trivial task. In the past, the parameter h has been simply set to be a global constant for the entire FOV, although such a practice may result in suboptimal filtering result. Besides, the NLM filter usually cannot effectively suppress the streak artifacts of low-dose CT images.

5.3 Adaptive NLM-regularized statistical image reconstruction

5.3.1 NLM-based regularization

Motivated by the work of NLM filter, Buades *et al.* (Buades et al. 2006) proposed the regularization model :

$$U(\boldsymbol{\mu}) = \sum_j \phi\left(\mu_j - \sum_{k\in SW_j} w_{jk}(\tilde{\boldsymbol{\mu}})\mu_k\right) \tag{5.4}$$

where $\tilde{\boldsymbol{\mu}}$ is a reference image, and the weighting coefficient $w_{jk}(\tilde{\boldsymbol{\mu}})$ is calculated from $\tilde{\boldsymbol{\mu}}$. However, a good reference image is usually not available before image reconstruction for low-dose CT. Lou *et al.* (Lou et al. 2010) suggested to use the FBP reconstruction result as the reference image, but such a reference image is typically noisy and the resulting regularization in Eq.(5.4) may lead to suboptimal reconstruction result.

To improve the reconstruction accuracy, in this work, we intend to make the regularization model be generic and thus take the following form:

$$U(\boldsymbol{\mu}) = \sum_j \phi\left(\mu_j - \sum_{k\in SW_j} w_{jk}(\boldsymbol{\mu})\mu_k\right), \text{ and } w_{jk}(\boldsymbol{\mu}) = \frac{\exp\left(-\left\|\mathbf{P}(\mu_j) - \mathbf{P}(\mu_k)\right\|_{2,a}^2 / h^2\right)}{\sum_{k\in SW_j} \exp\left(-\left\|\mathbf{P}(\mu_j) - \mathbf{P}(\mu_k)\right\|_{2,a}^2 / h^2\right)} \tag{5.5}$$

There are several choices for the potential function, but in this study, we only explored the regularization where $\phi(\Delta) = \Delta^2$. This choice makes the PWLS cost function quadratic and easy to optimize. We also utilized this as an example to demonstrate the feasibility and efficacy of the presented NLM-based regularizations for low-dose CT reconstruction, although some other potential functions (e.g. $\phi(\Delta) = |\Delta|^p$ $(1 < p < 2)$) may further improve the performance.

5.3.2 Local adaption of the filtering parameter h

The filtering parameter h determines the smoothness of the resulting image, where larger h results in more smoothing and smaller h results in less smoothing. In the previous studies, the h in the NLM-based regularizations was often set to be a constant across the entire FOV. However, when the local characteristics of the image differ significantly across the entire FOV, a constant h may result in inferior/suboptimal reconstruction result, since it may be too large for some regions (blurring edges and subtle structures) while too small (filtering little) for other regions within the image domain. To mitigate this issue, in this study, we propose a novel locally-adaptive estimation of the filtering parameter h at pixel j as:

$$h_j^2 = s \bullet mean\left\{\left\|\mathbf{P}(\mu_j) - \mathbf{P}(\mu_k)\right\|_{2,a},\ k \in SW_j\right\} + t \tag{5.6}$$

where s and t are two constants, and can be determined through experiments.

The rationale behind the mathematical expression of Eq. (5.6) is that the value of h should depend on the similarity between the patch of target pixel and the patches within the corresponding SW. That is, when SW contains many similar patches to $\mathbf{P}(\mu_j)$, h needs to be decreased to reduce the influence of the other patches. On the contrary, when very few similar patches exist in SW for $\mathbf{P}(\mu_j)$, h needs to be increased to relax the selection(Coupé et al. 2011). To achieve robust implementation of the similarity dependence in Eq. (5.6), the constant t is introduced to ensure numerical stability and adequate filtering for uniform regions, and the constant s is introduced to control the relative filtering strength for non-uniform regions in the image domain.

5.3.3 Adaptive NLM-regularized statistical image reconstruction

Using the regularization presented above, our PWLS image reconstruction scheme for low-dose CT can be summarized as follows:

$$\boldsymbol{\mu}^* = \arg\min_{\mu \geq 0} \left\{ (\mathbf{y} - \mathbf{A}\boldsymbol{\mu})^T \mathbf{D}(\mathbf{y} - \mathbf{A}\boldsymbol{\mu}) + \beta \sum_j \left(\mu_j - \sum_{k \in SW_j} w_{jk}(\boldsymbol{\mu}) \mu_k \right)^2 \right\} \tag{5.7}$$

Since the weighting coefficients in the regularization are computed on the unknown image $\boldsymbol{\mu}$, direct minimization of the objective function in Eq. (5.7) using the regularization in Eq. (5.5) can be very complicated. Instead, an empirical one-step-late (OSL) implementation is employed, based on the Gauss-Seidel (GS) updating strategy, for the minimization task in this study, where the weighting coefficients are computed on current image estimate and then are assumed to be constants when updating the image. Although there is no proof of global convergence for such an OSL iteration scheme, it is observed that the image estimation converges to a steady status after 20 iterations (the difference between the estimated images of two successive iterations becomes very small) for all the datasets presented in this study.

5.4 Experiments and results

In this work, three categories of projection data were utilized to validate the performance of the proposed adaptive NLM-regularized statistical image reconstruction method (referred to as PWLS-adaptiveNLM) for X-ray CT imaging from low-dose acquisitions. For comparison purpose, the standard FBP reconstruction, the FBP reconstruction followed by NLM filtering (referred to as FBP+NLM filtering), the NLM-regularized statistical image reconstruction with constant filtering parameter (referred to as PWLS-NLM), and the total variation regularized statistical image reconstruction (referred to as PWLS-TV) were also implemented in a similar fashion as the implementation of the proposed method. To ensure the fairness of comparison, the parameters for each method were carefully tuned to obtain the best image quality.

5.4.1 Digital clock phantom

1). Projection data acquisition

A computer simulated clock phantom was utilized in this study, which is modified from the reported one in (Evans et al. 2011). The clock phantom consists of a water background and eight circular inserts with different contrasts (C1: -100%, C2: +150%, C3: +7%, C4: -50%, C5: +85%, C6: -15%, C7: -7%, C8: +30%). The low-dose sinogram data of the clock phantom was acquired using the simulation method in (La Rivière and Billmire 2005). After calculating the noise-free line integral, the noisy measurement N_i at detector bin i was generated according to the statistical model:

$$N_i \sim \text{Poisson}(\bar{N}_{0i} \exp(-\bar{y}_i)) + \text{Gaussian}(0, \sigma_e^2) \tag{5.8}$$

where $\bar{N}_{0i}$ was set to be 3×10^4 and σ_e^2 was set to be 10 in this study. Then the corresponding noisy line integrals were calculated by the logarithm transform. The scanning geometry was the same as the Siemens Somatom Sensation 16 CT scanner (Siemens Healthcare, Forchheim, Germany).

2). Visualization-based evaluation

The reconstructed images by the FBP, FBP+NLM filtering, PWLS-NLM, PWLS-adaptiveNLM and PWLS-TV from the simulated low-dose sinogram are shown in Figure 5.1(b)-(f). The zoom-in views of three low-contrast inserts (C3: +7%, C6: -15%, C7: -7%) by different reconstruction methods are also illustrated. We can see that the FBP+NLM filtering can suppress the noise in the FBP reconstructed image to a large extent, but it is still not comparable to the PWLS-NLM reconstructed image. However, since these two methods use a constant filtering parameter, their outcomes seem to blur the low-contrast inserts substantially. In contrast, the PWLS-adaptiveNLM method can effectively suppress the noise while retaining the low-contrast objects. Finally, the PWLS-TV reconstructed image slightly suffers from patchy artifacts in the uniform region, and the low-contrast inserts are also considerably distorted.

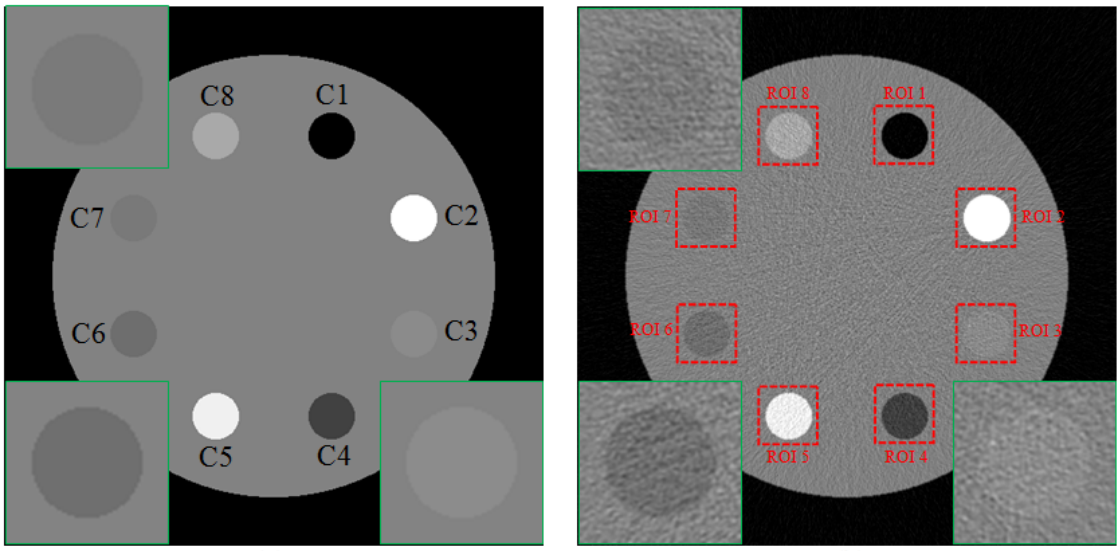

(a) (b)

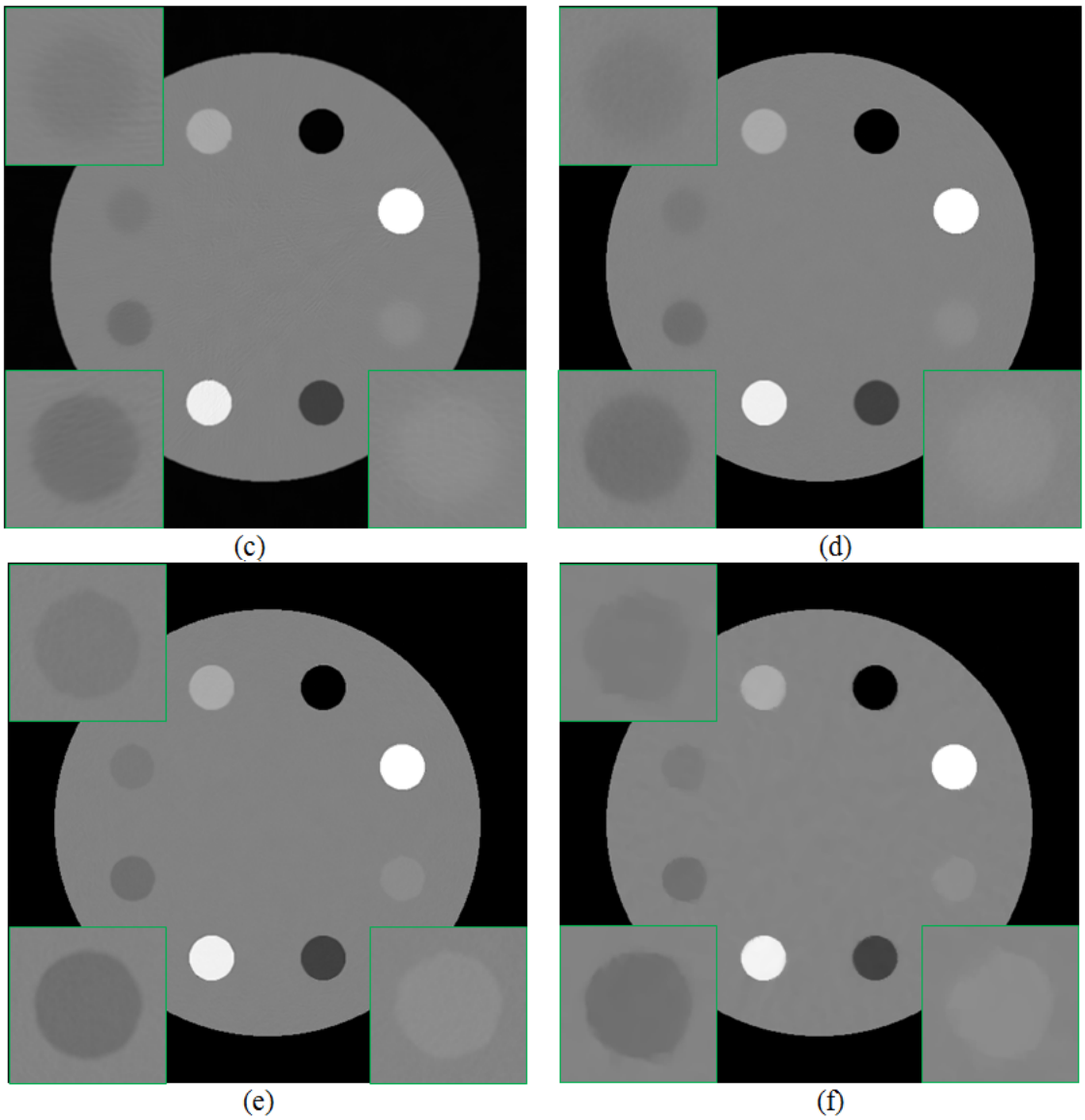

Figure 5.1. One slice of the clock phantom: (a) phantom; (b) FBP reconstruction from simulated noisy sinogram; (c) FBP+NLM filtering from simulated noisy sinogram (h=0.012); (d) PWLS-NLM reconstruction from simulated noisy sinogram ($\beta=5\times10^{6}$, h=0.008); (e) PWLS-adaptiveNLM reconstruction from simulated noisy sinogram ($\beta=5\times10^{6}$, $s=5\times10^{-4}$, $t=4\times10^{-6}$); (f) PWLS-TV reconstruction from simulated noisy sinogram ($\beta=2\times10^{3}$). All the images are displayed with the same window.

3). Noise reduction performance

To evaluate the noise reduction performance of the different reconstruction methods, two quantitative metrics were employed. According to Table 5.1, the proposed PWLS-adaptiveNLM method offers the highest PSNR and lowest NMSE, and therefore outperforms other methods in term of noise reduction, which is consistent with the visual inspection.

Table 5.1. Noise reduction performance of the five reconstruction methods for the clock phantom

Metrics	FBP	FBP+NLM filtering	PWLS-NLM	PWLS-adaptiveNLM	PWLS-TV
PSNR (dB)	29.32	36.15	44.25	44.87	42.69
NMSE (1e-4)	129.12	26.80	4.15	3.61	5.95

4). Assessing local image quality

In order to evaluate the performance of different methods on the reconstruction of fine structures, we chose eight ROIs in the clock phantom, as labeled by the red rectangles in Figure 5.1(b). Since the FBP reconstructed image was obviously worse than those by the other four methods due to the excessive noise, we excluded it and only compared the local image quality by the other four methods. The quantitative results with RMSE and UQI are illustrated in Figure 5.2. Still, the proposed PWLS-adaptiveNLM has the best local image quality for the eight detailed ROIs with the lowest RMSE and highest UQI. The UQI quantifies the noise, spatial resolution, and texture correlation. From Figure 5.2(b), it is noted that the UQI values of the high-contrast ROIs (including C1: -100%, C2: +150%, C4: -50%, C5: +85%, C8: +30%) by the four different methods are relatively high and comparable, while the UQI values of the low-contrast ROIs (including C3: +7%, C6: -15%, C7: -7%) by the four different methods are relatively low and differ substantially. These results suggest that the low-contrast objects are more difficult to recover but the PWLS-adaptiveNLM method performed well in recovering them. It is well-known that the low-contrast objects can be very critical in clinic.

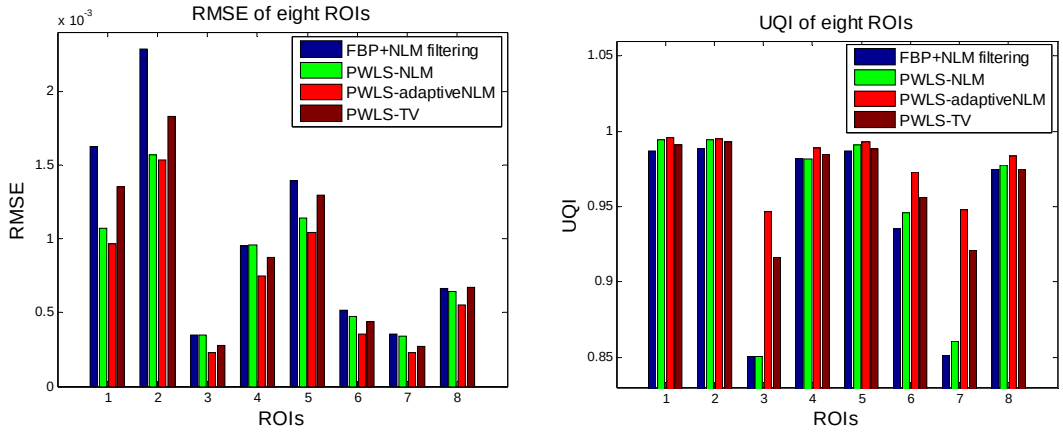

Figure 5.2. Performance comparison of the four methods on reconstruction of the eight ROIs labeled in Figure 5.1(b) with RMSE and UQI metrics. The corresponding methods are illustrated in figure legend.

5.4.2 Physical anthropomorphic torso phantom

1). Projection data acquisition

To evaluate the above presented reconstruction algorithm in a more realistic situation, an anthropomorphic torso phantom (Radiology Support Devices, Inc., Long Beach, CA) was used for experimental projection data acquisition. The phantom was scanned by the same clinical Siemens scanner in a cine mode at a fixed bed position. The X-ray tube

voltage was set to be 120 kV and the mAs level was set to be 40 mAs. The CT scanner was rotated 150 times around the torso phantom.

The central slice sinogram data of one scan was extracted and regarded as the low-dose scan. The averaged sinogram data of that slice from 150 repeated scans was reconstructed by the FBP method to serve as the ground truth image for evaluation purpose.

2). Visualization-based evaluation

Figure 5.3(a) shows one transverse image of the anthropomorphic torso phantom reconstructed by the FBP method from the averaged sinogram of 150 repeated scans, which serves as the ground truth image for evaluation. Figure 5.3(b)-(f) illustrates the reconstructed images by the FBP, FBP+NLM filtering, PWLS-NLM, PWLS-adaptiveNLM and PWLS-TV from a low-dose 40 mAs sinogram. The FBP+NLM filtering method can suppress the noise pretty well, but there are still tiny streak artifacts in the image. The three PWLS methods outperform the FBP+NLM in terms of streak artifacts suppression, which can be attributed to the statistical modeling of the sinogram data. From the zoom-in views of the detailed regions, we can observe that the PWLS-adaptiveNLM method is superior to the PWLS-NLM and PWLS-TV on the reconstruction of the fine structures.

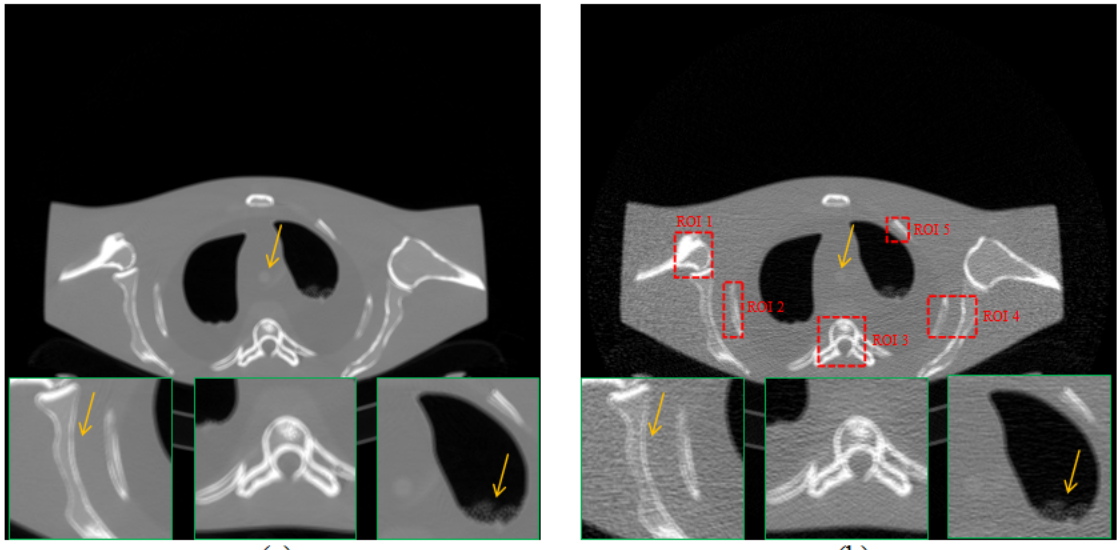

(a) (b)

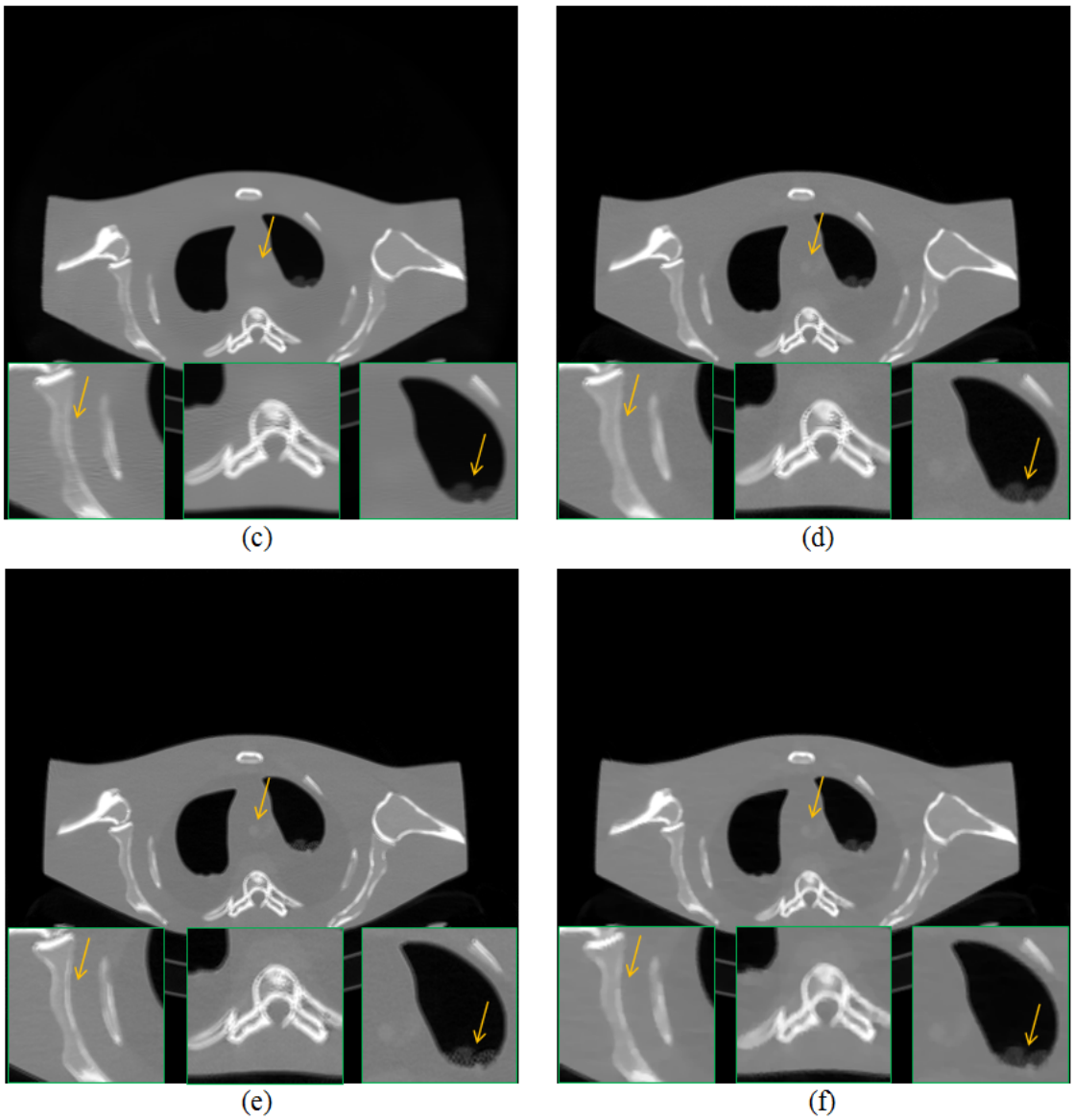

Figure 5.3. A reconstructed slice of the anthropomorphic torso phantom: (a) FBP reconstruction from the averaged sinogram; (b) FBP reconstruction from the 40 mAs sinogram; (c) FBP+NLM filtering from the 40 mAs sinogram (h=0.012); (d) PWLS-NLM reconstruction from the 40 mAs sinogram ($\beta=3\times10^{5}$, h=0.008); (e) PWLS-adaptiveNLM reconstruction from the 40 mAs sinogram ($\beta=3\times10^{5}$, $s=5\times10^{-4}$, $t=4\times10^{-6}$); (f) PWLS-TV reconstruction from the 40 mAs sinogram ($\beta=200$). All the images are displayed with the same window.

3). Noise reduction performance

Table 5.2 lists the quantitative results of the five different reconstruction methods on the anthropomorphic torso phantom with PSNR and NMSE metrics. The proposed PWLS-adaptiveNLM method also demonstrates better performance than the other four methods on image noise reduction.

Table 5.2. Noise reduction performance of the five reconstruction methods for the anthropomorphic torso phantom

Metrics	FBP	FBP+NLM filtering	PWLS-NLM	PWLS-adaptiveNLM	PWLS-TV
PSNR (dB)	31.00	38.91	39.17	39.39	39.09
NMSE (1e-4)	148.54	24.06	22.62	21.54	23.11

4). Assessing local image quality

To quantitatively demonstrate the benefits of the proposed PWLS-adaptiveNLM method, we compare the performance of the four methods on the reconstruction of ROIs with fine structures, which are labeled with red rectangles in Figure 5.3(b). The corresponding quantitative results based on the RMSE and UQI metrics are shown in Figure 5.4. Again, the PWLS-adaptiveNLM method yielded the lowest RMSE and the highest UQI for all the five detailed ROIs.

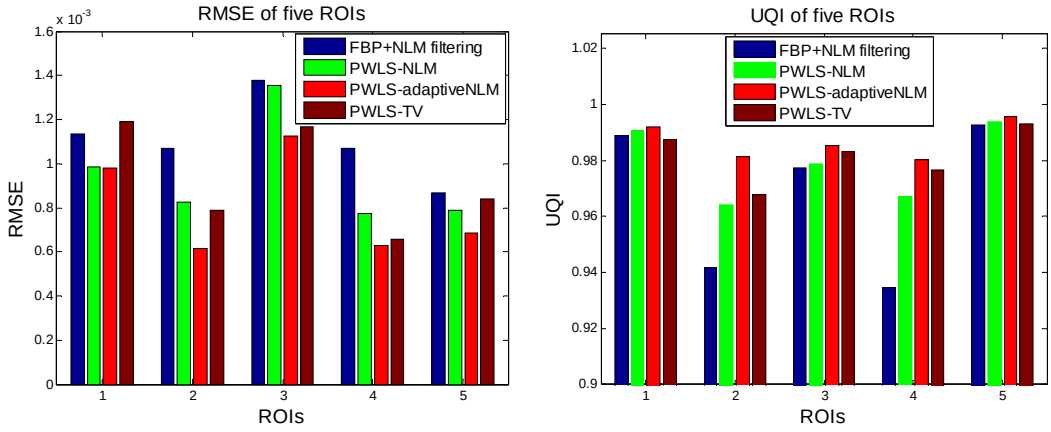

Figure 5.4. Performance comparison of the four methods on the reconstruction of detailed ROIs labeled in Figure 5.3(b) with RMSE and UQI metrics. The corresponding methods are illustrated in figure legend.

5.4.3 Clinical patient data

1). Projection data acquisition

The projection data of a patient were acquired using the same Siemens scanner after obtaining informed consent from the patient, and this clinical data serve as a pilot clinical study. The patient was scheduled for CT scan for medical reasons. The X-ray tube voltage was 120 kV, and the mAs level was 20 mAs, which was considered as ultra low-dose scan in clinic.

2). Visualization-based evaluation

The reconstructed images by the FBP, FBP+NLM filtering, PWLS-NLM, PWLS-adaptiveNLM and PWLS-TV from the ultra low-dose 20 mAs sinogram of the patient are shown in Figure 5.5(a)-(e). We can see that the FBP+NLM filtering method cannot eliminate the streak artifacts in the image, while the three PWLS methods do not have such problem due to the statistical modeling of the sinogram data. However, the PWLS-TV exhibits slight patchy artifacts in the region indicated by the arrow, which is also reported in (Tang et al. 2009). From the zoom-in views of the three detailed regions, we can also see that the PWLS-adaptiveNLM method outperforms the other methods on the

reconstruction of the fine structures. However, for the patient study, we cannot implement the quantitative evaluations as the phantom studies due to the lack of ground truth image. Still, we observe that the patient study exhibits the same trend as the phantom studies through visual inspection.

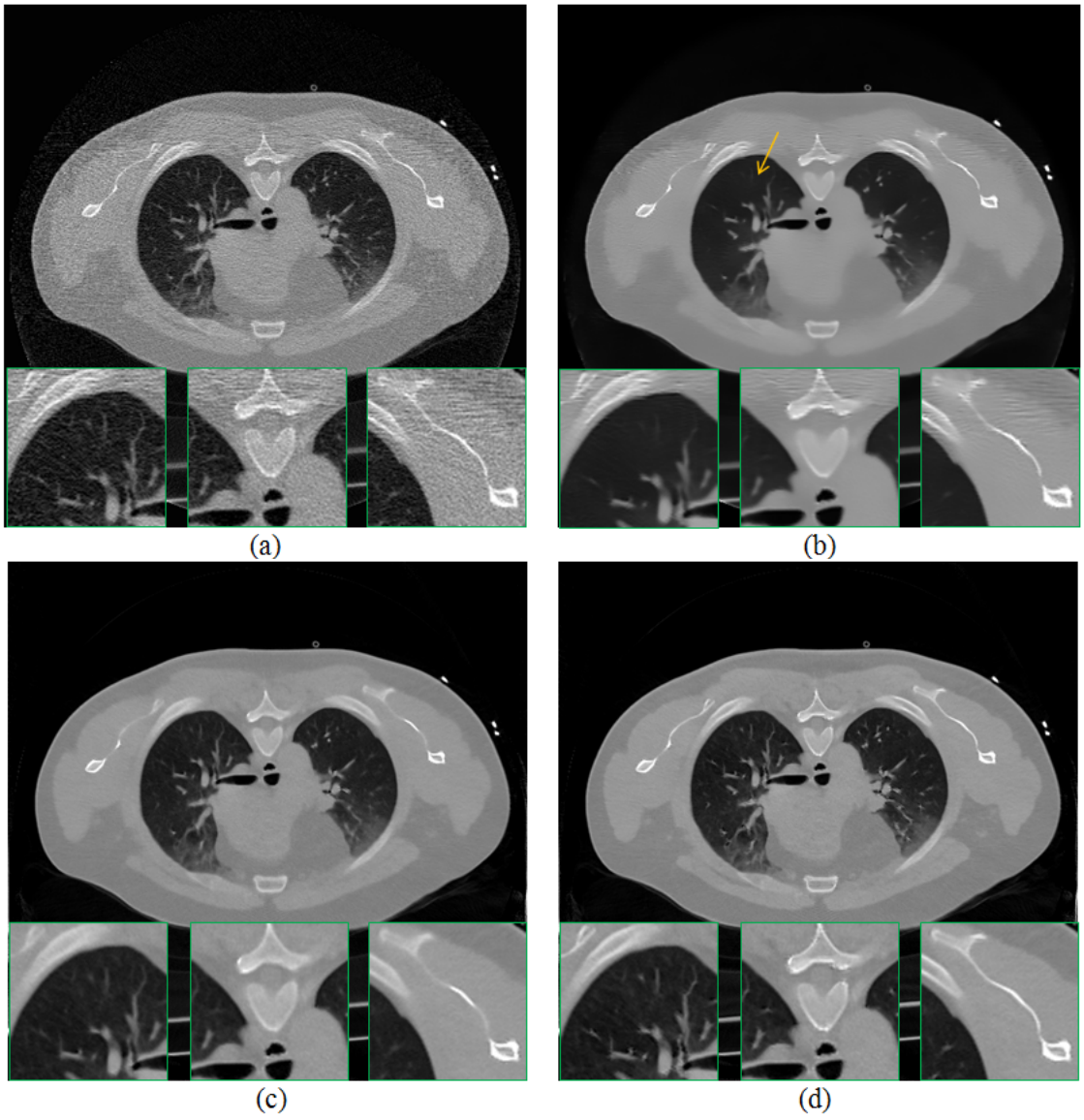

(a) (b) (c) (d)

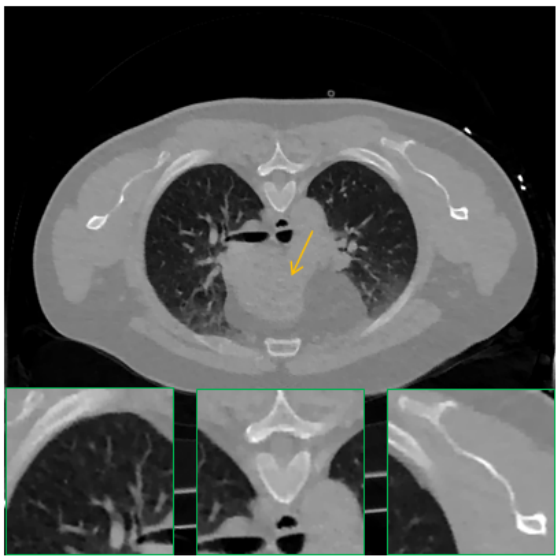

(e)

Figure 5.5. A reconstructed slice of the patient data: (a) FBP reconstruction from the 20 mAs sinogram; (b) FBP+NLM filtering from the 20 mAs sinogram (h=0.012); (c) PWLS-NLM reconstruction from the 20 mAs sinogram ($\beta=1\times10^{5}$, h=0.008); (d) PWLS-adaptiveNLM reconstruction from the 20 mAs sinogram ($\beta=1\times10^{5}$, $s=1\times10^{-3}$, $t=4\times10^{-6}$); (e) PWLS-TV reconstruction from the 20 mAs sinogram ($\beta=50$). All the images are displayed with the same window.

5.5 Discussion and conclusion

In this chapter, we proposed and validated an adaptive NLM-regularized statistical image reconstruction method for X-ray CT from low-dose acquisitions. One motivation of this work is that the traditional NLM filtering methods sometimes cannot completely remove the noise and streak artifacts in the low-dose CT images, especially when the streak artifacts are very severe. The NLM-regularized statistical image reconstruction method can mitigate this problem, partially due to the explicit statistical modeling of the projection data. However, the choice of the associated filtering parameter *h* as a spatially-invariant global constant in the NLM-based regularization may not be optimal for the reconstruction of the entire image. To further improve the reconstruction results, we proposed a novel strategy to determine locally optimal filtering parameter by considering local characteristics of the image, which made the NLM-based regularization to be adaptive. The experimental results with the PWLS-NLM and PWLS-adaptiveNLM methods proved that it is indeed necessary and beneficial to introduce the spatial adaptivity of the filtering parameter.

It is noted that the adaptive NLM-based regularization in this study is implemented in 2D domain. The implementation can be expanded to 3D space by setting the search-window and patch-window to, for instance, 17×17×17 and 5×5×5 respectively for isotropic data. This may further improve the performance of the proposed method, although it would also increase the computation burden.

Also, it is noted that the proposed adaptive NLM regularization shares similar idea with the edge-preserving TV (Tian et al. 2011) and adaptive-weighted TV (Liu et al. 2012) regularization. Although using different mechanism to incorporate the spatial

adaptivity, they essentially both consider local characteristics of the image to be reconstructed. However, the NLM-based regularization may have the advantage of better eliminating the patchy artifacts sometimes appearing in the TV-based regularization, due to the use of a larger neighborhood.

As any other proposed method, the presented PWLS-adaptiveNLM method also has some potential limitations. The first one is the parameters tuning. While the sizes of search-window and patch-window (also the standard deviation of the Gaussian kernel) do not show noticeable effects on the reconstructed image when they are set in a reasonable range and the parameter setting $t = 4\times10^{-6}$ in Eq. (7) works well, the strength parameter s in Eq. (7) seems need more manual tuning than the others. In this study, a typical range for s was found from 4×10^{-4} to 1×10^{-3}. Further investigation on the strength parameter is needed. This is another topic in our future research plan.

Chapter 6. Adaptive nonlocal-means regularized statistical image reconstruction for sparse-view CT

In previous chapter, we explored a NLM-regularized statistical image reconstruction scheme for low-mAs CT, which takes advantage of projection data and utilizes information only from current scan. While one can reduce CT radiation dose by either low-mAs or sparse-view data acquisition, the latter strategy may have additional advantage in computational burden due to fewer projection measurements. Therefore, in this chapter, we extend the NLM-regularized image reconstruction scheme on sparse-view CT to demonstrate its feasibility and efficacy.

6.1 Introduction

Low-dose X-ray computed tomography (CT) imaging is desired in clinic due to the growing concerns on excessive radiation dose to the patients (Brenner and Hall 2007). In addition to hardware improvement for CT systems (Hsieh 2009), two more cost-effective strategies have also been widely explored for radiation dose reduction: (1) lower the number of projection views per rotation (e.g., sparse-view) during projection data acquisition; and (2) lower the X-ray flux (e.g., mAs level) toward the patient per projection view. In this study, we focus on the first strategy wherein the projection data are sparsely sampled but the X-ray flux at each projection view remains relatively high. For this data acquisition manner, the reconstructed image by the conventional filtered back-projection (FBP) method usually suffers from view-aliasing artifacts due to insufficient angular sampling.

In order to improve image quality from abovementioned sparse-view acquisitions, various image reconstruction methods have been proposed. The first category of those methods is based on the compressed sensing (Donoho 2006), which was initially proposed to accurately reconstruct a signal from much fewer samples than that is required by the Nyquist sampling theorem. Although the CT images are generally not sparse in their original pixel representation, one can apply a sparsifying transform to increase the sparsity. Discrete gradient transform (DGT) is one of the most commonly used sparsifying transforms, which leads to the well-known total variation (TV) norm. Sidky et al (Sidky et al. 2006; Sidky and Pan 2008) investigated sparse-view CT reconstruction by minimizing the TV of the desired image with the adaptive steepest descent projection onto convex sets (ASD-POCS) algorithm. Also, the edge-preserving TV (Tian et al. 2011), adaptive-weighted TV (Liu et al. 2012), anisotropic TV (Debatin et al. 2012), and TV-strokes (Liu et al. 2014) models were explored for sparse-view CT image reconstitution. In addition, Chen et al (Chen et al. 2008) proposed a prior image constrained compressed sensing (PICCS) model to reconstruct dynamic CT images from sparsely sampled projection data. By introducing a prior image, it was reported that the PICCS method can better preserve the low-contrast objects (Lauzier et al. 2012). Besides DGT, other sparsifying transforms were also explored for sparse-view CT image

reconstruction, such as the wavelet transform (Yu and Wang 2010) or tight frame transform (Jia et al. 2011). The second category of reconstruction methods for sparse-view CT is based on dictionary learning (Donoho and Elad 2003). A dictionary is a redundant basis whose elements are called atoms and are learned from training images. Then, an image can be sparsely represented as a linear combination of the atoms. The dictionary learning-based method processes the image patch by patch, contrary to pixel by pixel fashion in conventional sparsifying transforms. Xu et al (Xu et al. 2012) investigated a way to utilize the dictionary learning-based sparsification as the regularization term for penalized reconstruction of sparse-view CT image. Furthermore, a dual dictionaries strategy (Lu et al. 2012), with one transitional dictionary for atom matching and one global dictionary for image updating, was also studied to improve the reconstructed image quality.

Another category of reconstruction methods for sparse-view CT is based on nonlocal means (NLM) algorithm (Buades et al. 2005). For instance, Jia et al (Jia et al. 2012) proposed a temporal NLM regularization for 4D CT image reconstruction or enhancement from sparse-view acquisitions, wherein the reconstruction of current frame image utilized the two neighboring frame images. Xu and Muller (Xu and Mueller 2012) tried to restore FBP-reconstructed sparse-view CT images with the help of a high quality prior image via the NLM algorithm, and noticed remarkable improvements over the conventional NLM filtering in suppressing the view-aliasing artifacts. However, the high quality prior image may not be readily available for some clinical applications, and even if it exists, registration is needed to align the two images, which can be challenging due to the existence of severe view-aliasing artifacts. In addition, a previous normal-dose CT scan induced nonlocal regularization was also investigated for iterative reconstruction of sparse-view CT (Zhang et al. 2012), but the method faced similar issues as the aforementioned method. In our previous work (Zhang et al. 2014; Zhang et al. 2015), we explored a generic NLM-regularized image reconstruction scheme for low-mAs CT, which takes advantage of projection data and utilizes information only from current scan. While one can reduce CT radiation dose by either low-mAs or sparse-view data acquisition, the latter strategy may have additional advantage in computational burden due to fewer projection measurements. Therefore, in this study, we extend the NLM-regularized image reconstruction scheme on sparse-view CT to demonstrate its feasibility and efficacy. Also, it is noted that the many NLM-based approaches generally utilize a spatially-invariant filtering parameter, but this setting is suboptimal for the entire image because the filtration may be too strong for some regions while too weak for other regions (Li et al. 2014; Zhang et al. 2015). Thus, in this study, we further investigate to use spatially-variant filtering parameters which are adaptive to the local characteristics of the image to be reconstructed. And the resulting approach is termed as adaptive NLM-regularized image reconstruction.

6.2 Adaptive NLM-regularized image reconstruction

The adaptive NLM-regularized image reconstruction for sparse-view CT can be formulated as:

$$\boldsymbol{\mu}^* = \arg\min_{\mu \geq 0} \{(\mathbf{y} - \mathbf{A}\boldsymbol{\mu})^T \boldsymbol{\Sigma}^{-1} (\mathbf{y} - \mathbf{A}\boldsymbol{\mu}) + \beta U(\boldsymbol{\mu})\} \tag{6.1}$$

While statistical modeling of projection measurements may not be essential in relatively high flux imaging application, the statistical assumption would still be important when the detected X-ray photon counts are limited (Xu and Tsui 2014). Therefore, we retain the weighted least-squares (WLS) rather than least-squares (LS) criterion as the data-fidelity term. $U(\boldsymbol{\mu})$ is the regularization term which is given as:

$$U(\boldsymbol{\mu}) = \sum_j \left(\mu_j - \sum_{k \in SW_j} w_{jk}(\boldsymbol{\mu}) \mu_k \right)^2, \quad \text{where } w_{jk}(\boldsymbol{\mu}) = \frac{\exp\left(-\left\| \mathbf{P}(\mu_j) - \mathbf{P}(\mu_k) \right\|_{2,a}^2 / h^2 \right)}{\sum_{k \in SW_j} \exp\left(-\left\| \mathbf{P}(\mu_j) - \mathbf{P}(\mu_k) \right\|_{2,a}^2 / h^2 \right)} \quad (6.2)$$

To further improve the reconstructed image quality, we utilized a locally-adaptive estimation of the filtering parameter h at pixel j as (Zhang et al. 2015):

$$h_j^2 = s \bullet mean\left\{ \left\| \mathbf{P}(\mu_j) - \mathbf{P}(\mu_k) \right\|_{2,a}, \; k \in SW_j \right\} + t \quad (6.3)$$

where s and t are two constants, and can be determined through experiments.

In this study, the regularization term in Eq. (6.2) using spatially-variant adaptive filtering parameter h in Eq. (6.3) is termed as adaptive NLM-based regularization and the resulting objective function in Eq. (6.1) is referred to as adaptive NLM-regularized image reconstruction.

6.3 Experiments and results

In this study, two categories of projection data (digital phantom and clinical patient) were utilized to evaluate the performance of the proposed NLM-regularized image reconstruction scheme for sparse-view CT. In the rest of this chapter, the NLM-regularized image reconstruction using spatially-invariant constant h is referred to as "PWLS-NLM", while the reconstruction using spatially-variant adaptive h in Eq. (6.3) is referred to as "PWLS-adaptiveNLM". For comparison purpose, the standard FBP reconstruction using Ramp filter at 100% Nyquist frequency (referred to as "FBP"), the FBP reconstruction followed by traditional NLM filtering (referred to as "NLM filtered FBP"), were also implemented.

6.3.1 Digital clock phantom

1). Projection data acquisition

A computer simulated clock phantom (Zhang et al. 2015) was utilized in this study, as shown in Figure 6.1. The clock phantom consists of a water background and eight circular inserts with different contrasts (C1: -100%, C2: +150%, C3: +7%, C4: -50%, C5: +85%, C6: -15%, C7: -7%, C8: +30%). The sinogram data was simulated utilizing a scanning geometry that mimics a Siemens Sensation 16 CT scanner (Siemens Healthcare, Forchheim, Germany). No noise was added in the sinogram data. The number of projection views per 360^0 rotation was simulated at 20, 30, 40, and 50.

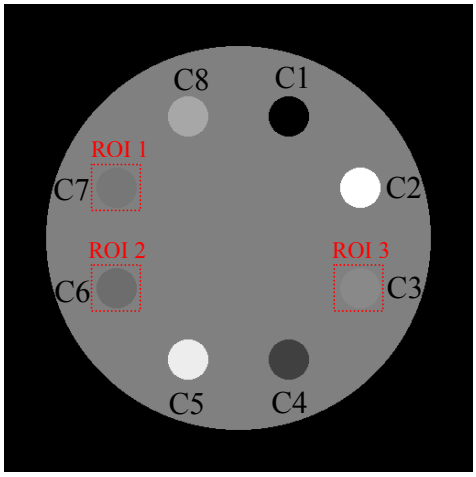

Figure 6.1. The computer simulated clock phantom.

2). Visualization-based evaluation

The reconstructed images by FBP, NLM filtered FBP, PWLS-NLM, and PWLS-adaptiveNLM, from 20, 30, 40, and 50 projection views are shown in Figure 6.2. We can observe that FBP reconstructed images suffer from severe view-aliasing artifacts, NLM filtered FBP images are still corrupted with artifacts, while the NLM-regularized image reconstructions drastically remove the artifacts. A closer observation shows that the PWLS-NLM reconstructions seem to blur the low-contrast inserts (C3: +7%, C6: -15%, C7: -7%) substantially, while the PWLS-adaptiveNLM reconstructions can better preserve the low-contrast objects. That is, the PWLS-adaptiveNLM reconstructions seem to achieve the best image quality among the four methods. Meanwhile, we can see that, as the number of projection views increases, the quality of reconstructed images by any method also improves. These observations are validated with quantitative metrics in the following sections.

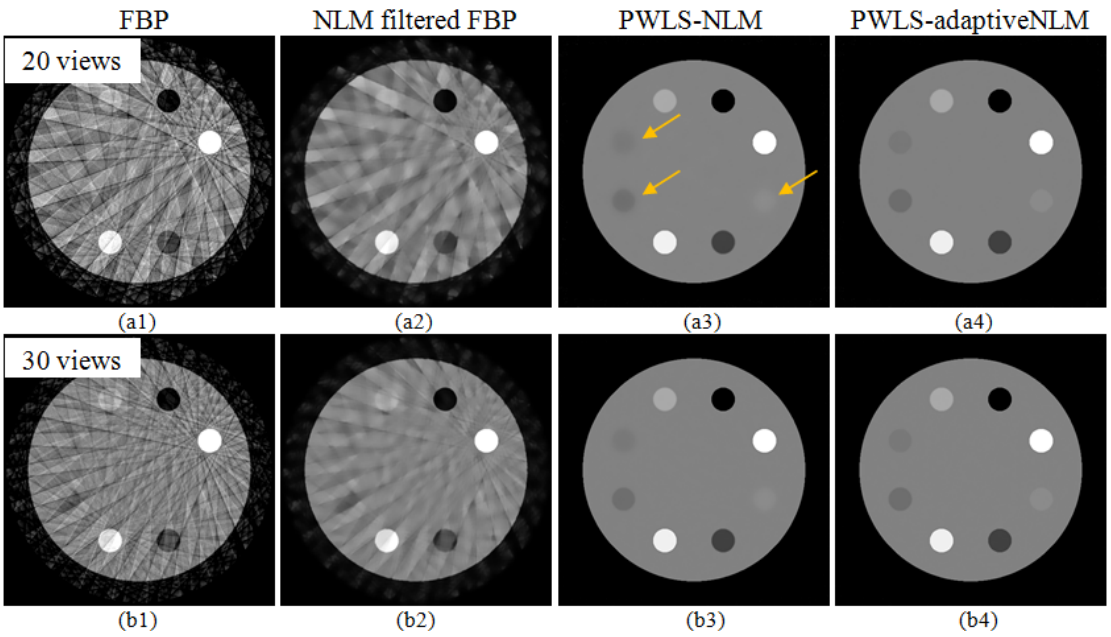

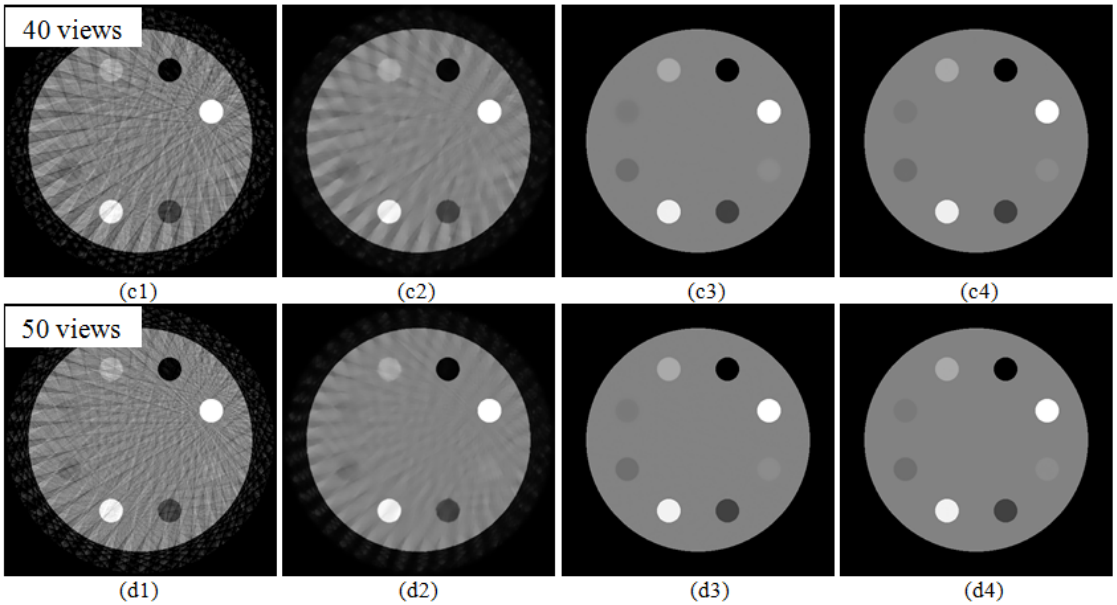

Figure 6.2. One reconstructed slice of the clock phantom by the four reconstruction methods from sparse-view acquisitions: (a1)-(a4) are reconstructed from 20 projection views; (b1)-(b4) are reconstructed from 30 projection views; (c1)-(c4) are reconstructed from 40 projection views; (d1)-(d4) are reconstructed from 50 projection views. All the images are displayed with the same window [0, 0.04] mm^{-1}.

3). Reconstruction accuracy

To evaluate the overall reconstruction accuracy of different reconstruction methods, the PSNR metric was employed. Table 6.1 demonstrates that the two NLM-regularized reconstructions have significantly higher PSNR than the FBP reconstructed images and the NLM filtered FBP images. Meanwhile, the PWLS-adaptiveNLM method has tiny gains over the PWLS-NLM method for all the cases, which is also consistent with our visual inspection.

Table 6.1. PSNR (dB) measures of the results reconstructed by the four methods for the clock phantom

Methods	*20 views*	*30 views*	*40 views*	*50 views*
FBP	19.23	21.49	22.89	23.12
NLM filtered FBP	25.53	28.97	30.53	31.41
PWLS-NLM	39.35	42.11	48.15	53.82
PWLS-adaptiveNLM	40.42	43.15	49.26	54.26

4). Assessing local image quality

The FBP reconstructed images in Figure 6.2 demonstrate that the high-contrast objects are easier to be recovered than the low-contrast objects. However, we know that the low-contrast objects are more critical in clinic. Therefore, in this work, we focus on the reconstruction of low-contrast inserts (C3: +7%, C6: -15%, C7: -7%) for the clock phantom. Three ROIs were chosen to include those inserts, as labeled by the red rectangles in Figure 6.1. Since the reconstruction accuracy study in the previous section

indicated that the two NLM-regularized image reconstruction methods obviously outperformed the FBP or NLM filtered FBP, we only compared the local image quality by the two NLM-regularized image reconstruction methods. The corresponding results with RMSE and UQI metrics are illustrated in Figure 6.3. Apparently, the PWLS-adaptiveNLM method generated better low-contrast objects reconstruction than the PWLS-NLM method, with lower RMSE and higher UQI. These results clearly demonstrate the merits of introducing the spatially-adaptive filtering parameter h in Eq. (4) for the NLM-regularized image reconstruction scheme.

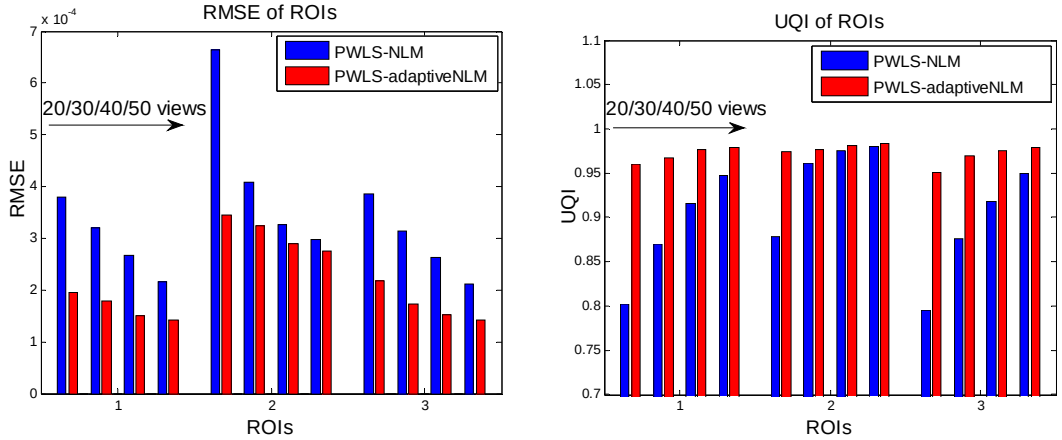

Figure 6.3. Performance comparison of the two NLM-regularized image reconstruction methods on reconstruction of the three ROIs labeled in Figure 6.1 with RMSE and UQI metrics. The corresponding methods are illustrated in figure legend.

6.3.2 Clinical patient data

1). Projection data acquisition

The projection data of a patient was acquired using the same Siemens scanner after obtaining informed consent from the patient, and this patient data serves as a pilot clinical study. The patient was scheduled for CT scan for medical reasons. The X-ray tube voltage was 120 kV, the mAs level was 100 mAs, and the number of projection views was 1160 per 360^0 rotation. Figure 6.4 shows one reconstructed slice of the patient from the projection data by the FBP method from the full 1160 projection views, which is considered as the ground truth image. In order to perform sparse-view CT image reconstruction, we evenly extracted 116 (10%), 145 (12.5%), 232 (20%), 290 (25%) projection views from the sinogram data. The size of reconstructed image is 512×512 with pixel size of 1.0 ×1.0 mm^2 for all implementations.

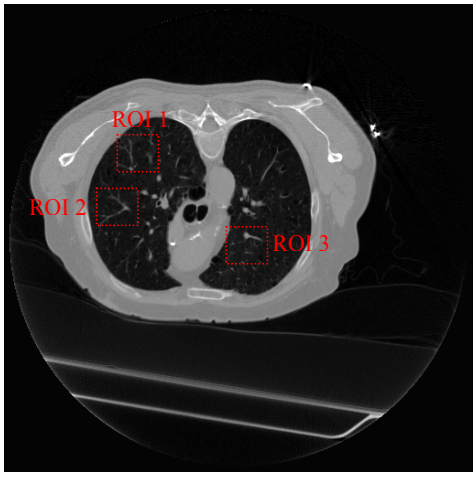

Figure 6.4. One reconstructed slice of the patient by the FBP method from 1,160 projection views.

2). Visualization-based evaluation

Figure 6.5 shows one reconstructed slice of the patient by the four image reconstruction methods from 116, 145, 232, and 290 projection views, respectively. Basically, we observe the same trends as the phantom study. That is, compared with the FBP and NLM filtered FBP methods, the two NLM-regularized image reconstruction methods can more effectively suppress the view-aliasing artifacts. Figure 6.6 illustrates the zoom-in views of Figure 6.5 for ROI 1 and ROI 3 which are labeled in Figure 6.4. The zoom-in views demonstrate that the PWLS-adaptiveNLM method is superior to the PWLS-NLM method in retaining the subtle structures in the image, which may be of great importance to physicians' diagnosis. In the following sections, we quantify the differences of the images reconstructed by the four methods.

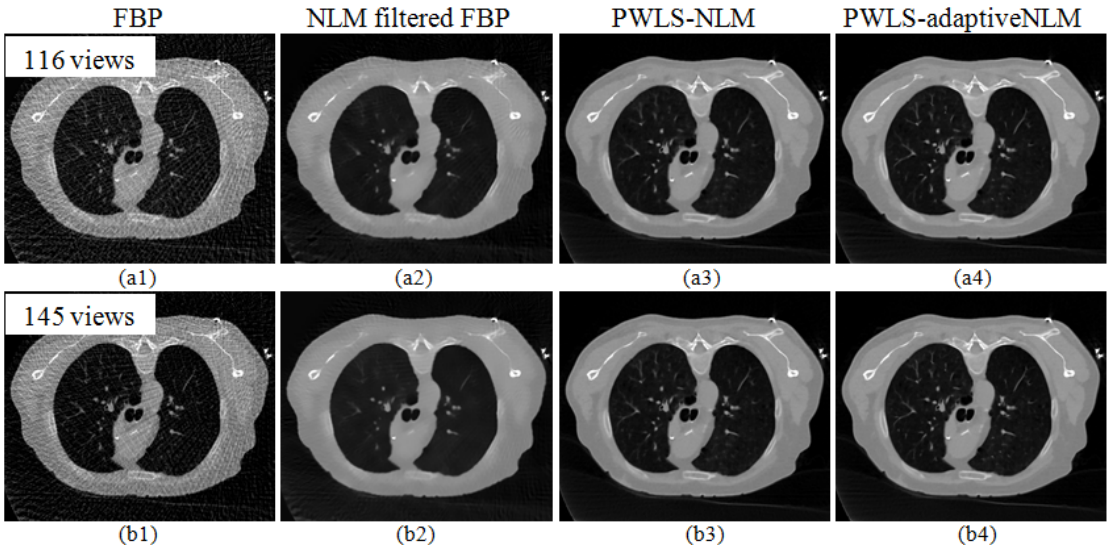

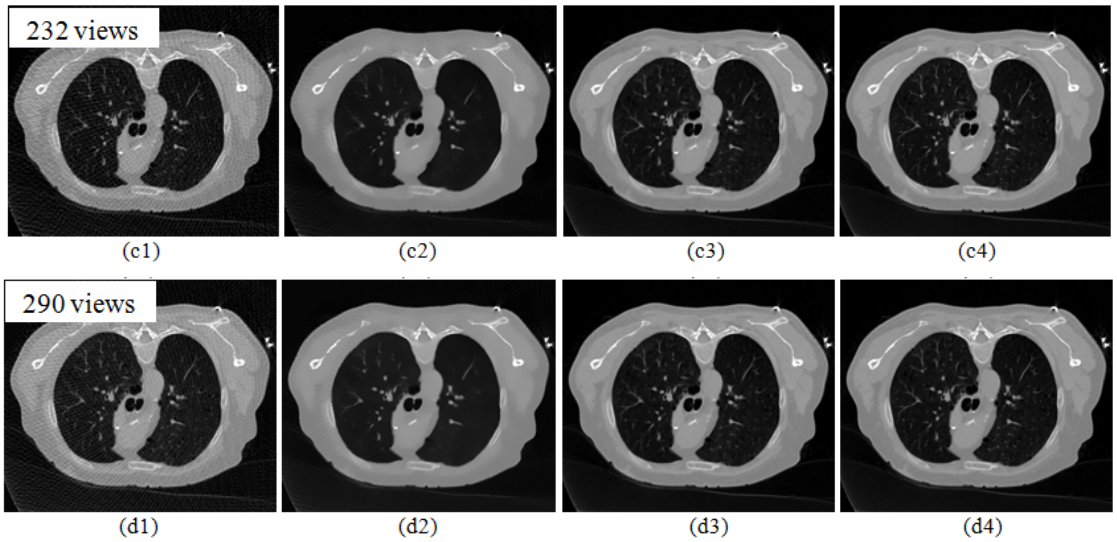

Figure 6.5. A reconstructed slice of the patient data by the four reconstruction methods from sparse-view acquisitions: (a1)-(a4) are reconstructed from 116 projection views; (b1)-(b4) are reconstructed from 145 projection views; (c1)-(c4) are reconstructed from 232 projection views; (d1)-(d4) are reconstructed from 290 projection views. All the images are displayed with the same window [0, 0.034] mm^{-1}, and the images are cropped for better visualization.

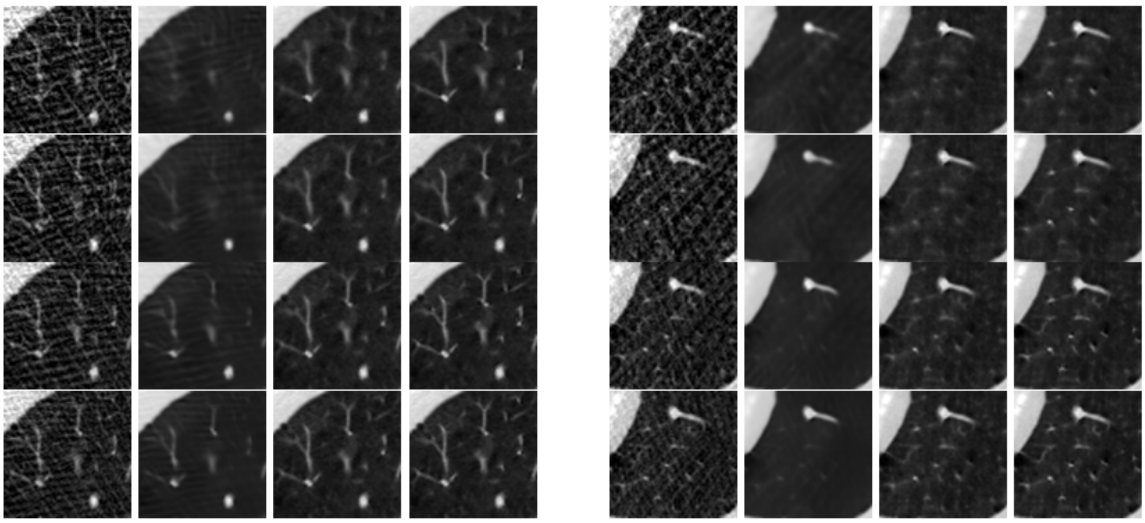

Figure 6.6. Zoom-in views of Figure 6.5 for two detailed ROIs labeled in Figure 6.4: Figure 6.6(a) corresponds to ROI 1 and Figure 6.6(b) corresponds to ROI 3. All the images are displayed with a typical lung window [0, 0.022] mm^{-1}.

3). Reconstruction accuracy

Table 6.2 illustrates the quantitative results of the four different reconstruction methods on the patient data with the PSNR metric. Still, the presented PWLS-adaptiveNLM method demonstrates the best reconstruction accuracy among the four methods for all cases.

Table 6.2. PSNR (dB) measures of the results reconstructed by the four methods for patient data

Methods	*116 views*	*145views*	*232 views*	*290 views*
FBP	24.70	26.00	28.98	30.50
NLM filtered FBP	32.22	33.54	35.10	35.89
PWLS-NLM	39.43	40.94	43.33	44.38
PWLS-adaptiveNLM	39.79	41.36	43.68	44.65

4). Assessing local image quality

To quantitatively demonstrate the gains of the PWLS-adaptiveNLM over the PWLS-NLM, we compared the performance of the two methods on the reconstruction of three ROIs in the lung region with subtle structures, which are labeled with red rectangles in Figure 6.4. The corresponding quantitative results based on the RMSE and UQI metrics are shown in Figure 6.7. For different projection views cases, the adaptive NLM method yields lower RMSE and higher UQI for all the three detailed ROIs.

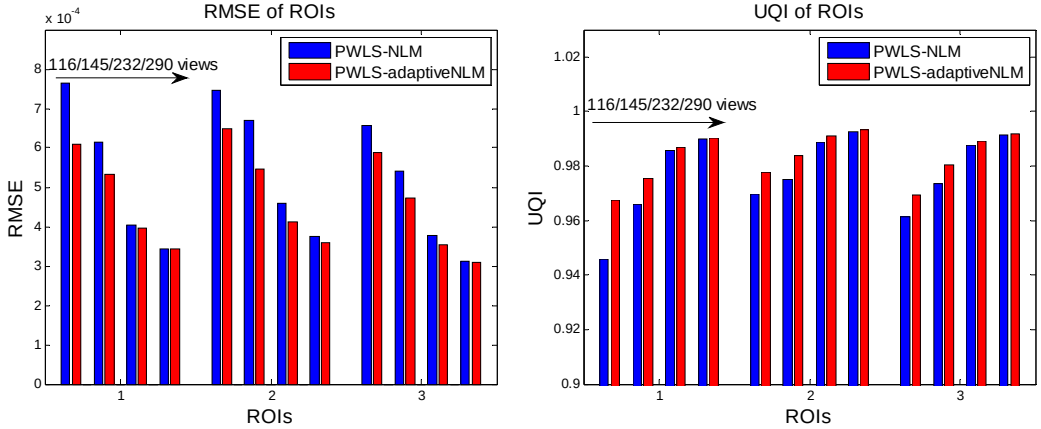

Figure 6.7. Performance comparison of the two NLM-regularized image reconstruction methods on reconstruction of the three ROIs labeled in Figure 6.4 with RMSE and UQI metrics. The corresponding methods are illustrated in figure legend.

6.4 Discussion and conclusion

In this study, we validated a NLM-regularized image reconstruction scheme for X-ray CT from sparse-view acquisitions. The experimental results with computer simulated phantom and clinical patient data demonstrate that the presented reconstruction scheme can successfully suppress the view-aliasing artifacts, and outperforms the method that taking NLM filtration of FBP reconstructed images. Meanwhile, the NLM-regularized image reconstruction using spatially-variant adaptive filtering parameters can better recover the low-contrast objects and subtle structures than that using spatially-invariant constant filtering parameter. Therefore, in order to improve image quality of low-contrast objects and subtle structures, it may be beneficial to employ the adaptive NLM-regularized image reconstruction method.

It is well known that the FBP reconstructed CT images from sparse-view acquisitions usually suffer from view-aliasing artifacts. Applying the NLM filter directly to FBP reconstructed CT images (i.e., NLM filtered FBP) is not quite effective in suppressing the

view-aliasing artifacts. Therefore, in this study, we propose a NLM-regularized image reconstruction scheme for sparse-view CT. Experimental results with the phantom and patient datasets demonstrate that the proposed reconstruction scheme is advantageous to the NLM filtered FBP method in suppressing the view-aliasing artifacts, as shown in Figure 6.2 and Figure 6.5. In order to improve the quality of low-contrast objects and subtle structures, we further investigate to design locally adaptive filtering parameters for the NLM-based regularization. Figure 6.3 and Figure 6.7 quantitatively illustrate that the adaptive NLM-regularized image reconstruction method considerably improves the quality of low-contrast objects and subtle structures as compared with the conventional NLM-regularized image reconstruction method, although it only marginally improves the overall image quality as shown in Table 6.1 and Table 6.2. Finally, it is also noted that, previous studies (Manjón et al. 2010; Li et al. 2014) which used NLM as a post-processing filter also demonstrated the benefits of employing adaptive filtering parameters. That is, the conclusions are consistent, no matter using the NLM as a post-processing filter or regularization in iterative reconstruction.

Chapter 7. Overview and prospective of statistical image reconstruction for low-dose CT

The statistical image reconstruction (SIR) methods for CT have been explored for radiation dose reduction in the past decades. Each of the SIR methods consists of two basic components of (1) construction of an adequate objective function and (2) utilization of a suitable algorithm for maximization or minimization of the objective function.

7.1 Construction of objective function

In construction of the objective function, the statistical modeling of the projection measurements for the data fidelity term is a prerequisite. The statistical phenomena in CT projection measurements are so complicated that it is rarely practical to have an exact statistical model and likelihood function (Nuyts et al. 2013). Instead, the statistical models in chapter 2 are considered as good approximations, and have been widely employed in the CT image reconstruction. In addition to the statistical model, a good regularization term is also a key to solve the ill-posed inverse problems including low-dose CT reconstruction. In practice, effectively suppressing the noise and streak artifacts while preserving the edges/details/contrasts are the two major concerns when designing a regularization term. Many regularization terms have been proposed and studied for low-dose CT reconstruction in the past decades, including those proposed in this dissertation. And more desirable regularizations based on prior knowledge may be proposed in the future.

While the statistical models in chapter 2 can reasonably describe the statistical properties of the low-dose CT projection data, the regularization for faithful image reconstruction remains an open question. There are many regularization models to impose local smoothness on the image, however, their diagnostic values are still not well documented. In theory, the regularization shall incorporate the prior knowledge of the image to be reconstructed. Unfortunately, the diagnostic information is not known in prior and actually need to be from the current scan. However, for some specific clinical tasks, such image-guided interventions, prior knowledge is available to achieve the task.

Furthermore, the hyper-parameter β in the pML or PWLS criterion controls the tradeoff between the data fidelity term and the regularization term. A larger β value produces a more smoothed reconstruction with lower noise but also lower resolution, and *vice versa*. The noise-resolution tradeoff curve, or bias-variance tradeoff curve, can indicate the influence of β value selection on reconstructed image quality. In practice, a series of β values can be tested for a specific SIR method with specific projection data, and after the images are reconstructed, visual inspection and quantitative measurements are used to determine the optimal β value. This scheme can also be considered as a process of trial and error. But generally, the selection of β value for SIR methods is still an open question and is considered as one of their drawbacks.

7.2 Optimization of objective function

Efficient algorithms for objective function optimization are important to avoid local maximum or minimum for the optimal solution. An iterative algorithm is typically employed because the objective function usually does not have a closed-form solution, or even if it has closed-form solution it is still impractical to directly invert the system matrix due to the large size (Fessler 2006). Several types of iterative algorithms have been proposed for solving objective functions of SIR, including the steepest descent (or gradient descent), conjugate gradient, expectation maximization, iterative coordinate descent, separable parabolic surrogates and so on (Fessler 2000). The selection of an iterative algorithm depends on several factors such as the form of the objective function, convergence rate, parallelization ability, and reconstruction accuracy. There are also some variants of these iterative algorithms which attempt to accelerate the reconstruction, such as the ordered subsets, group coordinate descent, and alternating direction method of multipliers approaches. In this dissertation, the objective function is usually of a quadratic form and easy to be optimized by the GS method.

7.3 Clinical use of SIR methods

Although considerable progress has been made on SIR of CT during the past decades, the analytical FBP method is still employed by most commercial scanners for image reconstruction. Due to a strong desire for radiation dose reduction, SIR methods have recently become an endeavor for major CT vendors, and some prototypes products based on this have been exhibited in a number of national and international meetings. Since the optimization of objective function for SIR is routinely performed by iterative algorithms, the computational burden due to multiple re-projection and back-projection operation cycles in the projection and image domains has always been one big challenge for clinical use. However, software approaches and hardware approaches using the graphical processing unit (GPU) (Xu and Mueller 2005) and cell broad-band engine (Knaup et al. 2006) have been investigated to accelerate the iterative procedure and substantially reduce the reconstruction time. With constant improvements in computation technology, SIR methods can move closer to clinical use and may play a dominant role there in the near future.

Publications on peer-reviewed journals

- **Zhang H**, Han H, Liang Z, Hu Y, Liu Y, Moore W, Ma J, and Lu H (2015). "Extracting information from previous full-dose CT scan for knowledge-based Bayesian reconstruction of current low-dose CT images." *IEEE Trans. Medical Imaging* (DOI 10.1109/TMI.2015.2498148).

- **Zhang H**, Ma J, Wang J, Liu Y, Han H, Lu H, Moore W, and Liang Z (2015). "Statistical image reconstruction for low-dose CT using nonlocal means-based regularization. Part II: An adaptive approach." *Computerized Medical Imaging and Graphics* 43: 26-35.

- **Zhang H**, Han H, Wang J, Ma J, Liu Y, Moore W, and Liang Z (2014). "Deriving adaptive MRF coefficients from previous normal-dose CT scan for low-dose image reconstruction via penalized weighted least-squares minimization." *Medical Physics* 41(4): 041916.

- **Zhang H**, Ma J, Wang J, Liu Y, Lu H, and Liang Z (2014). "Statistical image reconstruction for low-dose CT using nonlocal means-based regularization." *Computerized Medical Imaging and Graphics* 38(6): 423-435.

- **Zhang H**, Li L, Zhu H, Han H, Song B, and Liang Z (2014). "Integration of 3D scale-based pseudo-enhancement correction and partial volume image segmentation for electronic colon cleansing in CT colonograpy." *Journal of X-Ray Science and Technology* 22(2): 271-283.

- Liu Y, Liang Z, Ma J, Lu H, Wang K, **Zhang H**, and Moore W (2014). "Total variation-stokes strategy for sparse-view X-ray CT image reconstruction." *IEEE Trans. Medical Imaging* 33(3): 749-763.

- Liu Y, Ma J, **Zhang H**, Wang J, and Liang Z (2014). "Low-mAs X-ray CT image reconstruction by adaptive-weighted TV constrained penalized re-weighted least-squares."*Journal of X-Ray Science and Technology* 22(4): 437-457.

- Han H, Li L, Duan C, **Zhang H**, Zhao Y, and Liang Z (2013). "A unified EM Approach for bladder wall segmentation with coupled level sets constraints." *Medical Image Analysis* 17:1192-1205.

Bibliography

Aerts, H. J., E. R. Velazquez, et al. (2014). "Decoding tumour phenotype by noninvasive imaging using a quantitative radiomics approach." Nature communications 5.

Beister, M., D. Kolditz, et al. (2012). "Iterative reconstruction methods in X-ray CT." Physica Medica 28(2): 94-108.

Bouman, C. A. and K. Sauer (1996). "A unified approach to statistical tomography using coordinate descent optimization." IEEE Transactions on Image Processing 5(3): 480-492.

Brenner, D. J. and E. J. Hall (2007). "Computed tomography—an increasing source of radiation exposure." New England Journal of Medicine 357(22): 2277-2284.

Buades, A., B. Coll, et al. (2005). A non-local algorithm for image denoising. IEEE Computer Vision and Pattern Recognition (CVPR), IEEE.

Buades, A., B. Coll, et al. (2006). "Image enhancement by non-local reverse heat equation." Preprint CMLA 22: 2006.

Chen, G.-H., J. Tang, et al. (2008). "Prior image constrained compressed sensing (PICCS): a method to accurately reconstruct dynamic CT images from highly undersampled projection data sets." Med Phys 35(2): 660-663.

Coupé, P., J. V. Manjón, et al. (2011). "Patch-based segmentation using expert priors: Application to hippocampus and ventricle segmentation." NeuroImage 54(2): 940-954.

Coupé, P., P. Yger, et al. (2008). "An optimized blockwise nonlocal means denoising filter for 3-D magnetic resonance images." Medical Imaging, IEEE Transactions on 27(4): 425-441.

Dang, H., A. Wang, et al. (2014). "dPIRPLE: a joint estimation framework for deformable registration and penalized-likelihood CT image reconstruction using prior images." Phys Med Biol 59(17): 4799.

De Man, B. and S. Basu (2004). "Distance-driven projection and backprojection in three dimensions." Phys Med Biol 49(11): 2463.

Debatin, M., P. Zygmanski, et al. (2012). CT reconstruction from few-views by Anisotropic Total Variation minimization. Nuclear Science Symposium and Medical Imaging Conference (NSS/MIC), 2012 IEEE, IEEE.

Donoho, D. L. (2006). "Compressed sensing." IEEE Transactions on Information Theory 52(4): 1289-1306.

Donoho, D. L. and M. Elad (2003). "Optimally sparse representation in general (nonorthogonal) dictionaries via ℓ1 minimization." Proceedings of the National Academy of Sciences 100(5): 2197-2202.

Evans, J. D., D. G. Politte, et al. (2011). "Noise-resolution tradeoffs in x-ray CT imaging: A comparison of penalized alternating minimization and filtered backprojection algorithms." Med Phys 38(3): 1444-1458.

Faul, F., E. Erdfelder, et al. (2009). "Statistical power analyses using G* Power 3.1: Tests for correlation and regression analyses." Behavior research methods 41(4): 1149-1160.

Fessler, J. A. (2000). "Statistical image reconstruction methods for transmission tomography." Handbook of Medical Imaging 2: 1-70.

Fessler, J. A. (2006). "Iterative methods for image reconstruction." ISBI Tutorial. Arlington Virginia: April.

Giraldo, J. R., Z. S. Kelm, et al. (2009). Comparative study of two image space noise reduction methods for computed tomography: bilateral filter and nonlocal means. Engineering in Medicine and Biology Society, 2009. EMBC 2009. Annual International Conference of the IEEE, IEEE.

Han, H., L. Li, et al. (2015). "Fast and adaptive detection of pulmonary nodules in thoracic CT images using a hierarchical vector quantization scheme." Biomedical and Health Informatics, IEEE Journal of 19(2): 648-659.

Haralick, R. M., K. Shanmugam, et al. (1973). "Textural features for image classification." Systems, Man and Cybernetics, IEEE Transactions on(6): 610-621.

Herman, G. (1980). Image reconstruction from projections: the fundamentals of computerized tomography, Academic.

Hsieh, J. (2009). Computed tomography: principles, design, artifacts, and recent advances, SPIE Bellingham, WA.

Jia, X., B. Dong, et al. (2011). "GPU-based iterative cone beam CT reconstruction using tight frame regularization." Phys Med Biol 56(13): 3787-3807.

Jia, X., Z. Tian, et al. (2012). "Four-dimensional cone beam CT reconstruction and enhancement using a temporal nonlocal means method." Medical physics 39(9): 5592-5602.

Knaup, M., W. A. Kalender, et al. (2006). Statistical cone-beam CT image reconstruction using the cell broadband engine. Nuclear Science Symposium Conference Record, 2006. IEEE, IEEE.

La Rivière, P. J., J. Bian, et al. (2006). "Penalized-likelihood sinogram restoration for computed tomography." IEEE Transactions on Medical Imaging 25(8): 1022-1036.

La Rivière, P. J. and D. M. Billmire (2005). "Reduction of noise-induced streak artifacts in X-ray computed tomography through spline-based penalized-likelihood sinogram smoothing." IEEE Transactions on Medical Imaging 24(1): 105-111.

Lange, K. and R. Carson (1984). "EM reconstruction algorithms for emission and transmission tomography." J Comput Assist Tomogr 8(2): 306-316.

Lauzier, P. T., J. Tang, et al. (2012). "Prior image constrained compressed sensing: Implementation and performance evaluation." Med Phys 39(1): 66-80.

Li, T., X. Li, et al. (2004). "Nonlinear sinogram smoothing for low-dose X-ray CT." IEEE Transactions on Nuclear Science 51(5): 2505-2513.

Li, Z., L. Yu, et al. (2014). "Adaptive nonlocal means filtering based on local noise level for CT denoising." Med Phys 41(1): 011908.

Liu, Y., Z. Liang, et al. (2014). "Total variation-stokes strategy for sparse-view X-ray CT image reconstruction." IEEE Transactions on Medical Imaging 33(3): 749 - 763.

Liu, Y., J. Ma, et al. (2012). "Adaptive-weighted total variation minimization for sparse data toward low-dose x-ray computed tomography image reconstruction." Phys Med Biol 57(23): 7923.

Lou, Y., X. Zhang, et al. (2010). "Image recovery via nonlocal operators." Journal of Scientific Computing 42(2): 185-197.

Lu, H., X. Li, et al. (2002). Analytical noise treatment for low-dose CT projection data by penalized weighted least-square smoothing in the KL domain. SPIE Medical Imaging, International Society for Optics and Photonics.

Lu, Y., J. Zhao, et al. (2012). "Few-view image reconstruction with dual dictionaries." Phys Med Biol 57(1): 173.

Ma, J., J. Huang, et al. (2011). "Low-dose computed tomography image restoration using previous normal-dose scan." Medical physics 38(10): 5713-5731.

Ma, J., Z. Liang, et al. (2012). "Variance analysis of x-ray CT sinograms in the presence of electronic noise background." Med Phys 39(7): 4051-4065.

Ma, J., H. Zhang, et al. (2012). "Iterative image reconstruction for cerebral perfusion CT using a pre-contrast scan induced edge-preserving prior." Phys Med Biol 57(22): 7519.

Macovski, A. (1983). Medical Imaging Systems. New Jersey, Prentice Hall.

Manduca, A., L. Yu, et al. (2009). "Projection space denoising with bilateral filtering and CT noise modeling for dose reduction in CT." Med Phys 36(11): 4911-4919.

Manjón, J. V., P. Coupé, et al. (2010). "Adaptive non‐local means denoising of MR images with spatially varying noise levels." Journal of Magnetic Resonance Imaging 31(1): 192-203.

Nett, B., J. Tang, et al. (2009). Low radiation dose C-arm cone-beam CT based on prior image constrained compressed sensing (PICCS): including compensation for image volume mismatch between multiple data acquisitions. SPIE Medical Imaging, Lake Buena Vista, FL, International Society for Optics and Photonics.

Nuyts, J., B. De Man, et al. (2013). "Modelling the physics in the iterative reconstruction for transmission computed tomography." Phys Med Biol 58(12): R63.

Saha, P. and J. Udupa (2000). "Scale based image filtering preserving boundary sharpness and fine structures." IEEE Trans. Med. Imaging. v20: 1140-1155.

Sauer, K. and C. Bouman (1993). "A local update strategy for iterative reconstruction from projections." IEEE Transactions on Image Processing 41(2): 534-548.

Shepp, L. A. and Y. Vardi (1982). "Maximum likelihood reconstruction for emission tomography." IEEE Transactions on Medical Imaging 1(2): 113-122.

Sidky, E. Y., C.-M. Kao, et al. (2006). "Accurate image reconstruction from few-views and limited-angle data in divergent-beam CT." Journal of X-ray Science and Technology 14(2): 119-139.

Sidky, E. Y. and X. Pan (2008). "Image reconstruction in circular cone-beam computed tomography by constrained, total-variation minimization." Phys Med Biol 53(17): 4777.

Siewerdsen, J., A. Waese, et al. (2004). "Spektr: A computational tool for x-ray spectral analysis and imaging system optimization." Med Phys 31(11): 3057-3067.

Snyder, D. L., A. M. Hammoud, et al. (1993). "Image recovery from data acquired with a charge-coupled-device camera." JOSA A 10(5): 1014-1023.

Snyder, D. L., C. W. Helstrom, et al. (1995). "Compensation for readout noise in CCD images." JOSA A 12(2): 272-283.

Stayman, J. W., H. Dang, et al. (2013). "PIRPLE: a penalized-likelihood framework for incorporation of prior images in CT reconstruction." Phys Med Biol 58(21): 7563.

Tang, J., B. E. Nett, et al. (2009). "Performance comparison between total variation (TV)-based compressed sensing and statistical iterative reconstruction algorithms." Phys Med Biol 54(19): 5781.

Thibault, J.-B., C. A. Bouman, et al. (2006). A recursive filter for noise reduction in statistical iterative tomographic imaging. SPIE Electronic Imaging, International Society for Optics and Photonics.

Thibault, J.-B., K. D. Sauer, et al. (2007). "A three-dimensional statistical approach to improved image quality for multislice helical CT." Med Phys 34(11): 4526-4544.

Tian, Z., X. Jia, et al. (2011). "Low-dose 4DCT reconstruction via temporal nonlocal meansa)." Medical physics 38(3): 1359-1365.

Tian, Z., X. Jia, et al. (2011). "Low-dose CT reconstruction via edge-preserving total variation regularization." Phys Med Biol 56(18): 5949.

Wang, J., T. Li, et al. (2006). "Penalized weighted least-squares approach to sinogram noise reduction and image reconstruction for low-dose X-ray computed tomography." IEEE Transactions on Medical Imaging 25(10): 1272-1283.

Wang, J., K. Sauer, et al. (2012). Prediction coefficient estimation in markov random fields for iterative x-ray ct reconstruction. SPIE Medical Imaging, International Society for Optics and Photonics.

Whiting, B. R., P. Massoumzadeh, et al. (2006). "Properties of preprocessed sinogram data in x-ray computed tomography." Med Phys 33(9): 3290-3303.

Xu, F. and K. Mueller (2005). "Accelerating popular tomographic reconstruction algorithms on commodity PC graphics hardware." Nuclear Science, IEEE Transactions on 52(3): 654-663.

Xu, J. and B. Tsui (2014). "Quantifying the importance of the statistical assumption in statistical x-ray CT image reconstruction." IEEE Transactions on Medical Imaging 33(1): 61-73.

Xu, J. and B. M. Tsui (2009). "Electronic noise modeling in statistical iterative reconstruction." IEEE Transactions on Image Processing 18(6): 1228-1238.

Xu, Q., H. Yu, et al. (2012). "Low-dose X-ray CT reconstruction via dictionary learning." IEEE Transactions on Medical Imaging 31(9): 1682-1697.

Xu, W. and K. Mueller (2012). "Efficient low-dose CT artifact mitigation using an artifact-matched prior scan." Med Phys 39(8): 4748-4760.

Yavuz, M. and J. A. Fessler (1998). "Statistical image reconstruction methods for randoms-precorrected PET scans." Med Image Anal 2(4): 369-378.

Yu, H. and G. Wang (2010). "SART-type image reconstruction from a limited number of projections with the sparsity constraint." Journal of Biomedical Imaging 2010: 3.

Yu, H., S. Zhao, et al. (2009). "Ultra-low dose lung CT perfusion regularized by a previous scan." Academic radiology 16(3): 363-373.

Zhang, H., Z. Bian, et al. (2012). Sparse angular X-ray cone beam CT image iterative reconstruction using normal-dose scan induced nonlocal prior. Nuclear Science Symposium and Medical Imaging Conference (NSS/MIC), 2012 IEEE, IEEE.

Zhang, H., H. Han, et al. (2014). "Deriving adaptive MRF coefficients from previous normal-dose CT scan for low-dose image reconstruction via penalized weighted least-squares minimization." Med Phys 41(4): 041916.

Zhang, H., Y. Liu, et al. (2013). Investigation on scale-based neighborhoods in MRFs for statistical iterative reconstruction. Nuclear Science Symposium and Medical Imaging Conference (NSS/MIC), 2013 IEEE, IEEE.

Zhang, H., J. Ma, et al. (2015). "Statistical image reconstruction for low-dose CT using nonlocal means-based regularization. Part II: An adaptive approach." Computerized Medical Imaging and Graphics 43: 26-35.

Zhang, H., J. Ma, et al. (2014). "Statistical image reconstruction for low-dose CT using nonlocal means-based regularization." Computerized Medical Imaging and Graphics 38(6): 423-435.